Dissertations and Theses

5-2015

Attitude Determination & Control System Design and Implementation for a 6U CubeSat Proximity Operations Mission

Francisco J. Franquiz

ATTITUDE DETERMINATION & CONTROL SYSTEM DESIGN AND

IMPLEMENTATION FOR A 6U CUBESAT PROXIMITY OPERATIONS MISSION

A Thesis

Submitted to the Faculty

of

Embry-Riddle Aeronautical University

by

Francisco J. Franquiz

In Partial Fulfillment of the

Requirements for the Degree

of

Master of Science in Aerospace Engineering

May 2015

Embry-Riddle Aeronautical University
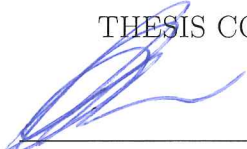
Daytona Beach, Florida

ATTITUDE DETERMINATION & CONTROL SYSTEM DESIGN AND
IMPLEMENTATION FOR A 6U CUBESAT PROXIMITY OPERATIONS MISSION

by

Francisco J. Franquiz

A Thesis prepared under the direction of the candidate's committee chairman, Dr.
Bogdan Udrea, Department of Aerospace Engineering, and has been approved by the
members of the thesis committee. It was submitted to the School of Graduate Studies
and Research and was accepted in partial fulfillment of the requirements for the
degree of Master of Science in Aerospace Engineering.

THESIS COMMITTEE

_____
Chairman, Dr. Bogdan Udrea

_____
Member, Dr. Mark Balas

_____
Member, Dr. Richard Prazenica

_____
Department Chair, Dr. Anastasios Lyrintzis
or Graduate Program Coordinator, Dr. Yi Zhao

4/28/15
_____
Date

_____
Dean of College of Engineering, Dr. Maj Mirmirani

4/28/15
_____
Date

_____
Associate VP for Academics, Dr. Robert Oxley

4-28-15
_____
Date

To my mother... whose undying devotion, affection, and support will forever be an inspiration.

ACKNOWLEDGMENTS

TABLE OF CONTENTS

LIST OF TABLES

LIST OF FIGURES

Figure
Page

Figure   Page

ABBREVIATIONS

ADCS	attitude determination and control
AFRL	Air Force Research Laboratory
ARAPAIMA	Application for Resident Space Object Proximity Analysis and IMAging
BFF	body-fixed frame
COTS	commercial off-the-shelf
DAC97	DSMC Analysis Code
DOF	degrees of freedom
DSMC	direct solution Monte Carlo
ECEF	Earth centered Eart fixed
ECI	Earth centered inertial
EKF	extended Kalman filter
FOH	first order hold
FOV	field of view
IMU	inertial measurement unit
IR	infrared
LEO	low Earth orbit
LVLH	local vertial local horizontal
LTP	local tangent plane
MOI	moment of inertia
MSISE90	Mass Spectrometer and Incoherent Scatter Radar Extended 1990
NED	North East down
NRLMSISE00	Naval Research Lab Mass Spectrometer and Incoherent Scatter Radar Extended 2000
OBC	on-board computer
OMT	orbital maneuvering thruster
PID	proportional-integral-derivative
RCS	reaction control system
RSO	resident space object
RW	reaction wheels
SRP	solar radiation pressure
STK	Systems Tool Kit
STR	start tracker
UNP	University Nano-Satellite Program
WGS84	World Geodetic System 1984
WMM	World Magnetic Model

ABSTRACT

Franquiz, Francisco J. MSAE, Embry-Riddle Aeronautical University, May 2015.

Attitude Determination & Control System Design and Implementation for a 6U

CubeSat Proximity Operations Mission.

The purpose of this work is to discuss the attitude determination and control system (ADCS) design process and implementation for a $12\,\mathrm{kg}$, $6\,\mathrm{U}$ ($36.6\,\mathrm{cm} \times 23.9\,\mathrm{cm} \times 27.97\,\mathrm{cm}$) CubeSat class nano-satellite. The design is based on the requirements and capabilities of the Application for Resident Space Object Proximity Analysis and IMAging (ARAPAIMA) proximity operations mission. The satellite is equipped with a cold gas propulsion system capable of exerting $2.5\,\mathrm{mN\,m}$ torques in both directions about each body axis. The attitude sensors include an angular rate gyro and star tracker (STR), supplemented by the payload optical array cameras.

The dynamic simulation of the satellite includes extensive environmental models and analyses that show how the satellite attitude is affected by aerodynamic drag, solar radiation pressure, gravity gradient torques, and residual magnetic moments. A mechanical propellant slosh model and a reaction torque analysis of the deployable solar panel hinges approximate the internal dynamics of the satellite. A trade study is presented to justify the use of a reaction control thruster actuated system over the more traditional reaction wheel configuration. Both actuation systems are modeled to hardware specifications and their propellant and energy requirements are examined alongside pointing performance.

Two methods of accounting for sensor noise and sampling rates are presented. The first is an extended Kalman filter based on the nonlinear model of a rate gyro coupled with quaternion attitude kinematics. The second presents a gyro-less angular rate observer capable of extrapolating STR measurements to the desired frequency. An additional method uses images from the payload cameras to perform [camera] frame centering maneuvers and to address the possibility of bias in the controller reference signal.

Four different controllers are described to reflect the chronological progression of the ADCS design. The first controller, designed to perform long angle maneuvers and target tracking, utilizes fixed gain eigenaxis control. The same controller is then augmented with a parallel proportional-integral-derivative (PID) type control law

using scheduled gains. This configuration is designed to switch between eigenaxis and PID control during imaging procedures to take advantage of the integral control introduced by the PID algorithm. To reduce system complexity, a modified eigenaxis control law, which incorporates scheduled integral control but does not require a switch to PID control, is introduced. A discrete time equivalent of the modified eigenaxis control law is also developed. Additionally, a brief description of a detumbling control law is presented.

Each of the four control laws is paired and tested with the different feedback and estimation methods discussed. An extensive showcase of numerical simulation results outlines the pointing performance of each system configuration and evaluates their capabilities of meeting a $1\,\mathrm{arcmin}$ $(3\,\sigma)$ pointing requirement. A comparison of the different properties and performance of each control system configuration precedes the selection of the discrete modified eigenaxis control law as the best alternative.

1. Introduction

The objective of this thesis is to describe the design process and implementation of an attitude determination and control system (ADCS) on a CubeSat class nano-satellite platform. Rather than focusing on traditional stability and performance requirements alone, the ADCS design has followed the development of the Application for Resident Space Object Proximity Analysis and IMAging (ARAPAIMA) mission since its conception. Therefore, the design approach emphasizes that the ADCS is a component of a larger system. As such, environmental, dynamic, and hardware modeling are all implemented to reflect projected mission scenarios and design choices ranging from body geometry to available computational resources. The result is an extensive model and simulation environment flexible enough to accommodate a growing system.

The ADCS design is divided into three main areas: dynamic modeling, filtering and estimation, and controller implementation. The dynamics of the system include the environmental models and attitude mechanics which describe the translational and rotational behavior of the satellite. The filtering and estimation models account for the different hardware properties of the system sensors. Lastly, the controller design brings the control algorithms together with the dynamics and estimation to ensure mission

performance requirements are met. Comprehensive results of the ADCS pointing performance are presented to show the logical progression of the design process.

1.1   CubeSat Background

The increasing interest in low budget space missions together with continuing advances in miniaturization of high performance electronics has lead to significant growth in the development of small satellites. These satellites, designated nano-satellites and micro-satellites, aim to fulfill missions of the same scope as their full-sized counterparts at a fraction of the cost. The flexibility of their design and relatively low complexity represent an opportunity for mass production and deployment at a scale hitherto unseen in the space industry.

These advantages, along with rising commercial support, have enabled academia to become involved in active projects and initiatives worldwide. The most noticeable of these began at CalPoly with the development of the CubeSat standard in 1999 (RikiMunakata, 2009). Since then CubeSats, miniaturized satellites with volume measured in increments of $10\,\mathrm{cm}^3$ ($1\,\mathrm{U}$), have become associated with university space research programs. These satellites usually weigh approximately $1\,\mathrm{km}$ per U and use commercial off-the-shelf (COTS) products to simplify the design process and reduce the overall construction cost. However, further development of space qualified electronics designed specifically for use on the CubeSat platform continues to close the gap between the capabilities of nano-satellites and the historically traditional, full-scale satellites. As a consequence, CubeSats have become the object of interest of

a wide range of educational, commercial, and governmental organizations with over 300 launched since 2000 (Swartwout, n.d.).

1.2 ARAPAIMA Mission

One such program, sponsored by the Air Force Research Laboratory (AFRL), is the University Nano-Satellite Program (UNP). Originally conceived to participate in the 8th iteration of the UNP program, the ARAPAIMA mission proposes a reconnaissance approach to perform visible, infrared (IR), and 3D imaging of Resident Space Objects (RSOs) without a priori knowledge of their shape or attitude (Harris et al., 2013). This process follows a set of autonomous approach and close proximity maneuvers carried out with sufficient accuracy to allow rendezvous and docking maneuvers with the RSO.

The mission is carried out by a $12\,\mathrm{kg}$, $6\,\mathrm{U}$ ($36.6\,\mathrm{cm} \times 23.9\,\mathrm{cm} \times 27.97\,\mathrm{cm}$) CubeSat placed in low Earth orbit (LEO) at an altitude of approximately $500\,\mathrm{km}$ and a $28.5°$ inclination. The CubeSat is equipped with an imaging array consisting of an IR camera, a miniature laser rangefinder, and a visible light monochrome camera arranged such that their respective imaging directions are parallel to each other as shown in Figure 1.1.

To perform orbital approach maneuvers, the satellite is equipped with an R-134a cold gas propulsion system operated by means of rapid solenoid valve actuation using miniaturized 2D nozzles attached to the satellite body. The propulsion system is comprised of 16 reaction control system (RCS) thrusters set up in pairs, each one
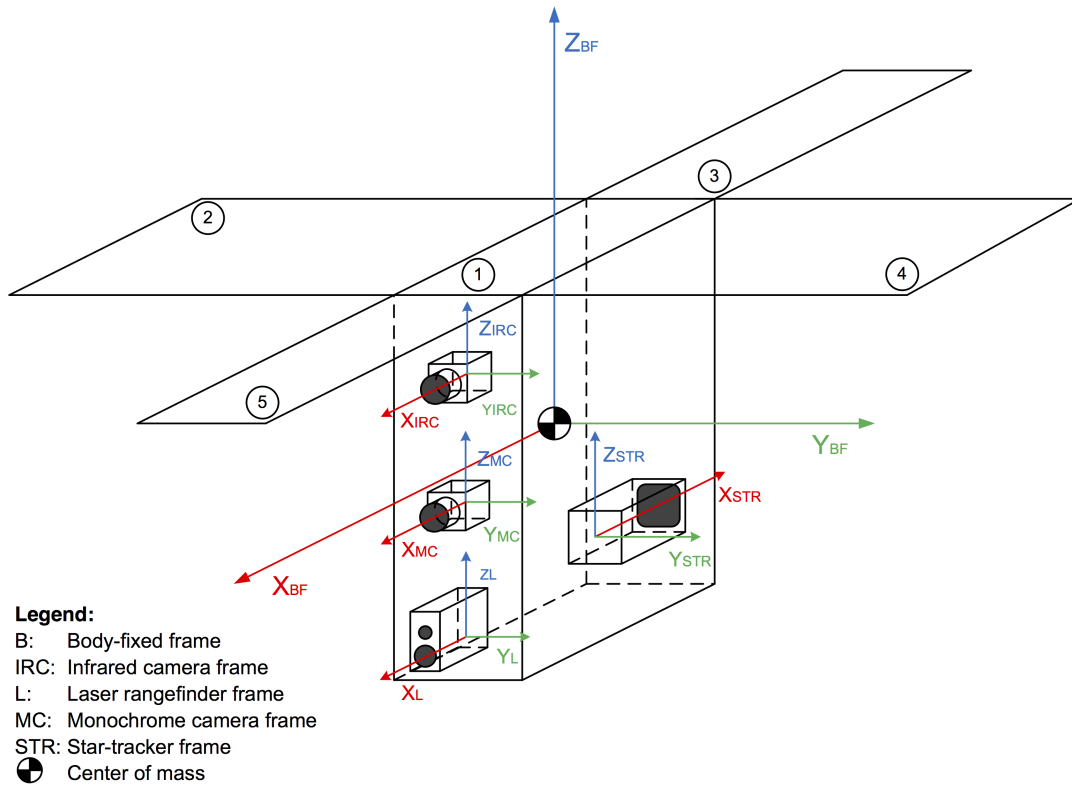
Figure 1.1. Imaging array placement on the satellite body. The x-axis on the satellite's body-fixed frame is defined as being parallel to the imaging direction.

capable of producing up to $25\,\mathrm{mN}$ of thrust. The nozzles are positioned such that a pure moment can be exerted about each body axis. With this configuration, four nozzles lie parallel to each other in both directions of the x and z body frame axes (Figure 1.2). These four nozzle clusters make up the orbital maneuvering thrusters (OMTs) and provide a total $100\,\mathrm{mN}$ of thrust.

Imaging constraints require the ADCS to maintain a pointing error of less than $1\,\mathrm{arcmin}$ at $3\,\sigma$ throughout all imaging procedures. This is the driving requirement for the design process presented in this thesis.
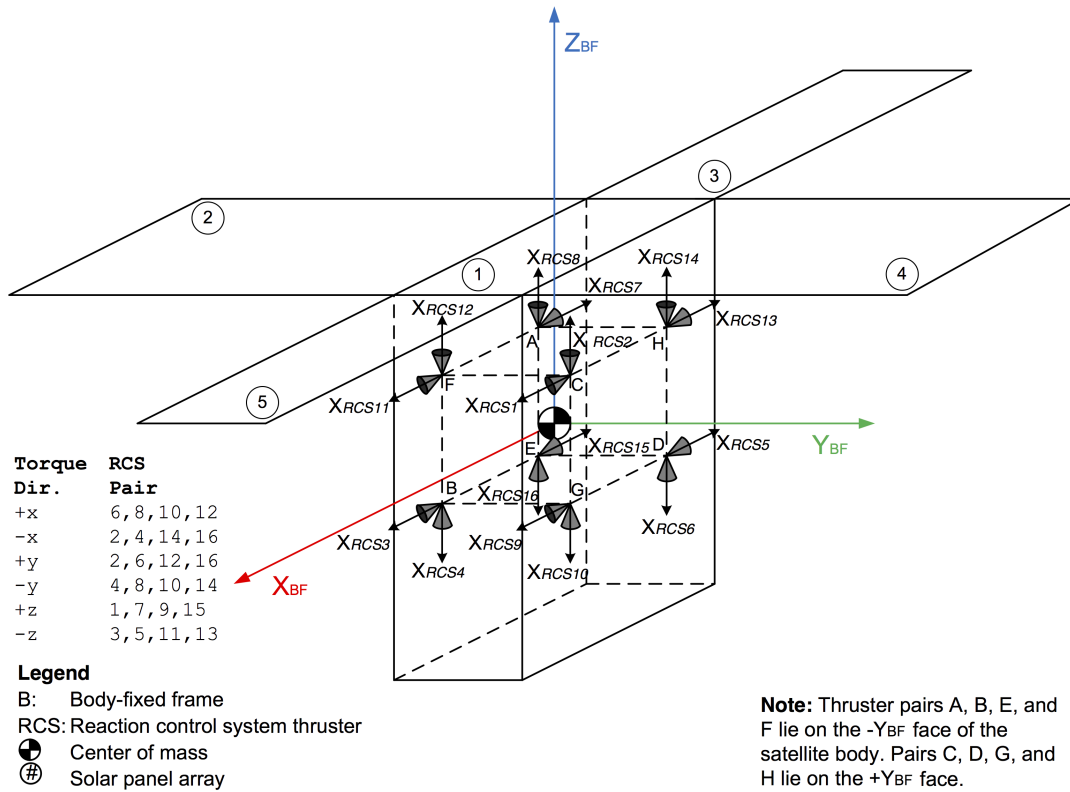
Figure 1.2. RCS thruster placement on satellite body-frame.

Attitude control is performed by operating the RCS thrusters in pairs to apply stabilizing moments. The thruster arrangement described above provides a full layer of attitude control redundancy, since the RCS system is able to operate with four nozzle pairs (pairs A B C D or E F G H in Figure 1.2).

The attitude determination system utilizes a combination of star tracker (STR) and angular rate gyro triad sensor readings to meet the pointing performance requirements. As a secondary attitude determination system, the satellite will also carry photo-diode sun sensors. These are used during operational modes in which the star tracker is

unable to provide an attitude solution such as detumbling maneuvers. An onboard GPS module is utilized to track the position of the satellite during orbital maneuvers and complement the communications array.

2. Dynamic Modeling

The satellite dynamics serving as the process or plant for the ADCS are modeled as a combination of attitude kinematics and orbital mechanics for a rigid body with six degrees-of-freedom (DOF). These are further augmented by a set of environmental models and conditions which contribute to the external disturbances acting on the satellite body. Sources of internal disturbances are also considered. In addition, detailed actuator models that capture the hardware operation and possible inaccuracies are included as part of the internal body dynamics.

2.1 Rigid Body Dynamics

The satellite body is treated as a rigid body with constant mass and moment of inertia (MOI). The forces and moments acting on the satellite's body fixed frame (defined as shown in Figure 1.2) are given by

$$\boldsymbol{F}_b = m(\dot{\boldsymbol{V}}_b + \boldsymbol{\omega} \times \boldsymbol{V}_b) + \boldsymbol{F}_d + \boldsymbol{F}_{cmd}, \tag{2.1}$$

$$\boldsymbol{M}_b = \boldsymbol{J}\dot{\boldsymbol{\omega}} + \boldsymbol{\omega} \times (\boldsymbol{J}\boldsymbol{\omega}) + \boldsymbol{M}_d + \boldsymbol{M}_{cmd}. \tag{2.2}$$

Where m and $\boldsymbol{V}_b$ are the body's mass and velocity respectively; $\boldsymbol{J}$ is a diagonal matrix containing the principal moments of inertia. All perturbing forces and moments acting on the system are taken into consideration through the $\boldsymbol{F}_d$ and $\boldsymbol{M}_d$ terms respectively, and are propagated through the integration of the angular velocity $\boldsymbol{\omega}$. Similarly, inputs are introduced through the $\boldsymbol{F}_{cmd}$ and $\boldsymbol{M}_{cmd}$ terms.

Changes to the satellite's configuration that occur throughout the mission, such as when appendages (solar panels, antennas, etc.) deploy, are modeled as impulsive changes in the body's moment of inertia. For the purpose of attitude control simulations, the mass flow rate of the propellant is assumed to be sufficiently small for the mass to be considered constant throughout imaging maneuvers.

2.2   Quaternion Kinematics

The attitude kinematics are described in terms of rotation quaternions. All quaternions referenced henceforth are considered to be normalized unit-quaternions and are defined as

$$\bar{\boldsymbol{q}} = \begin{bmatrix} q_0 \\ q_1 \\ q_2 \\ q_3 \end{bmatrix} = \begin{bmatrix} \cos(\phi/2) \\ \sin(\phi/2)\hat{e}_x \\ \sin(\phi/2)\hat{e}_y \\ \sin(\phi/2)\hat{e}_z \end{bmatrix} = \begin{bmatrix} \cos(\phi/2) \\ \sin(\phi/2)\hat{e} \end{bmatrix} = \begin{bmatrix} q_0 \\ \boldsymbol{q}_v \end{bmatrix}, \tag{2.3}$$

where $\hat{\boldsymbol{e}}$ is an arbitrary unit column vector and ϕ is an arbitrary angle through which a 3D frame is rotated about $\hat{\boldsymbol{e}}$.

The quaternion kinematic equation in terms of the inertially-referenced body angular velocity $\boldsymbol{\omega}$ is given by (Shuster, 1993) to be

$$\dot{\bar{q}} = \frac{1}{2}\bar{q} \otimes \bar{\boldsymbol{\omega}},\tag{2.4}$$

where $\otimes$ indicates quaternion multiplication, and $\bar{\boldsymbol{\omega}}$ is the "pure imaginary" quaternion equivalent of $\boldsymbol{\omega}$ defined as

$$\bar{\boldsymbol{\omega}} = [0, \omega_x, \omega_y, \omega_z]^T.\tag{2.5}$$

The matrix notation equivalent of Equation (2.4) is

$$\dot{\bar{q}} = \frac{1}{2}\Omega(\boldsymbol{\omega})\bar{q},\tag{2.6}$$

where

$$\Omega(\boldsymbol{\omega}) = \begin{bmatrix} 0 & -\omega_x & -\omega_y & -\omega_z \\ \omega_x & 0 & \omega_z & -\omega_y \\ \omega_y & -\omega_z & 0 & \omega_x \\ \omega_z & \omega_y & -\omega_x & 0 \end{bmatrix}.\tag{2.7}$$

Equations (2.1), (2.2) and (2.4) make up the full dynamics of the model and allow the satellite's state to be determined at any time t based on known initial conditions.

The attitude error of the body is also expressed in terms of quaternions. The error quaternion $\bar{q}_e$ of the satellite is defined as the quaternion which describes the rotation

from the current quaternion state to the command or reference quaternion $\bar{\boldsymbol{q}}_{cmd}$ and

is defined as

$$\bar{\boldsymbol{q}}_e = \begin{pmatrix} q_{0_e} \\ \boldsymbol{q}_{v_e} \end{pmatrix} = \bar{\boldsymbol{q}}_{cmd}^{-1} \otimes \bar{\boldsymbol{q}}. \tag{2.8}$$

A simpler attitude error representation, the pointing angle error, is defined as the

angle from the body x-axis (imaging direction) to the desired x-axis as given by the

error quaternion. It can be extracted from the direction cosine matrix resulting from

the quaternion triple product

$$\boldsymbol{w} = \bar{\boldsymbol{q}}\bar{\boldsymbol{v}}\bar{\boldsymbol{q}}^*, \tag{2.9}$$

where $\bar{\boldsymbol{q}}^*$ is the quaternion complex conjugate and $\bar{\boldsymbol{v}}$ is an arbitrary vector expressed

in the form of Equation (2.5). By factoring the $\bar{\boldsymbol{v}}$ terms, this can be further expanded

as

$$\boldsymbol{w} = \begin{bmatrix} (2q_0^2 - 1) & 0 & 0 \\ 0 & (2q_0^2 - 1) & 0 \\ 0 & 0 & (2q_0^2 - 1) \end{bmatrix} \begin{bmatrix} v_1 \\ v_2 \\ v_3 \end{bmatrix} + 2 \begin{bmatrix} q_1^2 & q_1 q_2 & q_1 q_3 \\ q_1 q_2 & q_2^2 & q_2 q_3 \\ q_1 q_3 & q_2 q_3 & q_3^2 \end{bmatrix} \begin{bmatrix} v_1 \\ v_2 \\ v_3 \end{bmatrix}$$
$$+ 2 \begin{bmatrix} 0 & -q_0 q_3 & q_0 q_2 \\ q_0 q_3 & 0 & -q_0 q_1 \\ -q_0 q_2 & q_0 q_1 & 0 \end{bmatrix} \begin{bmatrix} v_1 \\ v_2 \\ v_3 \end{bmatrix}, \tag{2.10}$$

then

$$
\boldsymbol{w} = \begin{bmatrix} 2q_0^2 + 2q_1^2 - 1 & 2q_1q_2 - 2q_0q_3 & 2q_1q_3 + 2q_0q_2 \\ 2q_1q_2 + 2q_0q_3 & 2q_0^2 + 2q_2^2 - 1 & 2q_2q_3 - 2q_0q_1 \\ 2q_1q_3 - 2q_0q_2 & 2q_2q_3 + 2q_0q_1 & 2q_0^2 + 2q_3^2 - 1 \end{bmatrix} \begin{bmatrix} v_1 \\ v_2 \\ v_3 \end{bmatrix}. \tag{2.11}
$$

The three-by-three matrix in Equation (2.11) is the direction cosine matrix which rotates the vector $\boldsymbol{v}$ in the frame. Substituting the unit quaternion norm

$$
1 = \sqrt{q_0^2 + q_1^2 + q_2^2 + q_3^2}, \tag{2.12}
$$

and taking the inverse cosine of the first term in Equation (2.11), results in the angle between the x-components of $\boldsymbol{v}$ and $\boldsymbol{\omega}$

$$
\psi = \arccos(q_0^2 + q_1^2 - q_2^2 - q_3^2). \tag{2.13}
$$

Substituting the quaternion error $\bar{\boldsymbol{q}}_e$ into Equation (2.9) and letting $\boldsymbol{v}$ be the body x-axis unit vector $\hat{\boldsymbol{x}}$, results in the pointing error es defined above

$$
\psi_e = \arccos(q_{0,e}^2 + q_{1,e}^2 - q_{2,e}^2 - q_{3,e}^2). \tag{2.14}
$$

2.3   Reference Frames

At this point it is useful to specify the reference frames utilized throughout the different models. The body-fixed frame (BFF) has already been defined as seen in Figures 1.1 and 1.2. The inertial frame or Earth-Centered Inertial (ECI) frame is

described by (Schutz, Tapley, & Born, 2004) as follows: the x-axis is aligned with the mean vernal equinox of the J2000 system and the z-axis is aligned with the Earth's angular velocity vector $\boldsymbol{\omega}_E$ as shown in Figure 2.1. The y-axis completes the right-handed coordinate system. This frame is used for all internal calculations throughout the models, and it serves as a reference point for transformations between different frames.
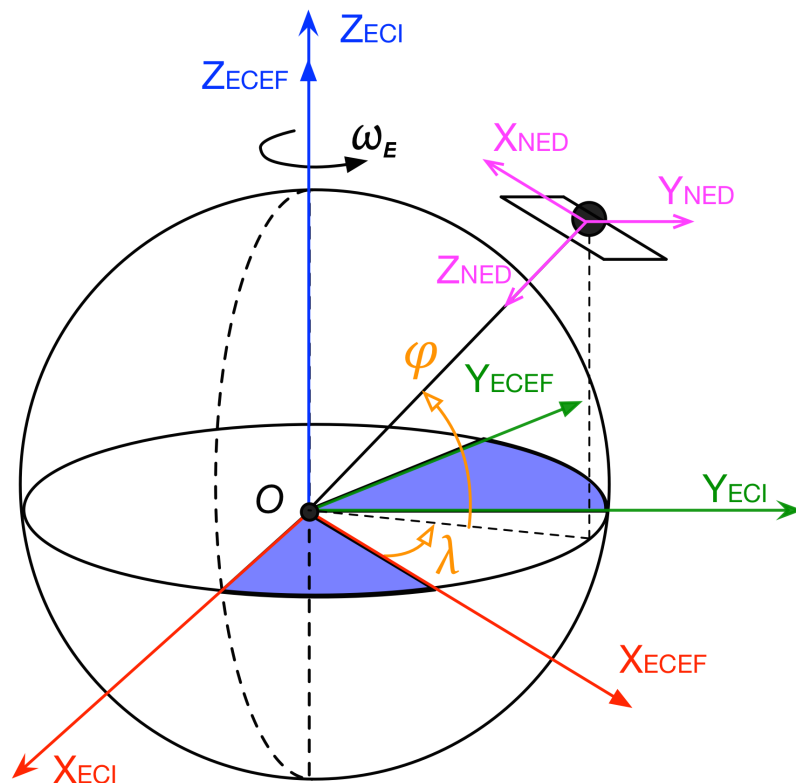
Figure 2.1. ECI, ECEF, and NED reference frames. The latitude (λ) and longitude (ϕ) convention for an arbitrary point over the Earth's surface with respect to the ECEF frame is shown.

Another useful frame is the Earth-Centered Earth-Fixed (ECEF) frame, which rotates with the Earth. Its x-axis points to the (0°, 0°) point on the Earth's graticule

and the z-axis points due North. It should be noted, however, that the z-axis does not lie perfectly along $\boldsymbol{\omega}_e$ due to polar motion.

Finally, some environmental models provide information on the North-East-Down (NED) frame, a type of non-inertial, local tangent plane (LTP) reference system usually used for aircraft navigation. In this system, the x-axis points to the polar North (parallel to the LTP) while the z-axis points downward (nadir), towards the Earth's surface. The y-axis completes the right-handed frame and points East on the LTP (Figure 2.1). Note that while the center of the NED frame is dependent on the body's location (relative to ECEF), the frame is not a body-fixed frame. Further frames and conventions are defined in Appendix A.

2.4   Environmental Disturbances

To account for environmental conditions, a set of models is set parallel to the dynamic equations discussed above. These models shape the disturbance moments and forces acting on the system to mirror those of the ARAPAIMA mission scenario. At the expected 500 km altitude, the effects of Earth's gravitational and magnetic field as well as its atmosphere are non-negligible (Wertz, Everett, & Puschell, 2011). Therefore, they form the dominant aspect of the plant model.

2.4.1 Aerodynamic Drag

At LEO, the atmospheric density and composition have a direct impact on the satellite's attitude especially when one considers its low mass and the size of the solar panels relative to the body. Using the Mass Spectrometer and Incoherent Scatter Radar Extended 1990 (MSISE90) atmospheric model it is possible to estimate the density, temperature, and composition of the atmosphere as well as the number densities of its components at a specified altitude on the ECEF frame (Hedin, n.d.). Data from the Naval Research Laboratory Mass Spectrometer and Incoherent Scatter Radar Extended 2000 (NRLMSISE00) model, an updated version of the MSISE90 model, is also used since it contains additional data on Oxygen particles at altitudes above 500 km (Picone, Hedin, & Drob, n.d.).

Aerodynamic torques are produced by the atmospheric particles colliding with the satellite surface. Collisions occur at a higher frequency during maximum solar activity resulting in larger disturbances. This worst case scenario has been assumed for all aerodynamic calculations. The aerodynamic torques acting on the satellite are estimated by Equation (2.15)

$$\boldsymbol{M}_{aero} = \frac{1}{2}\rho \text{diag}(\boldsymbol{V}_{\infty}^2)\boldsymbol{C}_M A l_{ref}, \qquad (2.15)$$

where ρ is the mass density, $\boldsymbol{V}_{\infty}$ is the freestream velocity, $\boldsymbol{C}_M$ is the moment coefficient vector, A is the projected surface area, and l_{ref} is the body reference length. Table 2.1 summarizes the values assigned to each constant.

Table 2.1. Parameters and constants used to calculate the aerodynamic drag disturbance torque.

Parameter	Symbol	Value	Units
Projected Area	A	26.06×10^{-2}	$\mathrm{m^2}$
Reference length	l_{ref}	0.1	m
Mass density	ρ	1.02×10^{-11}	$\mathrm{kg\,m^{-3}}$
Freestream velocity	$\boldsymbol{V_\infty}$	$7.612\hat{\boldsymbol{e}}$	$\mathrm{km\,s^{-1}}$
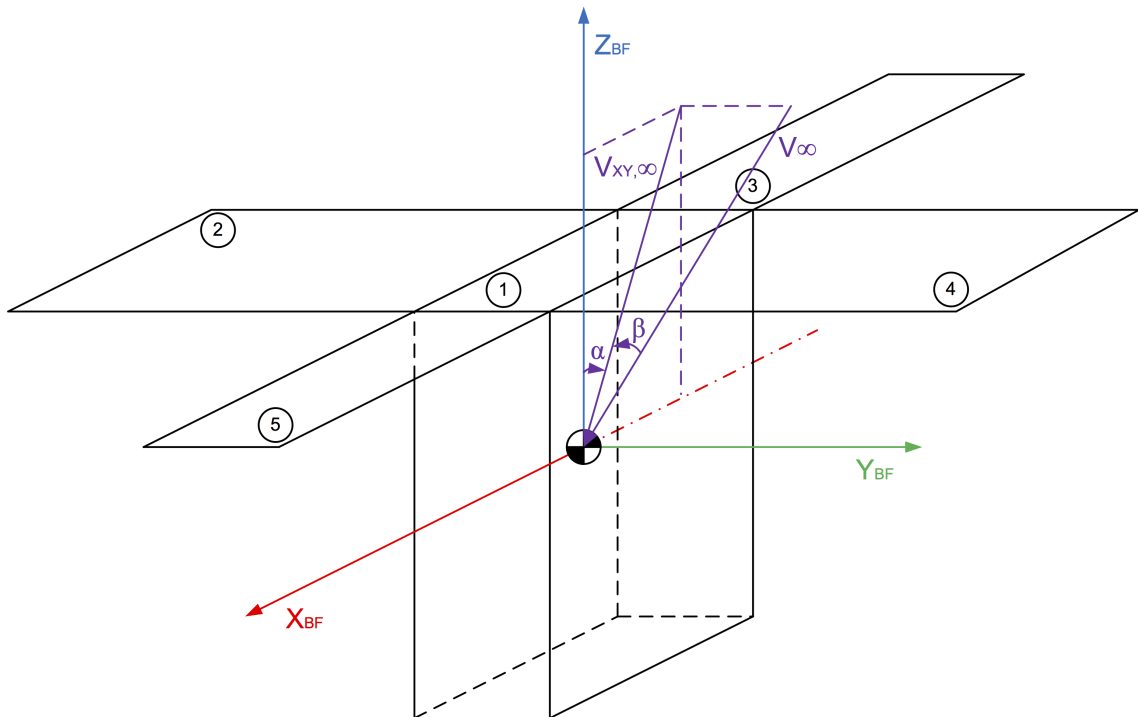
Figure 2.2. Angle of attack (α) and angle of slip (β) definitions for the aerodynamic drag on the satellite body-frame. These provide the orientation for the flow direction in the DSMC iteration results.

At a nominal altitude of $500\,\mathrm{km}$ the NRLMSISE00 model gives an atmospheric composition of 94% O and 6% N with a number density of $n = 3.769 \times 10^{14}\,\mathrm{m^{-3}}$ at a temperature of $1491\,\mathrm{K}$. The mean free path between particles $\lambda = 27.33\,\mathrm{km}$, which compared with a reference length l_{ref} of $0.1\,\mathrm{m}$ (taken to be approximately one-third

of the maximum body dimension as suggested by (Wertz et al., 2011)) results in a Knudsen number, $K_n = \lambda/l_{ref} = 273300$ (Lyle & Stabekis, 1971). This indicates the satellite operates in the free molecular flow regime.

Given the previous statement, the moment coefficients $\boldsymbol{C}_M = [C_{M_x}, C_{M_y}, C_{M_z}]^T$ of the satellite were calculated using the direct solution Monte Carlo (DSMC) program DAC97, which employs algorithms based on the methods described by (Bird, 1994). A variable hard sphere model has been assumed for the collisions between the particles (O and N) and the satellite. $V_\infty = ||\boldsymbol{V}_\infty||$ has been assumed to be $7.612\,\mathrm{km\,s^{-1}}$, which is equivalent to the mean orbital speed.

A total of 1369 runs of the DAC97 code have been performed on the ARAPAIMA body geometry for 37 different α and β values. The angle of attack was varied between $-90°$ and $90°$ in steps of $5°$; the sideslip angle was similarly varied between $0°$ and $180°$ (the angle of attack and the sideslip angle are defined as seen in Figure 2.2). The DSMC results are used to form 2D look-up tables which map the drag and moment coefficients as functions of α and β as shown in Figure 2.3. Together with the total mass density obtained from the MSISE90 model, Equation (2.15) is used to calculate the aerodynamic disturbance torques at any orientation (Figure 2.4). The maximum force coefficient corresponding to the drag coefficient in general aerodynamic terms is approximately 2.0, which is within the expected range (2.0-2.2) for small satellites in LEO (Wertz et al., 2011).
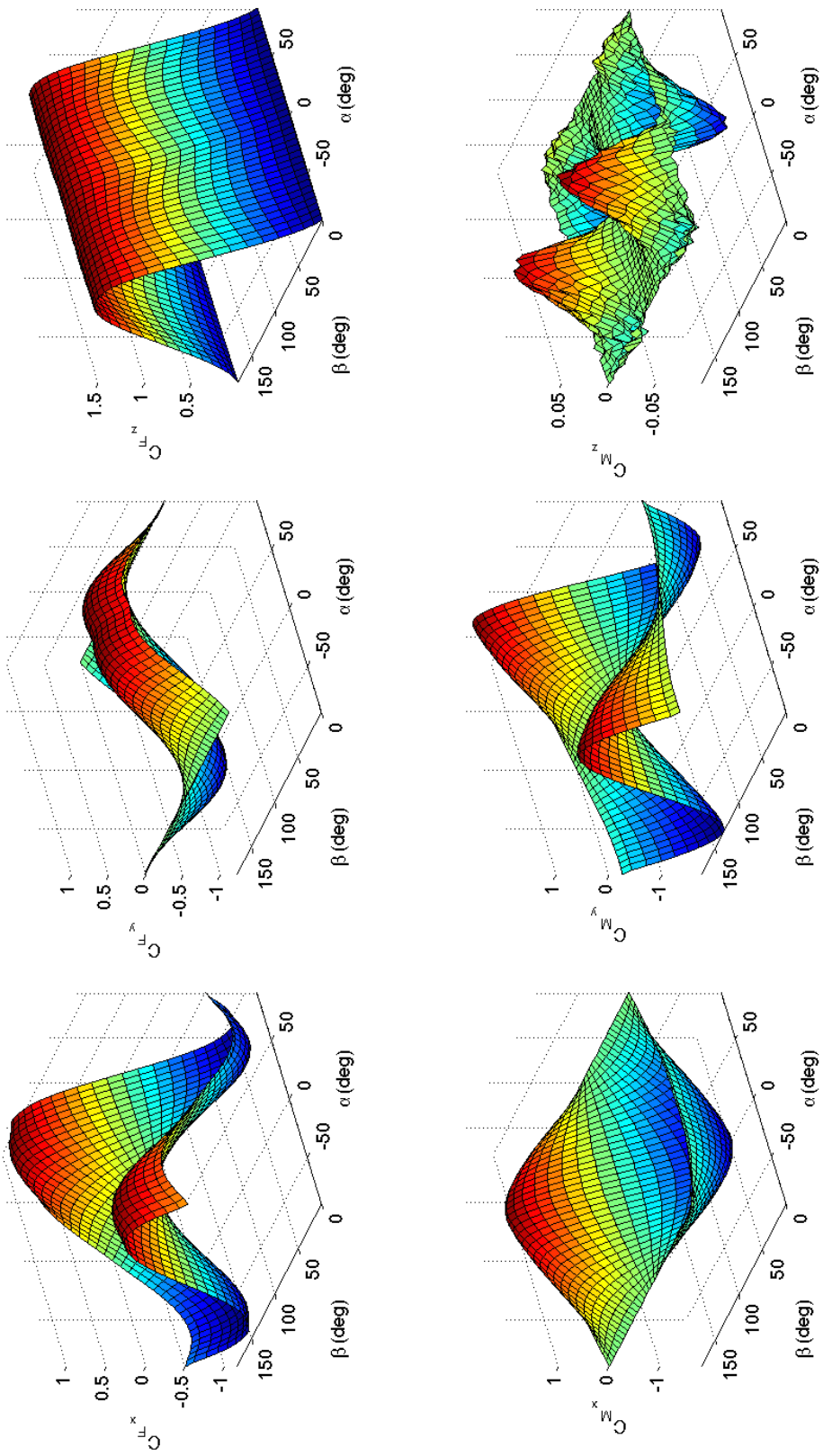
Figure 2.3. Force and moment coefficients of the ARAPAIMA satellite as functions of its orientation in terms of α and β. The first three plots describe the change of the force coefficient in the x, y, and z body-axes respectively. The following three plots do the same for the moment coefficients.
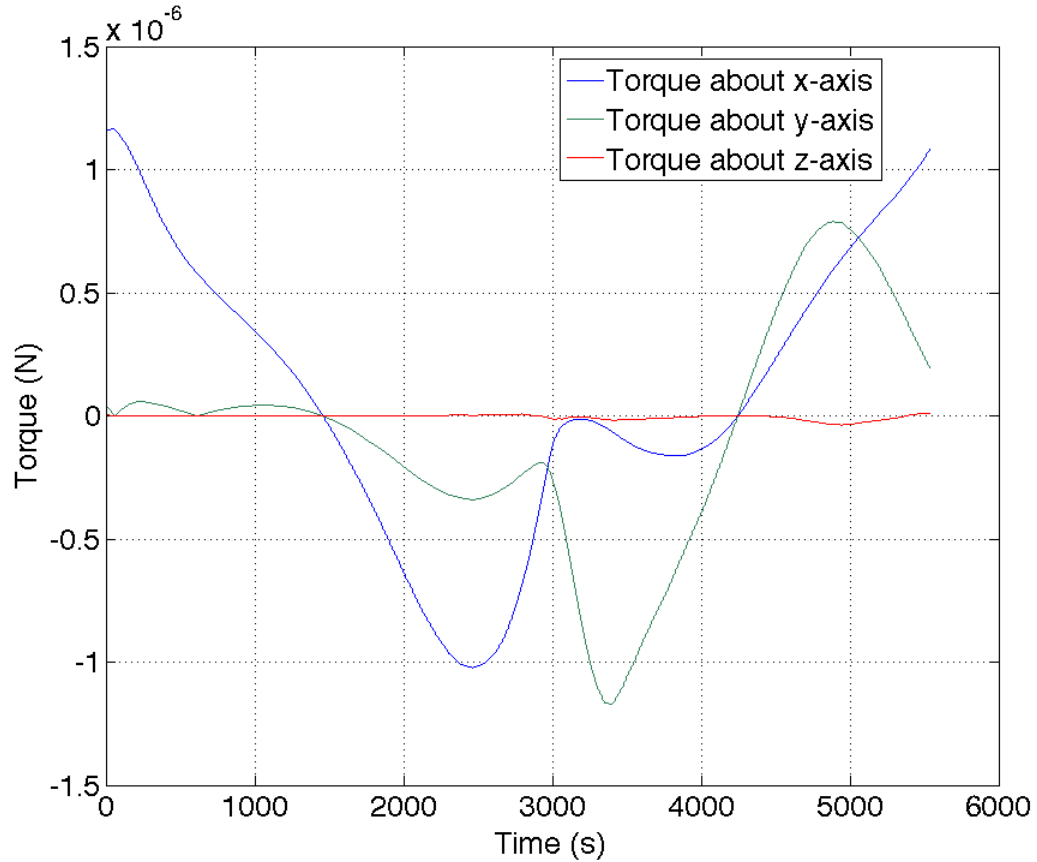
Figure 2.4. Aerodynamic disturbance torques acting on the satellite body during one orbit at a 500 km altitude and 28.5° inclination.

2.4.2 Magnetic Residual

The magnetic disturbance torque has two major sources: the force produced on a point charge by the magnetic component of the Lorentz force, and the torque experienced by an aspherical paramagnetic body which, in the absence of other torques, aligns its long axis with the local magnetic field. This means that all electrically conducting parts of the satellite contribute charges and produce time varying magnetic

fields. Due to the complex nature of evaluating these disturbance torques, empirical data is used to estimate their effect.

The Earth's magnetic field $\boldsymbol{B}_E$ is predicted using the 2010-2015 World Magnetic Model (WMM), which provides magnetic intensity, inclination, declination, and a complete geometry of the field at any point in a $-1\,\mathrm{km}$ to $850\,\mathrm{km}$ range (z-direction) in the NED frame (Maus et al., 2010). An estimate of the maximum magnetic torque can then be obtained by merging all contributing magnetic effects into a residual dipole moment specific to the satellite body and exposing it to the environmental magnetic field (Wertz et al., 2011; Inamori, Sako, & Nakasuka, 2011)

$$\boldsymbol{M}_{rmm} = \boldsymbol{m}_{rmm} \times \boldsymbol{B}_E. \tag{2.16}$$

For the ARAPAIMA satellite, the magnetic dipole moment $\boldsymbol{m}_{rmm}$ is approximated to be $0.1\,\mathrm{A\,m^2}$ and aligned with the body y-axis thus $\boldsymbol{m}_{rmm} = [0, 0.1, 0]^T$. The resulting $\boldsymbol{M}_{rmm}$ is calculated as shown in Figure 2.5.
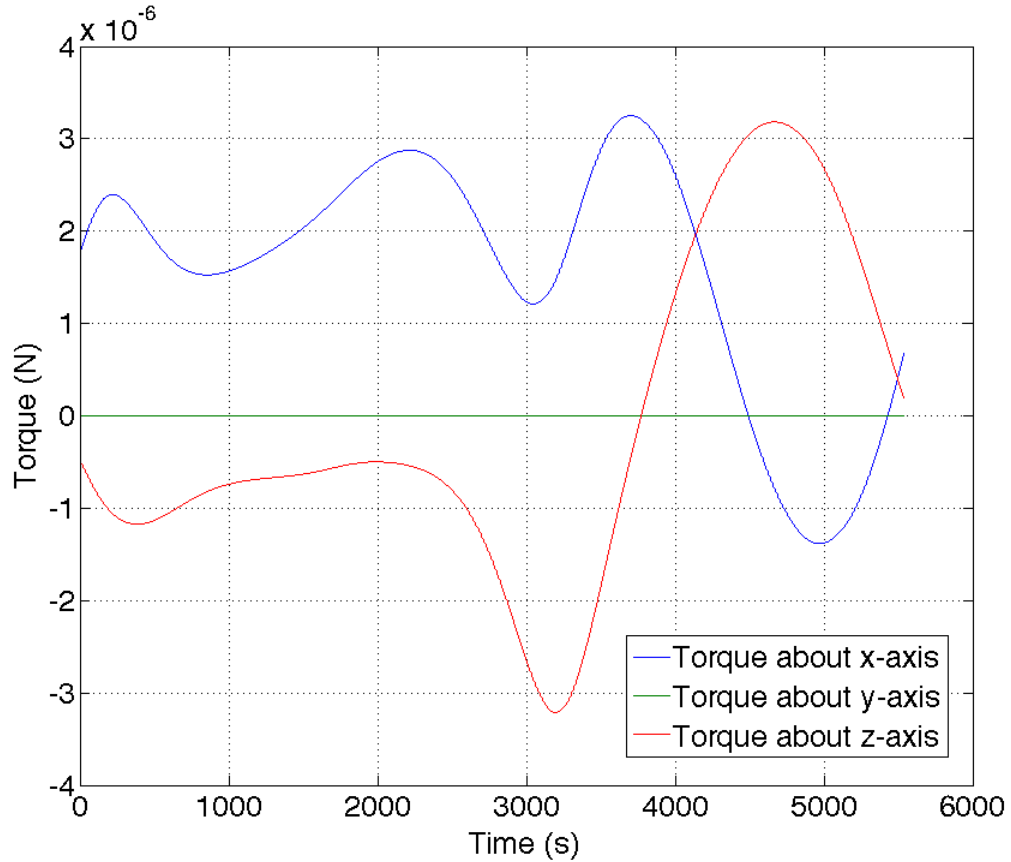
Figure 2.5. Magnetic disturbance torques acting on the satellite body during one orbit at a 500 km altitude and 28.5° inclination.

2.4.3   Gravity Gradient

In order to have the body follow an orbital trajectory, a gravitational model of Earth is used to determine the force acting on the satellite at any point in time. The model implements the mathematical representation of the geocentric equipotential ellipsoid described by the World Geodetic System 1984 (WGS84) (MathWorks, 2013).

When the center of mass of a satellite does not coincide with its center of gravity, the variation of the Earth's gravitational field over the volume of the spacecraft

produces torques which, in the absence of other disturbances, will try to align one of the body's principal axes with the local gravity field vector (Curtis, 2013). This disturbance is given by

$$\boldsymbol{M}_{gg} = \frac{3\mu}{||\boldsymbol{r}||^3}(\hat{\boldsymbol{r}}) \times \boldsymbol{J}\hat{\boldsymbol{r}}, \tag{2.17}$$

where $\boldsymbol{r}$ is the satellite position in the ECI frame. The gravity gradient disturbance contribution to the attitude dynamics are calculated by evaluating Equation (2.17) along the satellite's trajectory. The resulting moments are shown in Figure 2.6.
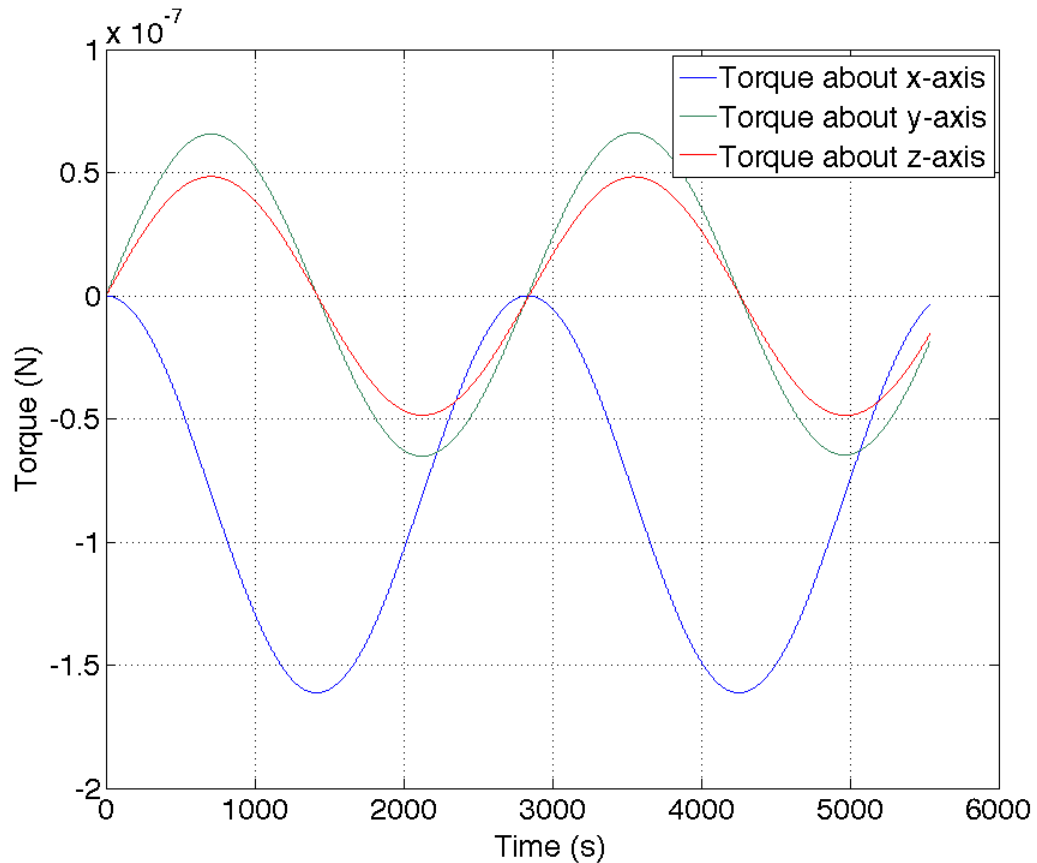
Figure 2.6. Gravity gradient disturbance torques acting on the satellite body during one orbit at a 500 km altitude and 28.5° inclination.

2.4.4 Solar Radiation Pressure

When solar photons collide with a satellite, the momentum exchange between sunlight and the body surface results in a net pressure force called solar radiation pressure (SRP). This pressure is a complex function of the shape and optical properties of the satellite as well as the shading and solar intensity $\mathbf{\Phi}$. The worst case scenario is given by Equation (2.18) where $\mathbf{\Phi}$ is taken from an Systems Tool Kit (STK) simulation for the day of January 1st, 2015

$$\boldsymbol{M}_{srp} = \frac{\mathbf{\Phi} f_s S_s (1 + \zeta) l_s}{c}. \tag{2.18}$$

The resulting $\boldsymbol{M}_{srp}$ is shown in Figure 2.7. Note that the disturbances disappear during the eclipse portion of the orbit. Additional parameters are listed in Table 2.2.

Table 2.2. Parameters and constants used to calculate the SRP disturbance torque.

Parameter	Symbol	Value	Units
Surface area	S_s	12.21×10^{-2}	m^2
Moment arm	l_s	0.1	m
Reflectance factor	ζ	0.6	-
Average solar constant	f_s	1366	$W\,m^{-2}$
Speed of light	c	3×10^{-8}	$m\,s^{-2}$
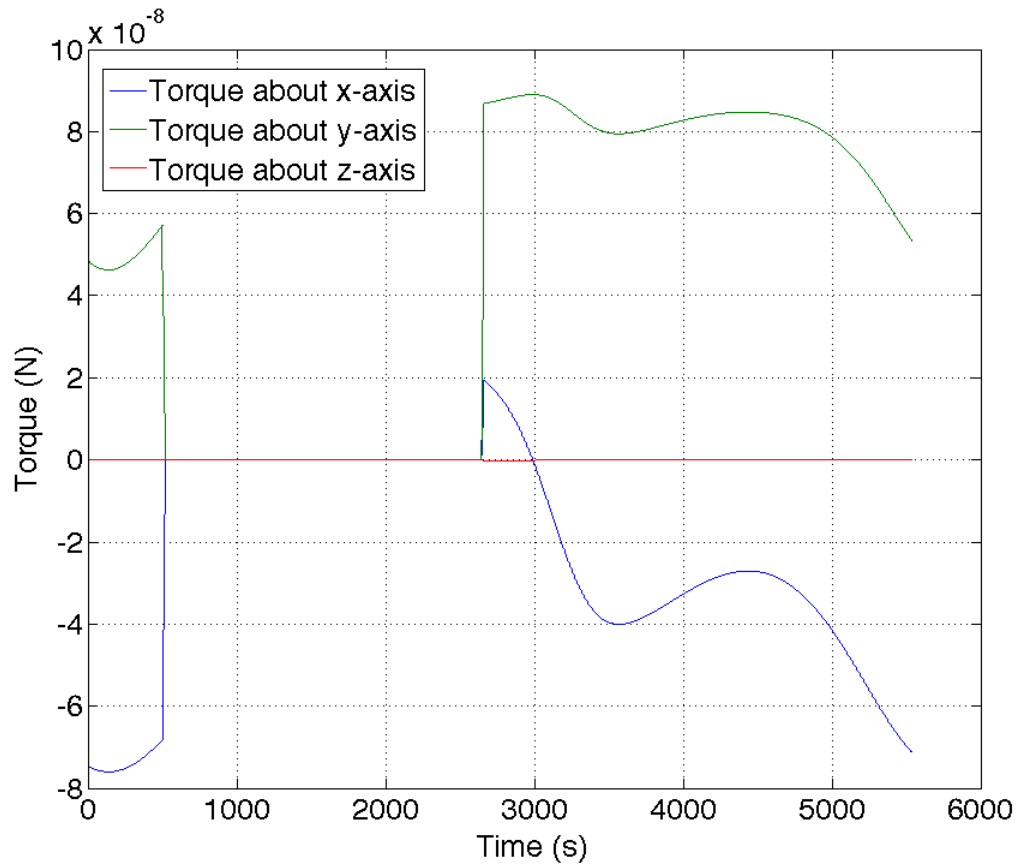
Figure 2.7. Solar radiation pressure disturbance torques acting on the satellite body during one orbit at a 500 km altitude and 28.5° inclination.

2.5 Internal Disturbances

External factors are not the only sources of disturbances for a satellite; moving parts and other mechanical interfaces also produce undesirable torques. Many of these internal disturbances are also produced or exacerbated as a result of active control. Because there is no ideal way to mitigate them, the controller must be able to minimize both external and internal torques.

2.5.1 Solar Panel Hinges

The solar panel hinges are loaded with torsion springs held by burn wire release mechanisms which control the panel deployment. In order for the rigid body dynamics outlined in Section 2.1 to be valid, the flexible joints must be modeled such that any moment or force resulting from their movement can be incorporated into the pre-existing dynamic equations. Assuming the solar panel themselves are inflexible, the satellite can be analyzed as a system of rigid bodies with torsion spring joints. Consider a single panel, connected to the main body by a spring-loaded hinge described by the second order mass-spring-damper equation

$$\boldsymbol{M}_{sp} = \boldsymbol{J}_{sp}\ddot{\boldsymbol{\theta}}_{sp} + b\dot{\boldsymbol{\theta}}_{sp} + k\boldsymbol{\theta}_{sp}. \tag{2.19}$$

Where $\boldsymbol{M}_{sp}$ is the input torque, $\boldsymbol{J}_{sp}$ is the panel's moment of inertia, $\boldsymbol{\theta}_{sp}$ is the spring's angular position, and b and k are the damping and spring coefficients respectively. The input from the actuators results in a moment $\boldsymbol{M_{act}}$ about the main body center of mass. This moment is, in turn, opposed by the body's angular acceleration such that

$$\boldsymbol{T}_{sp} = \boldsymbol{M}_{act} - \boldsymbol{J}_b\ddot{\boldsymbol{\theta}}_b. \tag{2.20}$$

Then the spring interaction with the rest of the body can be analyzed over time according to

$$\boldsymbol{M}_{act} - \boldsymbol{J}_b\ddot{\boldsymbol{\theta}}_b = \boldsymbol{J}_{sp}\ddot{\boldsymbol{\theta}}_{sp} + b\dot{\boldsymbol{\theta}}_{sp} + k\boldsymbol{\theta}_{sp}. \tag{2.21}$$

Where the subscript b indicates the quantities corresponding to the satellite body.

This analysis is then extended to account for all four solar panels simultaneously. The resulting torques $\boldsymbol{M_{sp}}$ can now be added to Equation (2.2) as superimposed disturbances. Although small in comparison to the external disturbances, modeling this reaction is important in order to monitor and avoid exciting structural modes through control actuation (Section 2.6.2). Based on the spring properties outlined in Table 2.3, the damped frequency of the solar panel hinges

$$f_d = \frac{1}{2\pi}\sqrt{\frac{k}{J} - \left(\frac{b}{2J}\right)^2},$$
(2.22)

is determined to be an average of 27 Hz.

Figure 2.8 shows the disturbance of a single panel due to angular acceleration of the spring load. During deployment, the superimposed moments of the different panels cancel each other. Table 2.3 shows the different spring properties for each panel.

Table 2.3. Properties and constants of the individual solar panel hinges. Spring and damping coefficients were approximated from deployment video demonstrations. The directions in parenthesis indicate in which body face the panel is located.

	Symbol	6 U (+Y/-Y)	3 U (+X/-X)	Units
Spring coefficient	k	100/90	100/110	$\mathrm{N\,m\,rad^{-1}}$
Damping coefficient	b	0.1/0.09	0.1/0.11	$\mathrm{N\,m\,s\,rad^{-1}}$
Inertial load	J_{sp}	$(3.5/3.55)\times10^{-3}$	$(1.6/1.55)\times10^{-3}$	$\mathrm{kg\,m^2}$
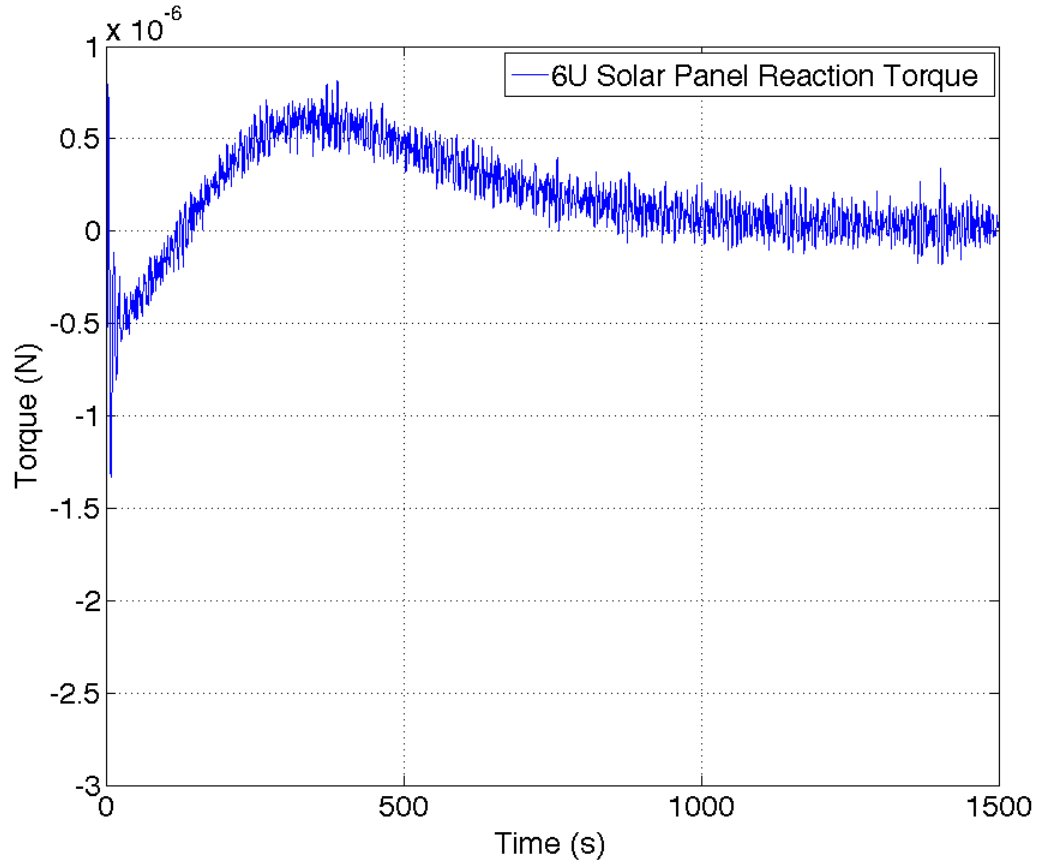
Figure 2.8. Solar panel hinge disturbance moment. The initial offset of is due to the initial acceleration of the satellite and deployment of the solar panel

2.5.2   Propellant Slosh

Even in microgravity, liquid propellant slosh contributes directly to attitude destabilization. In the case of the ARAPAIMA mission, slosh can hinder mission completion by introducing unwanted angular momentum which could result in a deviation from trajectory during orbital maneuvers or in oscillations of the pointing axis which prevent sufficiently stable imaging. For this reason, a simple yet fairly accurate mass-spring-damper equivalent mechanical model was incorporated in the

simulation. A detailed analysis of this mechanical model designed specifically for the ARAPAIMA mission was carried out by (Vazquez, 2014). A summary of the resulting moment equation and parameters follows.

The model takes into account the propellant's behavior through the Weber, Froude and Bond numbers and is described by Equation (2.23) in terms of angular and linear displacements as proposed by (Dodge, 2010)

$$M_{sl} = -(J_{x,0} + m_{sl,0}H_0^2)\alpha_{sl} - \sum_0^n m_{sl,n}H_{sl,n}(\ddot{x}_{sl,n} + H_{sl,n}\alpha_{sl,0}) + g\sum_0^n m_{sl,n}x_{sl,n}. \quad (2.23)$$

Where $J_{x,0}$, H_0, and $\alpha_{sl,0}$ are the respective moment of inertia, position, and angular acceleration of the stationary propellant mass $m_{sl,0}$. $x_{sl,n}$ indicates the position of the nth moving propellant mass $m_{sl,n}$ along the spring direction, whereas $H_{sl,n}$ indicates the position along the tank's length. For micro-gravity scenarios, g represents the translational thrust applied by the satellite. Figure 2.9 shows a second order ($n=2$) representation of Equation (2.23).

Note that due to the nature of the mass-spring-damper representation, Equation (2.23) needs to be modified according to the expected motion along each axis (especially depending on the alignment of the thrusters). The x-axis implementation is given above. The output on all three axes for one orbit with a 65% propellant fill ratio can be seen in Figure 2.10. Table 2.4 shows the parameters corresponding to Equation (2.23) for a first mode model ($n=1$) with zero initial acceleration.
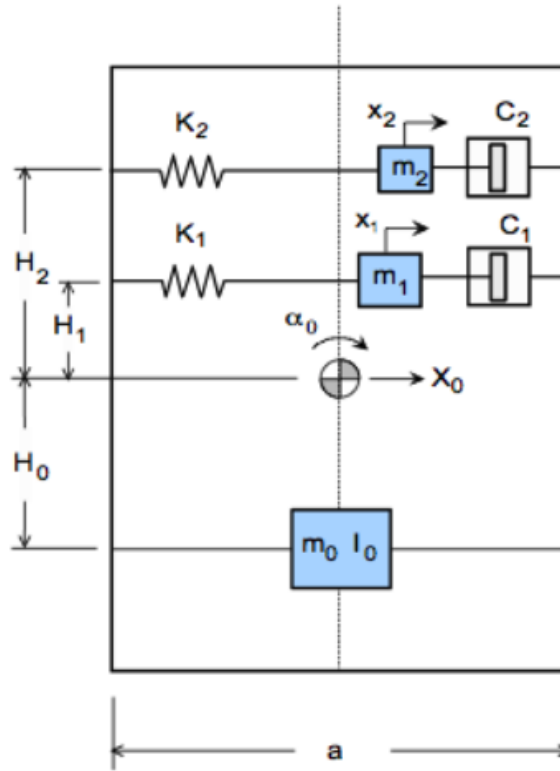
Figure 2.9. Propellant slosh model diagram indicating a second order mass model within a rectangular tank (Dodge, 2010).

Table 2.4. Parameters for a first mode slosh propellant slosh simulation at 65% propellant fill ratio.

Fill ratio		65%	Units
Linear acceleration	$\ddot{x}_{sl,n}$	0	$\mathrm{m\,s^{-2}}$
Height of fluid	h	0.550	m
Tank width	a	0.214	m
Oscillating mass	m_1	0.695	kg
Stationary mass	m_0	0.341	kg
Initial position of m_0	H_0	0.014	m
Initial position of m_1	H_1	0.029	m
Moment of Inertia	$J_{x,0}$	0.289×10^{-3}	$\mathrm{kg\,m^2}$
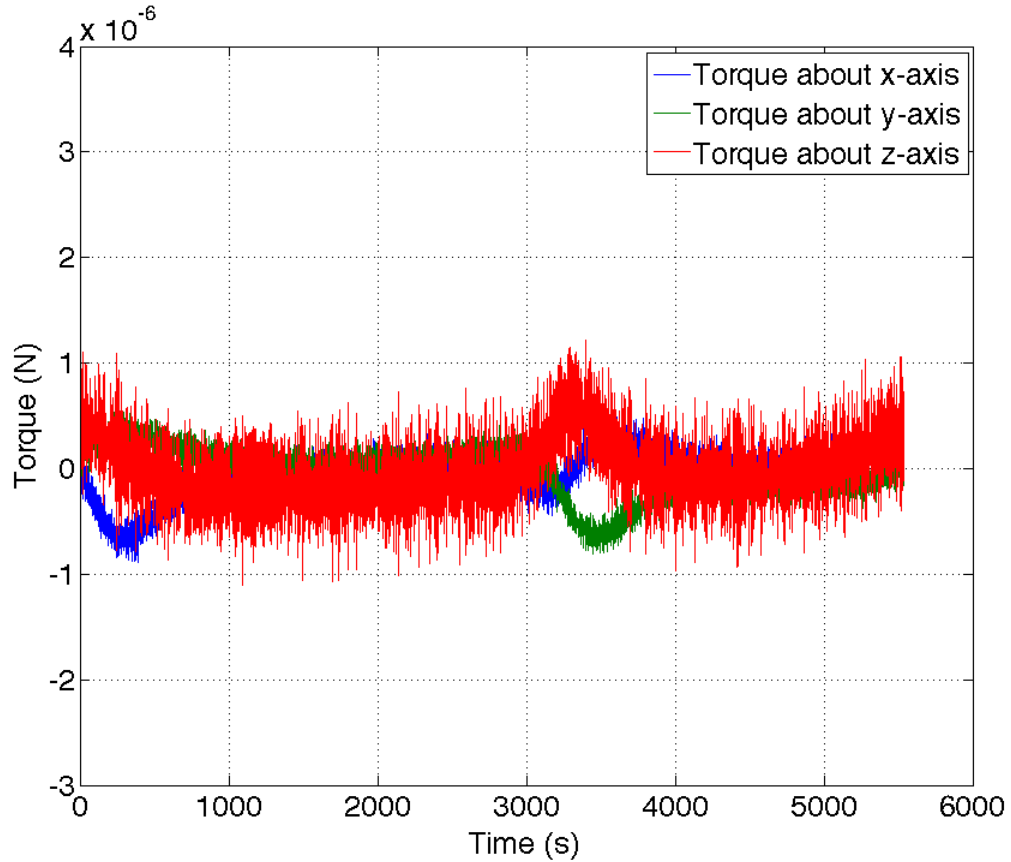
Figure 2.10. Propellant slosh disturbance moment.

2.6 Actuators

Originally the ARAPAIMA mission relied on reaction wheels (RW) to perform attitude control; however, these are still dependent on the RCS thrusters to periodically despin the flywheels. This dependency coupled with mass and volume constraints led to descoping the reaction wheels in favor of an RCS thruster actuated control system. A trade study which compares the attitude performance, propellant consumption, and

electrical energy requirements of each actuator configuration is presented to justify the decision.

2.6.1 Reaction Wheels

The RW model is based on the standard model of a brushed DC motor subjected to static and dynamic imbalances. The physical properties of Sinclair Interplanetary RW-0.03-4 flywheels were used to model the RW assembly (detailed in Table 2.5). These are mounted so each RW's spin axis is aligned with a particular body axis. The generic open loop transfer function of a DC motor (neglecting friction and armature inductance) is given by

$$\frac{\Omega_{rw}}{V} = \frac{K_m}{(R_m J_{rw})s + K_m^2}. \tag{2.24}$$

Where Ω_{rw} and V are the respective angular speed and voltage of the motor in the Laplace domain. R_m, K_m and J_{rw} are the armature resistance, motor constant, and moment of inertia respectively. s is the Laplace domain complex number frequency.

Additional disturbance torques due to the static and dynamic imbalances of the flywheels are modeled as functions of the angular velocity $\omega_{rw,n}$ and imbalance constants $U_{s,n}$ and $U_{d,n}$ as described by (Liu, 2007)

$$\boldsymbol{M}_{U_s} = \boldsymbol{R}_w \times \begin{bmatrix} U_{s,y}\omega_{rw,y}^2 \sin(\omega_{rw,y}t) + U_{s,z}\omega_{rw,z}^2 \sin(\omega_{rw,z}t) \\ U_{s,z}\omega_{rw,z}^2 \sin(\omega_{rw,z}t) + U_{s,x}\omega_{rw,x}^2 \sin(\omega_{rw,x}t) \\ U_{s,x}\omega_{rw,x}^2 \sin(\omega_{rw,x}t) + U_{s,y}\omega_{rw,y}^2 \sin(\omega_{rw,y}t) \end{bmatrix}, \tag{2.25}$$

$$\boldsymbol{M}_{U_d} = \begin{bmatrix} U_{d,z}\omega_{rw,z}^2 \sin(\omega_{rw,z}t) - U_{d,y}\omega_{rw,y}^2 \sin(\omega_{rw,y}t) \\ U_{d,x}\omega_{rw,x}^2 \sin(\omega_{rw,x}t) - U_{d,z}\omega_{rw,z}^2 \sin(\omega_{rw,z}t) \\ U_{d,y}\omega_{rw,y}^2 \sin(\omega_{rw,y}t) - U_{d,x}\omega_{rw,x}^2 \sin(\omega_{rw,x}t) \end{bmatrix}. \tag{2.26}$$

A PI controller is added to Equation (2.24), resulting in the closed loop reaction wheel model

$$\frac{\Omega_{rw}}{R} = \frac{K_m(k_{p,rw}s + k_{i,rw})}{(J_{rw}R_m)s^2 + K_m(k_{p,rw} + K_m)s + K_m k_{i,rw}}, \tag{2.27}$$

where $k_{i,rw}$ and $k_{p,rw}$ are the integral and proportional control gains respectively.

The resulting torque applied to the body is a function of the RW angular momentum $\boldsymbol{H_{rw}}$ and dependent imbalances

$$\boldsymbol{M}'_{rw} = \boldsymbol{\omega}_{rw} \times \boldsymbol{H}_{rw} + \boldsymbol{M}_{U_s} + \boldsymbol{M}_{U_d}. \tag{2.28}$$

Table 2.5. Reaction wheel model physical constants and control gains.

Parameter	Symbol	Value	Units
Moment of inertia	J_{rw}	5.109×10^{-5}	$\text{kg}\,\text{m}^2$
Armature Resistance	R_m	2.9	Ω
Motor torque constant	K_m	1.12×10^{-3}	$\text{N}\,\text{m}\,\text{A}^{-1}$
Nominal momentum	h_{max}	4.28×10^{-2}	$\text{N}\,\text{m}\,\text{s}$
Dynamic imbalance coefficient	U_d	1.00×10^{-10}	$\text{N}\,\text{m}\,\text{s}^2$
Static imbalance coefficient	U_s	5.00×10^{-10}	$\text{N}\,\text{s}^2$
Proportional gain	$K_{p,rw}$	1.65	-
Integral gain	$K_{i,rw}$	54.76	-

2.6.2 RCS Thrusters

The RCS thruster model utilizes pulse width modulated (PWM) signals to accurately represent rapid valve actuation. The PWM command regulates the torque applied to the body and approximates a 'throttleable' actuator. The throttle action is linear over the entire operational range for a set of user specified frequencies (approximately 1 Hz to 100 Hz as shown in Figure 2.11), at increments of 1% of the maximum thrust (Huang, 2014).
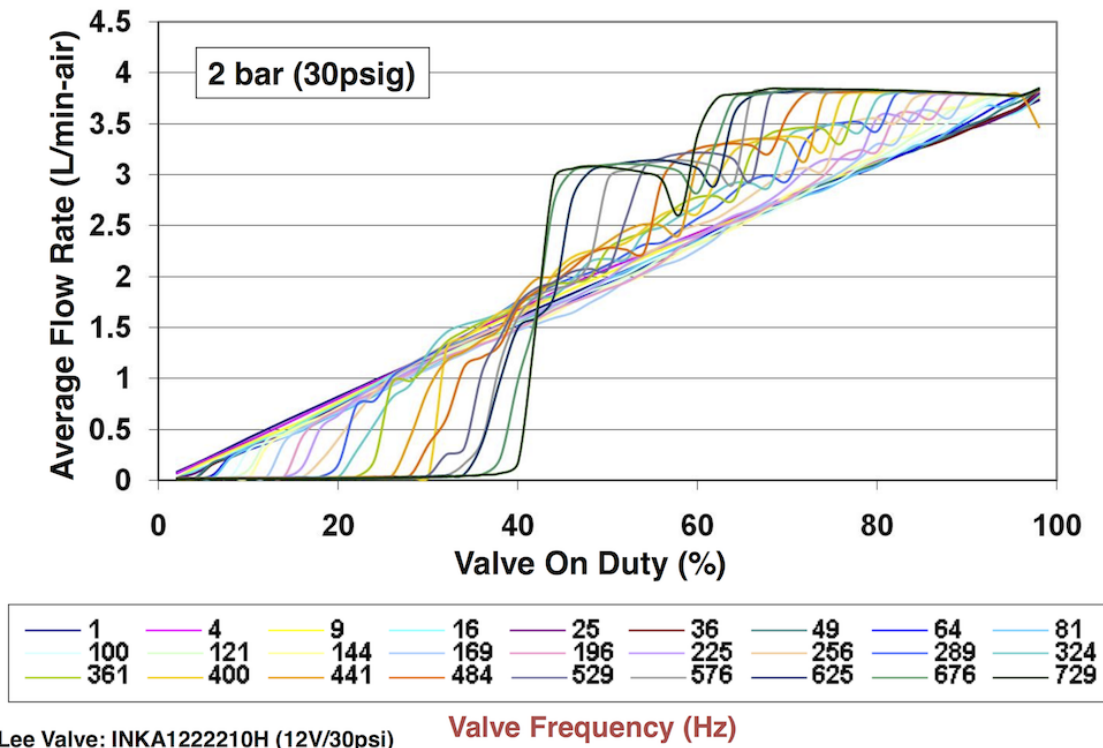
Figure 2.11. Thrust command (top) and resulting valve operation signal (bottom).

Keeping the frequency constant, it is possible to produce the average desired thrust value over time by controlling the signal duty cycle. The amount of time the

valve remains open t_{rcs} is proportional to the ratio of the desired thrust T_{cmd} and the maximum available thrust T_{max}

$$t_{rcs} = \frac{1}{f_{rcs}} \frac{T_{cmd}}{T_{max}}.$$

(2.29)
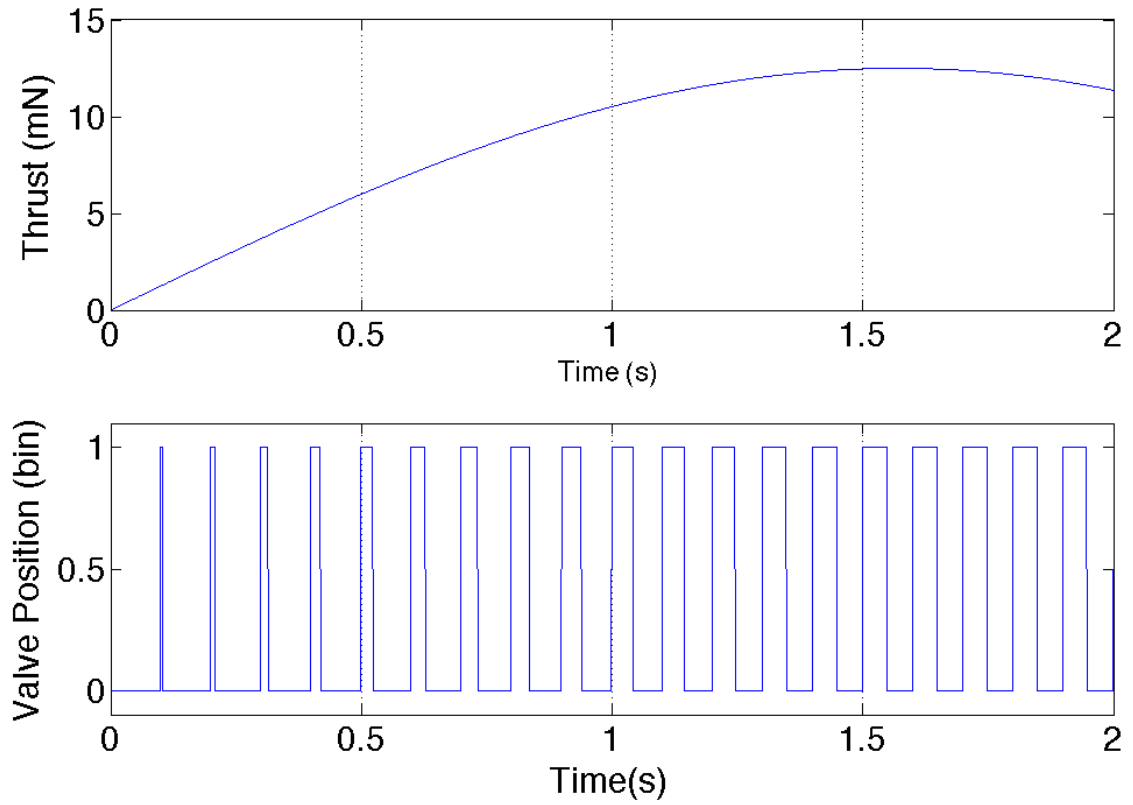
Figure 2.12. Thrust command (top) and resulting valve operation signal (bottom).

Figure 2.12 illustrates the variation of Equation (2.29) with respect to the command signal magnitude when the valves are operated at 10 Hz. The resulting thrust $(\boldsymbol{T}_{rcs})$ from the RCS model must then be considered a function of time as follows

$$\boldsymbol{T}_{rcs}(t') = \begin{cases} 0 & t' > t_{rcs} \\ \\ T_{max} & t' \leq t_{rcs} \end{cases}, \tag{2.30}$$

where t' is an arbitrary periodic time variable with range $[0, 1/f_{rcs}]$. The resulting torque applied to the body is then

$$\boldsymbol{M}_{rcs}(t) = 2l_{rcs}\boldsymbol{T}_{rcs}(t'). \tag{2.31}$$

where the moment arm l_{rcs} is set to be $5\,\mathrm{cm}$ for all thrusters.

A separate model is implemented to account for manufacturer imperfections and installation misalignment, which affects the resulting thrust and torque produced by the thrusters. Small deviations (within the bounds of $\pm 1\%$) from the ideal conditions, $\boldsymbol{\delta}$, are applied to each thruster's maximum thrust, nozzle placement, and angular offset. Additionally, the model accounts for the thrust component normal to the surface of the satellite, $\boldsymbol{T}_{side}$, which depends on the center of pressure $(\boldsymbol{C}_p)$ of the nozzle's exhaust plume. The location of $\boldsymbol{C}_p$ is also subject to a random offset. The altered control moment acting on the body is a function of all the different deviations

$$\boldsymbol{M}'_{rcs} = 2\mathrm{diag}(\boldsymbol{l}_{rcs} + \boldsymbol{\delta}_l)\left[\boldsymbol{C}(\boldsymbol{\delta}_\phi)(\boldsymbol{T}_{rcs}(t') + \boldsymbol{\delta}_T) + \mathrm{diag}(\boldsymbol{T}_{side})(\boldsymbol{C}_p + \boldsymbol{\delta}_{cp})\right]. \tag{2.32}$$

Where $\boldsymbol{C}(\boldsymbol{\delta}_\phi)$ is the direction cosine matrix of the thrust offset angle ϕ. Additional model parameters and other physiscal quantities are detailed in Table 2.6.

Table 2.6. RCS thruster model parameters and propulsion system constants.

Parameter	Symbol	Value	Units
Maximum Thrust	T_{max}	25×10^{-3}	N
Specific impulse	I_{sp}	60	s
Minimum pulse width	t_{min}	2×10^{-3}	s
Operating frequency	f_{rcs}	10	Hz
Thruster moment arm	l_{rcs}	5×10^{-2}	m
Side thrust	T_{side}	$0.01(T_{max})$	N
Center of pressure	C_p	3×10^{-2}	m
Nozzle location offset	$\boldsymbol{\delta}_l$	$\mathrm{rand}(0.01(l_{rcs}))$	m
Nozzle direction offset	$\boldsymbol{\delta}_\phi$	$\mathrm{rand}(1.75)$	rad
Center of pressure offset	$\boldsymbol{\delta}_{cp}$	$\mathrm{rand}(0.01(C_p))$	m
Thrust magnitude offset	$\boldsymbol{\delta}_T$	$\mathrm{rand}(0.01(T_{max}))$	N

2.6.3 Trade Study

The comparison between actuators focuses on the three areas of greatest impact to the mission: accuracy, propellant consumption, and electrical energy required. A $250\,\mathrm{m}$ relative orbit about the RSO at a $500\,\mathrm{km}$ altitude is simulated for each type of actuator. The satellite completes a full orbit while performing target tracking. Both executions utilize the same solver (ode14x), simulation time step ($1\,\mathrm{ms}$), and include all aforementioned disturbances. The operating frequency of the RCS thrusters is set to $10\,\mathrm{Hz}$.

Pointing Accuracy

Figures 2.13 and 2.14 show the pointing accuracy achieved with each actuator during the simulation. While both systems meet the target requirements, the thruster controlled system is shown to be an improvement of approximately one order of magnitude over the RW actuated system.
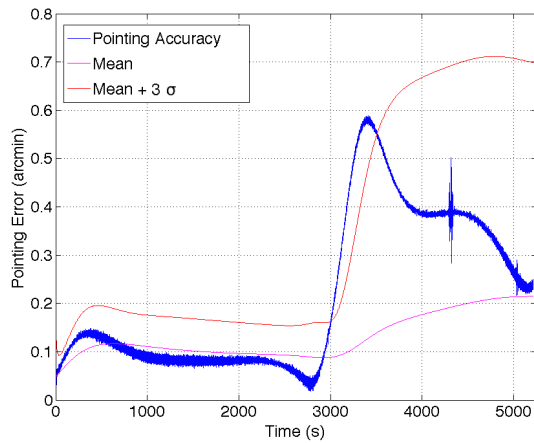
Figure 2.13. Pointing accuracy of RW system during target tracking and disturbance rejection.
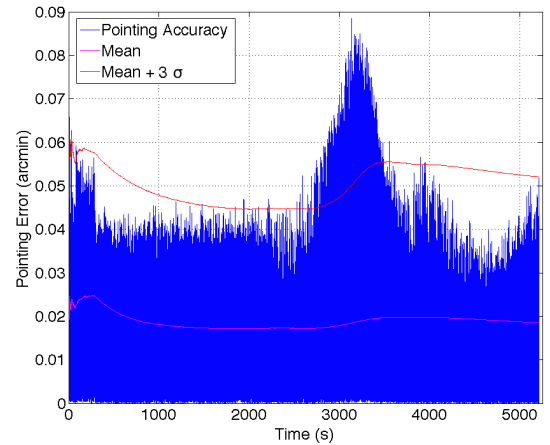
Figure 2.14. Pointing accuracy of RCS thruster system during target tracking and disturbance rejection.

Propellant Consumption

The propellant consumption of the RCS system is determined assuming the mass flow rate per pulse is constant (no loss of pressure). The consumption rate is approximately constant for the simulated maneuver since the tracking motion dominates the pointing performance. This results in a total usage of 7.58×10^{-4} kg for a single orbit period.

The propellant consumption of the RWs is based on the burn time required to offload the stored momentum h

$$t_{burn} = \frac{h}{2T_{max}l_{rcs}}.$$ (2.33)

The amount of propellant required is then

$$m_{p,rw} = \dot{m}_{prop}t_{burn},$$ (2.34)

where the mass flow rate is defined as

$$\dot{m}_{prop} = \frac{T_{max}}{I_{sp}g_E},$$ (2.35)

where I_{sp} is the specific impulse of the propellant and g_e is the acceleration due to gravity at sea level.

Figure 2.15 shows the angular momentum stored in each RW throughout the simulated maneuver. The RWs reach approximately 15.85%, 8.54% and 19.22% of their saturation value respectively. A total of 6.34×10^{-4} kg of propellant is required to offload the combined momentum for a single orbit.

Energy Consumption

Since the base model of the RWs is that of a DC motor, its energy consumption is simply the product of the voltage supplied by the controller and the current drawn by
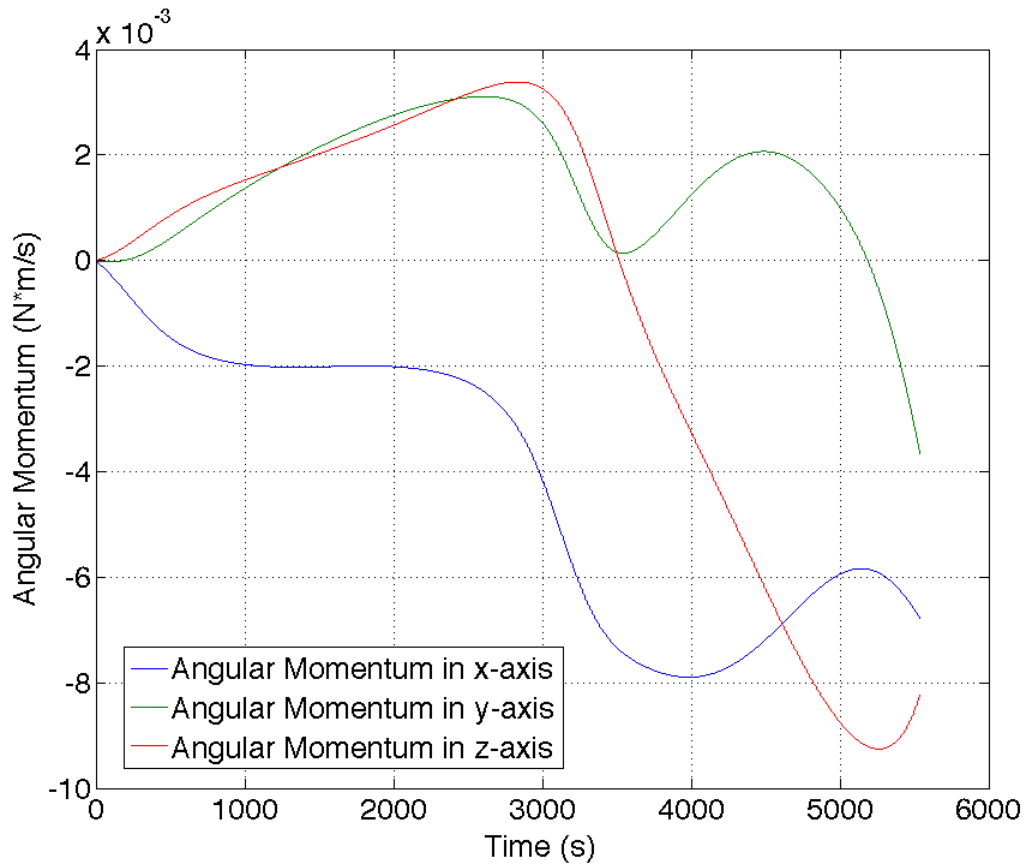
Figure 2.15. Angular momentum stored per axis in RWs in a single orbit during target tracking and disturbance rejection.

the motor integrated over time. Figure 2.16 shows the energy required to operate the RWs over a single orbit period. The sum of the energy consumed per axis results in a 1.019×10^3 J total. Similar analysis on the RCS pulse signal reveals 2.392×10^3 J of energy is required for operation.

Table 2.7. RCS thruster and RW trade study results.

Parameter	RCS	RW	Units
Accuracy (3σ)	0.07	0.7	arcmin
Propellant	7.58×10^{-4}	6.34×10^{-4}	kg
Energy	2.392×10^3	1.019×10^3	J
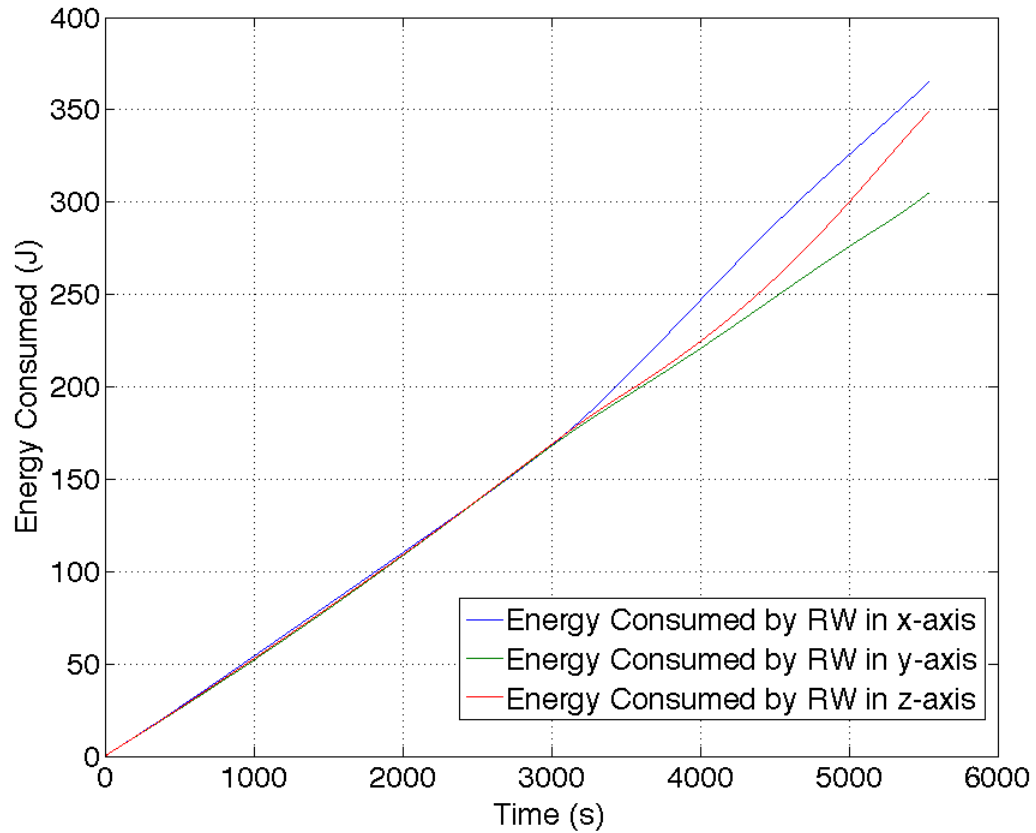
Figure 2.16. Reaction wheel energy consumption per axis in a single orbit during target tracking and disturbance rejection.

The overall performance, restated in Table 2.7, suggests the RCS thruster system is more costly to operate despite its superior accuracy. However, the RW system relies on the thrusters because it requires regular offloading. This represents an inherent power cost proportional to t_{burn} and increased operational complexity due to the accompanying attitude correction maneuver. Additionally, the operational cost of the thrusters can be reduced by adjusting the operating frequency f_{rcs}.

Based on this analysis, the RWs are considered to be unnecessary in the present system and may be excluded. In addition to reducing the mass and volume required

by the ADCS, removal of the RWs circumvents the need for angular momentum management maneuvers. Moreover, the RCS thruster configuration is sufficient to preserve attitude control redundancy. All further results utilize the thruster actuation model exclusively.

2.7 Sensors

The ADCS primary attitude determination method consists of utilizing the STR quaternion solutions and angular rate measurements to feedback the attitude states required by the control law. In order to account for measurement uncertainty, simple models based on manufacturer specifications are used to introduce noise directly into the feedback signal.

2.7.1 Star Tracker

The STR model is based on the Nano Star Tracker developed by Blue Canyon Technologies. This presents an advantage because the STR delivers attitude information directly in quaternion format. Therefore, all present uncertainties are attributed to white noise and are assumed to be independent of internal process error.

The star tracker output is represented as a combination of the true quaternion solution and the quaternion representation of its roll and bore-sight uncertainties as indicated in Table 2.8

$$\bar{\boldsymbol{q}}_{str} = \bar{\boldsymbol{q}} \otimes (\bar{\boldsymbol{q}}_{str,bs} \otimes \bar{\boldsymbol{q}}_{str,r}). \tag{2.36}$$

Within the model, $\bar{\boldsymbol{q}}_{str,bs}$ and $\bar{\boldsymbol{q}}_{str,r}$ are calculated by defining random offset angles ϕ_{bs} and ϕ_r that follow the accuracy distributions $\sigma_{str,bs}$ and $\sigma_{str,r}$ respectively. Consider two arbitrary unit vectors $\hat{\boldsymbol{e}}_{bs}$ and $\hat{\boldsymbol{e}}_r$ as defined in Equation (2.3), where $\hat{\boldsymbol{e}}_{bs}$ is perpendicular and $\hat{\boldsymbol{e}}_r$ is parallel to the body x-direction. Then

$$\bar{\boldsymbol{q}}_{str,bs} = \begin{bmatrix} \cos(\phi_{bs}/2) \\ \sin(\phi_{bs}/2)\hat{\boldsymbol{e}}_{bs} \end{bmatrix} \tag{2.37}$$

and

$$\bar{\boldsymbol{q}}_{str,r} = \begin{bmatrix} \cos(\phi_r/2) \\ \sin(\phi_r/2)\hat{\boldsymbol{e}}_r \end{bmatrix} \tag{2.38}$$

Note that $\hat{\boldsymbol{e}}_{bs}$, ϕ_r, and ϕ_{bs} are not fixed values; instead they are randomly generated at every simulation step.

Table 2.8. STR hardware parameters based on the Blue Canyon Technology Nano Star Tracker.

Parameter	Symbol	Value	Units
Update rate	f_{str}	5	Hz
Bore-sight accuracy	$\sigma_{str,bs}$	6 (1σ)	arcsec
Roll axis accuracy	$\sigma_{str,r}$	40 (1σ)	arcsec
Nominal operation range	-	< 1	$^\circ\,\mathrm{s}^{-1}$
Off-nominal operation range	-	< 4	$^\circ\,\mathrm{s}^{-1}$

2.7.2 Angular Rate Gyro

The angular rate gyro model is based on the Nano Inertial Measurement Unit (IMU) developed by MEMSENSE. The model assumes the rate gyro triad can be

analyzed as three separate sensors each collecting information about a single body direction. Furthermore, measurements are assumed to be affected by bias b_g, scaling S_g and white noise w_{arw}.

A simple gyro model for this set of assumptions is given by (Flenniken, 2005)

$$\omega_g = (1 + S_g)\omega + b_g + w_{arw}. \tag{2.39}$$

Note that there is no way of determining the scaling and bias values other than through empirical data of the specific hardware in question. Therefore, random constant values are assigned at the beginning of each simulation based on the deviations specified in Table 2.9.

Table 2.9. IMU hardware paramaeters based on the MEMSENSE Nano IMU series.

Parameter	Symbol	Value	Units
Update rate	f_{gyro}	50	Hz
Angle random walk	w_{arw}	$1.66 \times 10^{-2}\,(1\sigma)$	$\mathrm{rad\,s^{-1}}$
Bias random walk	w_{brw}	$2.62 \times 10^{-2}\,(1\sigma)$	$\mathrm{rad\,s^{-2}}$
Scaling Random walk	w_{srw}	$0.10\,(1\sigma)$	$\mathrm{s^{-1}}$

3. Filtering and Estimation

The sampling rate and accuracy of the system sensors have a direct impact on the ADCS performance. After implementing the sensor models discussed in Section 2.7, two different methods of state estimation are proposed: an extended Kalman filter (EKF), and a gyro-less rate observer.

3.1 Extended Kalman Filter

Some of the control laws presented in Chapter 4 require simultaneous quaternion and angular rate error measurements. However, the maximum sampling rate of the gyro is $50\,\mathrm{Hz}$ whereas the STR's is $5\,\mathrm{Hz}$. Therefore the main purpose of the EKF in our system is to propagate the quaternion solution of the STR between measurements using the quaternion kinematics discussed in Section 2.2.

Consider the attitude kinematics presented in Equation (2.6)

$$\dot{\boldsymbol{q}} = \frac{1}{2}\begin{bmatrix} 0 & -\omega_x & -\omega_y & -\omega_z \\ \omega_x & 0 & \omega_z & -\omega_y \\ \omega_y & -\omega_z & 0 & \omega_x \\ \omega_z & \omega_y & -\omega_x & 0 \end{bmatrix}\begin{bmatrix} q_0 \\ q_1 \\ q_2 \\ q_3 \end{bmatrix},$$

where ω_n represents the true angular rate measured by the rate gyro about any of the BFF axes. Then, solving Equation (2.39) for ω_n

$$\omega_n = \frac{1}{1 + S_{g,n}} (\omega_{g,n} - b_{g,n} - w_{arw}). \tag{3.1}$$

Note that although b_n and S_n cannot be measured, they can be included in the estimation process by

$$\boldsymbol{\dot{b}_g} = \begin{bmatrix} \dot{b}_{g,x} \\ \dot{b}_{g,x} \\ \dot{b}_{g,x} \end{bmatrix} = \begin{bmatrix} w_{rrw} & 0 & 0 \\ 0 & w_{rrw} & 0 \\ 0 & 0 & w_{rrw} \end{bmatrix}, \tag{3.2}$$

$$\boldsymbol{\dot{S}_g} = \begin{bmatrix} \dot{S}_{g,x} \\ \dot{S}_{g,y} \\ \dot{S}_{g,z} \end{bmatrix} = \begin{bmatrix} w_{srw} & 0 & 0 \\ 0 & w_{srw} & 0 \\ 0 & 0 & w_{srw} \end{bmatrix}. \tag{3.3}$$

Where w_{rrw} and w_{srw} are random constants based on the hardware properties specified Table 2.9.

Together, Equations (2.6) and (3.1) to (3.3) form the state $\boldsymbol{x}$ to be estimated by the EKF

$$\boldsymbol{x} = [q_0, q_1, q_2, q_3, b_{g,x}, b_{g,y}, b_{g,z}, S_{g,x}, S_{g,y}, S_{g,y}]^T. \tag{3.4}$$

Appendix B shows the linearizion and discretization process in detail. The procedure for the discrete EKF implementation is summarized here.

The estimation process uses a predictor-corrector approach, which assumes a general, non-additive noise model (G. Blesser, n.d.). The predicted state $\boldsymbol{\mu}^p$ and state covariance $\boldsymbol{P}^p$ are calculated according to

$$\boldsymbol{\mu}_t^p = g(\boldsymbol{u}_t, \boldsymbol{\mu}_{t-1}), \tag{3.5}$$

$$\boldsymbol{P}_t^p = \boldsymbol{G}_t \boldsymbol{P}_{t-1} \boldsymbol{G}_t^T + \boldsymbol{W}_t \boldsymbol{R}_t \boldsymbol{W}_t^T. \tag{3.6}$$

Where $\boldsymbol{G}_t$ is the state transition matrix, $\boldsymbol{R}_t$ is the process noise covariance matrix, and $\boldsymbol{W}_t$ is the "noise transition" matrix, required by the non-additive noise calculations.

The corrected or updated states are calculated using the Kalman gain $\boldsymbol{K}_t$

$$\boldsymbol{K}_t = \boldsymbol{P}_{t-1}^p \boldsymbol{H}_t^T (\boldsymbol{H}_t \boldsymbol{P}_{t-1}^p \boldsymbol{H}_t^T + \boldsymbol{V}_t \boldsymbol{Q}_t \boldsymbol{V}_t^T)^{-1}, \tag{3.7}$$

$$\boldsymbol{\mu}_t = \boldsymbol{\mu}_t^p + \boldsymbol{K}_t \left[\boldsymbol{z}_t - \boldsymbol{H}_t \boldsymbol{\mu}_t^p \right], \tag{3.8}$$

$$\boldsymbol{P}_t = (\boldsymbol{I} - \boldsymbol{K}_t \boldsymbol{H}_t) \boldsymbol{P}_t^p. \tag{3.9}$$

Where $\boldsymbol{H}_t$ is the measurement correction matrix, $\boldsymbol{Q}_t$ is the measurement noise co-variance matrix, and $\boldsymbol{V}_t$ is the "measurement walk" matrix corresponding to the non-additive noise model. $\boldsymbol{z}_t$ is the measurement update from the STR.

The EKF performance is measured by calculating the quaternion error as defined in Equation (2.8), taking $\bar{\boldsymbol{q}}_{cmd}$ to be the true attitude solution given by the plant and

$\bar{q}$ as the EKF output. Figure 3.1 shows how the quaternion error converges over time.
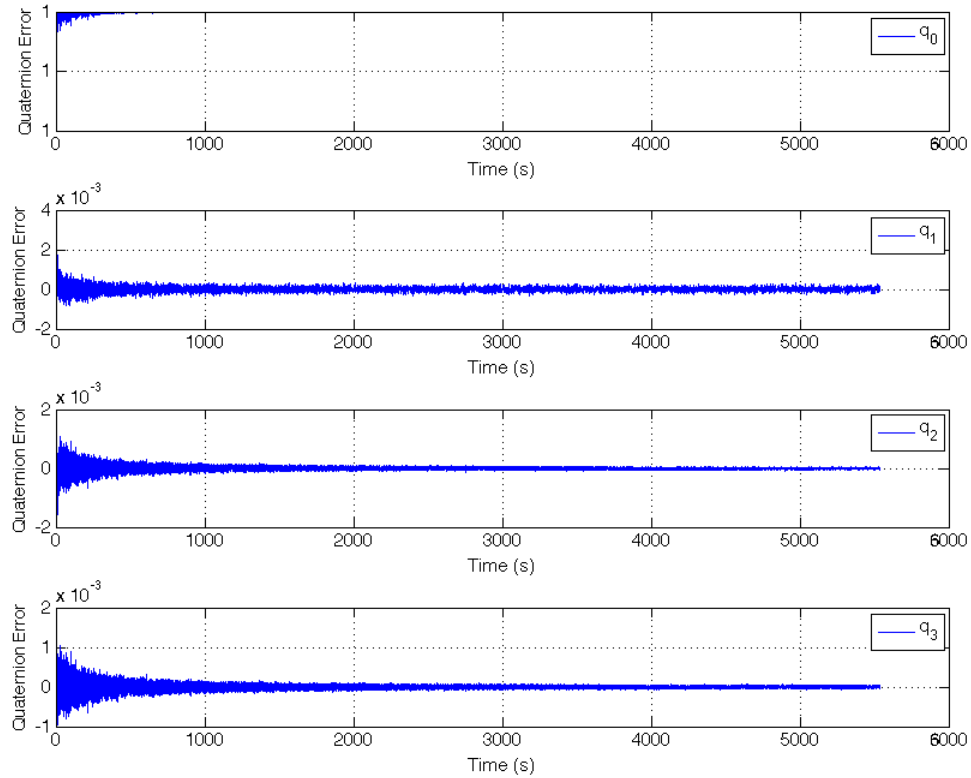
Figure 3.1. Quaternion Error between the true plant output and the EKF output with an STR update rate of 5 Hz and a gyro sampling rate of 50 Hz.

Note that the EKF only estimates the quaternion feedback; it is not designed to filter the white noise from the gyro measurements. Additionally, the EKF quaternion input corresponds to the simulated STR quaternion as defined by Equation (2.36).

3.2 Angular Rate Observer

An alternative solution to the EKF is presented by (Thakur, Mazenc, & Akella, 2014) in the form of a smooth angular velocity observer. This solution estimates the body angular rate based solely on the STR quaternion solution and does not require gyro measurements or corrections. The estimation law is proven to be stable through partial Lyapunov strictification and is defined using quaternion observer kinematics

$$\dot{\hat{\bar{q}}} = \frac{1}{2} \boldsymbol{E}(\hat{\bar{q}})(\hat{\boldsymbol{\omega}} + \lambda \boldsymbol{C}^T(\tilde{\bar{q}})\tilde{\boldsymbol{q}}_v), \tag{3.10}$$

$$\dot{\hat{\boldsymbol{\omega}}} = \boldsymbol{C}^T(\tilde{\bar{q}})\boldsymbol{J}^{-1}\left[\gamma \tilde{\boldsymbol{q}}_v - \boldsymbol{S}(\hat{\boldsymbol{\omega}}^B)\boldsymbol{J}\hat{\boldsymbol{\omega}}^B + \boldsymbol{M}_{cmd} - \lambda \boldsymbol{J}\boldsymbol{S}(\tilde{\boldsymbol{q}}_v)(\hat{\boldsymbol{\omega}}^B) \right]. \tag{3.11}$$

Where λ and γ are tuning parameters and

$$\hat{\boldsymbol{\omega}}^B \equiv \boldsymbol{C}(\tilde{\bar{q}})\hat{\boldsymbol{\omega}}. \tag{3.12}$$

In this notation, $\hat{\bar{q}}$ and $\hat{\boldsymbol{\omega}}$ represent the estimated quaternion and angular rates respectively. Their counterparts $\tilde{\bar{q}}$ and $\tilde{\boldsymbol{\omega}}$ represent the corresponding estimation errors. In turn, $\boldsymbol{C}$ and $\boldsymbol{S}$ represent the cosine matrix and skew symmetric matrix of their respective arguments. $\boldsymbol{E}$ represents a collapsed quaternion matrix analogous to Equation (2.7) defined as:

$$E(\bar{\boldsymbol{q}}) = \begin{bmatrix} -\boldsymbol{q}_v^T \\ q_0\boldsymbol{I} + \boldsymbol{S}(\boldsymbol{q}_v) \end{bmatrix} \tag{3.13}$$

Although limited by the operational conditions of the STR, this approach has the advantage of estimating both quaternion and angular rate values without the need for additional hardware. To account for the STR sampling time, a zero order hold is placed on the continuous signal and is linearly extrapolated between measurement updates.
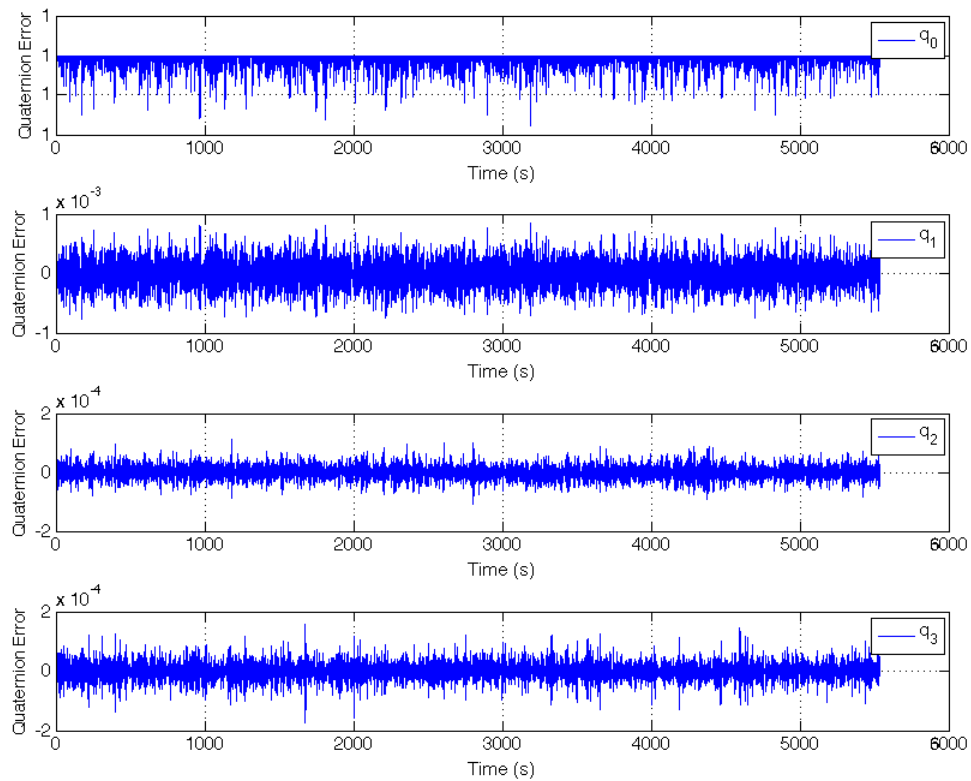
Figure 3.2. Quaternion Error between the true plant output and the angular rate observer.

Figure 3.2 shows the error of the quaternion estimation. Notice that the error magnitude remains constant with a zero mean instead of converging towards its steady

state value like the EKF. As with the EKF, the inputs to the observer correspond to the simulated sensor signals.

The estimated angular rates cannot be compared directly to the measured rates because the sensor model output is never used as an input to the observer. Instead, Figures 3.3 to 3.6 showcase the observer performance by comparing the estimate (at an STR sampling rate of 1 Hz) directly to the true values. The unused sensor signal is included to present a qualitative comparison between the true, measured, and estimated values.
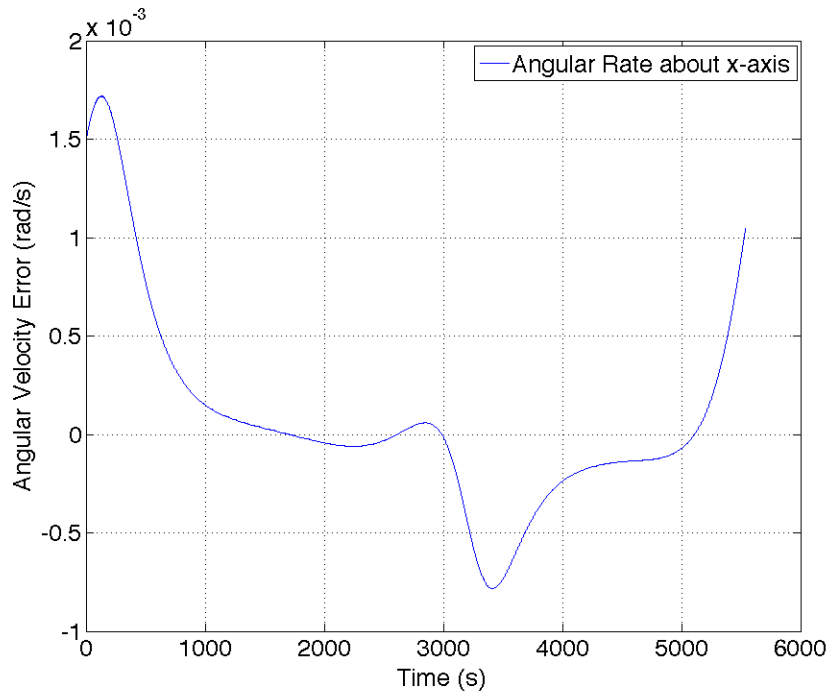
Figure 3.3. True angular rate about the BFF x-axis during target tracking.

Figure 3.4 shows the expected sensor output lies in the $1 \times 10^{-1} \, \mathrm{rad\,s^{-1}}$ range whereas Figure 3.3 shows the true value is in the $1 \times 10^{-3} \, \mathrm{rad\,s^{-1}}$ range. The estimated

rate error (Figure 3.6) is of the same order of magnitude as the true data but the estimated rates are seen to follow the same general progression of the true rates. This performance is shown in Chapter 5 to provide sufficient accuracy to achieve the pointing requirements.
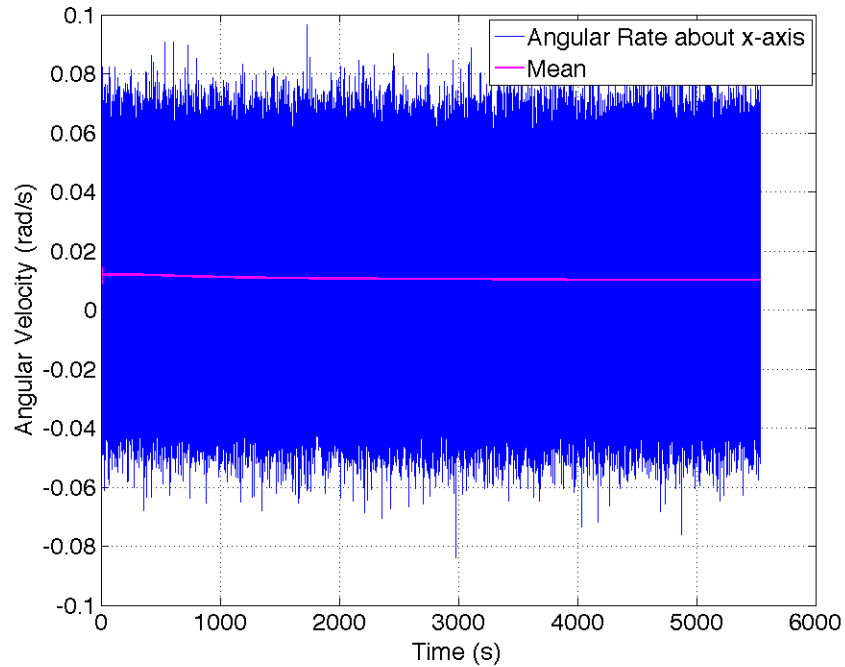
Figure 3.4. True angular rate about the BFF x-axis with gyro sensor model noise.
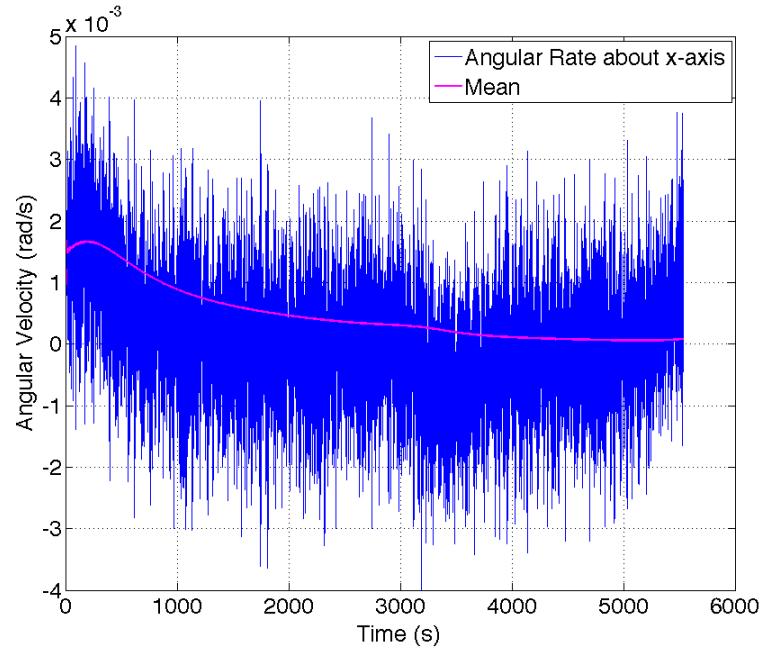
Figure 3.5. Estimated angular rate about the BFF x-axis during target tracking.(The STR sampling rate was set to 1 Hz)
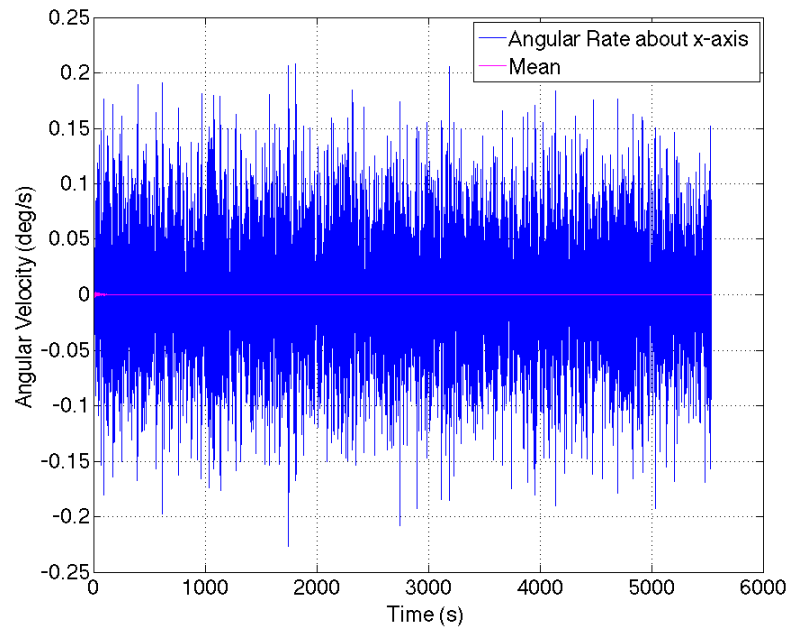
Figure 3.6. Error between true and estimated angular rate in the BFF x-axis.(The STR sampling rate was set to 1 Hz)

4. Controller Design

The ARAPAIMA mission has stringent attitude requirements that vary as the operational modes progress. Aside from orbital maneuvers, the mission requires the ADCS be able to perform detumbling, slew, target tracking, and frame centering maneuvers. Individual maneuvers and the transitions between them must also preserve stability requirements. The different control configurations presented in this section focus on addressing each mission maneuver. They also follow the chronological evolution of the ADCS design and the rationale behind same.

4.1   Eigenaxis Control

The slew and target tracking control mode is based on the quaternion feedback regulator proposed by (Wie, 1985). It consists of linear error quaternion feedback and both linear and nonlinear angular rate feedback which counteract gyroscopic coupling torques. This approach is based on eigenaxis rotations and is analogous to the well known PD controller. It is designed for large angle maneuvers and both its global stability as well as its robustness to inertia matrix uncertainty are proven in relation to various spacecraft applications (Wie & Lu, 1995). One minor modification suggested

by (Pong et al., 2010) changes the angular rate feedback term $\boldsymbol{\omega}$ to angular rate error

feedback $\boldsymbol{\omega}_e$ defined simply as

$$\boldsymbol{\omega}_e = \boldsymbol{\omega} - \boldsymbol{\omega}_{ref}, \tag{4.1}$$

where $\boldsymbol{\omega}_{ref}$ is the reference angular velocity.

The regulator control output is the expressed as a command torque

$$\boldsymbol{M}_{cmd} = -\boldsymbol{\omega} \times \boldsymbol{J}\boldsymbol{\omega} - \boldsymbol{K}_d\boldsymbol{\omega}_e - \boldsymbol{K}_p\boldsymbol{q}_{e_v}, \tag{4.2}$$

where $\boldsymbol{K}_d$ and $\boldsymbol{K}_p$ are gain matrices of the form $\boldsymbol{K} = a\boldsymbol{J}$. According to (Wie, Weiss,

& Arapostathis, 1989), the gyroscopic decoupling feedback $\boldsymbol{\omega} \times \boldsymbol{J}\boldsymbol{\omega}$ is unnecessary for

slow tracking maneuvers. In such cases, Equation (4.2) reduces to the linear control

law

$$\boldsymbol{M}_{cmd} = -\boldsymbol{K}_d\boldsymbol{\omega}_e - \boldsymbol{K}_p\boldsymbol{q}_{e_v}. \tag{4.3}$$

4.2 PID Control

Some operations such as detumbling, frame centering, and inertial pointing require

terms to approach a zero steady-state error. The eigenaxis control law lacks integral

terms, resulting in unavoidable error offset or bias. Integral control action is introduced

into the system by switching to a PID-type controller implemented about each axis.

A PID control law that utilizes the vector portion of the same input error quaternion parameter as Equation (4.3) is defined as

$$\boldsymbol{M}_{cmd} = -\left[\boldsymbol{K}_p + \frac{\boldsymbol{K}_i}{s} + \boldsymbol{K}_d s\right]\boldsymbol{q}_{e_v},\qquad(4.4)$$

where $\boldsymbol{K}_i$ is also a gain matrix of the form $\boldsymbol{K} = a\boldsymbol{J}$.

This control law has a marked advantage over the eigenaxis law in that it does not have angular rate inputs, which means it is only affected by the STR white noise. It must be noted, however, that this approach depends on the pointing error being small at the moment of switch so the dynamics are decoupled. Otherwise, integral control could drive the system unstable.

4.2.1 Gain Scheduling

Using the star tracker quaternion attitude solution, it is possible to apply Equation (4.4) to different types of maneuvers by choosing appropriate gains for each. Instead of creating a new control law for each application, gain scheduling is utilized to apply the same law to different control modes. The scheduling scheme is described as a function of time by

$$\begin{aligned} p &= p_1 + f(t)(p_2 - p_1) \\ i &= i_1 + f(t)(i_2 - i_1) \\ d &= d_1 + f(t)(d_2 - d_1) \end{aligned}\qquad(4.5)$$

where p, i, and d are the scalar terms of the gain matrices in Equation (4.4). $f(t)$ is a type of smoothstep function (ramp function with smooth edges) with an arbitrary slope m that controls the duration of the control switch transition shown in Figure 4.1. By setting the integral term i_1 to zero at the moment of switch, it is possible to transition smoothly between control modes as this reduces the 'bump' effect of switching between controllers with different integral terms. The switch performance can be further improved by resetting the PID integrator and gain transition simultaneously.
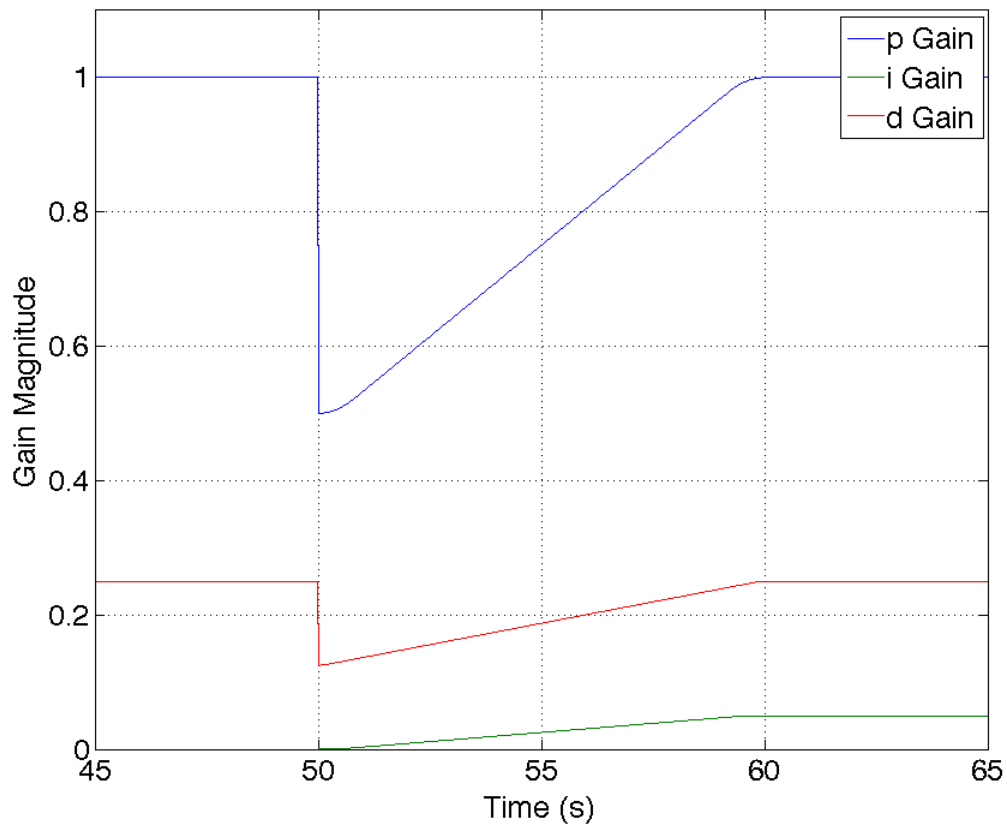
Figure 4.1. Smoothstep scheduling functions ensure a continuous gain transition.

4.2.2 Detumbling

Detumbling operations require the body angular rates be reduced past a specified threshold within a set of given constraints, usually determined by the time or energy limitations of the system. A simple PI law results from applying Equations (4.4) and (4.5) with $d_2 = 0$, which is used to bring the angular rates to zero

$$\boldsymbol{M}_{cmd} = -\left[\boldsymbol{K}_p + \frac{\boldsymbol{K}_i}{s}\right]\boldsymbol{\omega}_e. \tag{4.6}$$

4.2.3 Image Feedback

Imaging operations require high accuracy and are sensitive to measurement noise and bias in the controller input. Visual feedback utilizes the payload cameras at high sampling rates to generate a secondary set of command inputs based on the position of the RSO in the payload's field of view (FOV). Assuming there is no significant optical noise, this provides unbiased information which can be used to perform frame centering maneuvers.

Figure 4.2 illustrates how the pointing error angle ψ_e can be described as a function of the distance between the satellite and the RSO, and the Δx and Δy projection parameters. Instead of the quaternion error seen thus far, the projection parameters are used to direct the necessary Y-axis and Z-axis rotation commands

$$\boldsymbol{M}_{cmd} = -\left[\boldsymbol{K}_p + \frac{\boldsymbol{K}_i}{s} + \boldsymbol{K}_d s\right]\begin{bmatrix} -\Delta x \\ \Delta y \end{bmatrix}. \tag{4.7}$$
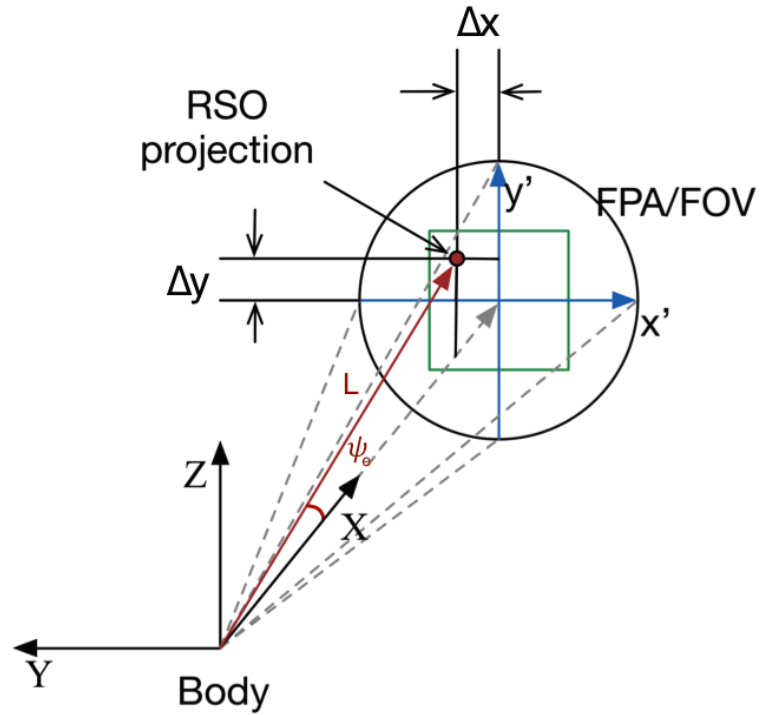
Figure 4.2. Projection of the RSO on the camera FOV superimposed on a 2D Cartesian coordinate system used for frame centering.

In practice, it is not possible to obtain 3D attitude information from a 2D projection without multiple reference points obtained from the star field in the background or by feature detection of the RSO. For the ARAPAIMA mission, it is assumed that a constant angular rate is induced about the BFF x-axis prior to the frame centering maneuver such that the solar panels are kept in sunlight (but not enough to interfere with imaging operations). Therefore, no control torques are exerted about the body x-direction throughout the maneuver.

The simulation model is not yet advanced enough to accept a stream of pictures to determine Δx and Δy. Therefore, the projection parameters are obtained from the

true (noiseless) quaternion error and the distance L_{rso} between the satellite and the

RSO as

$$\Delta x = -L_{rso} \left[\frac{\bar{q}_e \hat{\bar{x}} \bar{q}_e^{-1}}{\| \bar{q}_e \hat{\bar{x}} \bar{q}_e^{-1} \|} \right]_2,$$

$$\Delta y = L_{rso} \left[\frac{\bar{q}_e \hat{\bar{x}} \bar{q}_e^{-1}}{\| \bar{q}_e \hat{\bar{x}} \bar{q}_e^{-1} \|} \right]_3.$$

(4.8)

Where $\hat{x}$ is the BFF x-axis unit vector and $\bar{q}_e \hat{\bar{x}} \bar{q}_e^{-1}$ is the quaternion rotation of $\hat{x}$

(Kuipers, 1999). Note that only a single element of the normalized vector is considered,

as specified by the subscript outside the square brackets.

4.3   Eigenaxis with Integral Control

With the implementation of the angular rate observer (see Section 5.2.2), the

performance of the eigenaxis and PID control laws is close enough to prompt the

question of whether the complexity added by switching controllers is justifiable. An

alternative solution was proposed by (Wie, Bailey, & Heiberg, 2002), which involves

adding an integral control term to the quaternion error feedback in Equation (4.3)

$$M_{cmd} = -K_d \omega_e - K_p q_{e_v} - K_i \int q_{e,v}.$$

(4.9)

Gain scheduling is applied in the same manner as with the PID controller

$$M_{cmd} = -J \left(d\omega_e - p q_{e_v} - i \int q_{e_v} \right).$$

(4.10)

Where d, p, and i vary according to Equation (4.5). In order to avoid possible

instability introduced by the integral term, i is set to zero during rapid slews and

large angle maneuvers. It is then scheduled to the proper value during frame centering and imaging operations.

4.3.1 Image Feedback

Since the image feedback process described in Section 4.2.3 gives projection parameters as inputs, Equation (4.9) has to be modified in order to work properly. A time derivative term is added to the quaternion error feedback such that

$$\boldsymbol{M}_{cmd} = -\boldsymbol{J}\left(d\boldsymbol{\omega}_e + p\boldsymbol{q}_{e_v} + i\int \boldsymbol{q}_{e_v} + v\frac{d}{dt}\boldsymbol{q}_{e_v}\right). \tag{4.11}$$

or, in the Laplace domain

$$\boldsymbol{M}_{cmd} = -\boldsymbol{J}\left[d\boldsymbol{\omega}_e + \left(p + \frac{i}{s} + vs\right)\boldsymbol{q}_{e_v}\right]. \tag{4.12}$$

Where v is another gain constant that can be scheduled according to Equation (4.5). As with i, v is set to zero during all maneuvers for which it is not required.

4.3.2 Controller Discretization

A necessary step in the ADCS development is the discretization of the control law, estimators, and feedback algorithms. For the moment, it is assumed that the control law and estimator are implemented as part of a larger flight software that will manage communication with the sensors and other hardware. The EKF algorithm was designed from the start as a digital system and as such requires no discretization.

Similarly, the rate observer together with the input extrapolator acts similar to a first order hold (FOH) system which also requires no discretization other than using an appropriate order numerical integrator to solve Equations (3.10) and (3.11).The main concern is then the discretization of the controller.

Equations (4.4) and (4.12) contain all the terms of interest that require discrete representation. Using the forward Euler integration method as given by (Franklin, Powell, & Workman, 1990)

$$y(t) = \int_{t_0}^{t} f(t)dt, \tag{4.13}$$

$$\int_{t=kT_s}^{(k+1)T_s} f(t)dt = y((k+1)T_s) - y(kT_s), \tag{4.14}$$

where k is simply the discrete time step counter, and T_s is the sampling time constant. It is possible to express the Laplace domain integral

$$Y(s) = \frac{1}{s}F(s), \tag{4.15}$$

as a discrete domain or Z domain approximation

$$Y(z) \approx \frac{T_s}{z-1}F(z). \tag{4.16}$$

Therefore, the simple relation

$$\frac{1}{s} \approx T_s \frac{1}{z-1},$$ (4.17)

can be used to discretize the control equations.

The PID controller is given as

$$\boldsymbol{J} \left[p + i \frac{T_s}{z-1} + d \frac{N}{1 + N \frac{T_s}{z-1}} \right] \boldsymbol{q}_{e_v},$$ (4.18)

where the discrete time derivative has been changed to better represent the control algorithm implementation. In the continuous time model, filtered time derivatives are preferred because they can be implemented by using an integrator feedback loop. The same format was followed in the discrete model, which makes Equation (4.17) the only substitution necessary in the discretization. Figure 4.3 gives a block diagram representation of the filtered time derivative. N is simply a filter gain which can be tuned to affect the response of the pole filter in the derivative. A default value of 100 is used throughout the model.
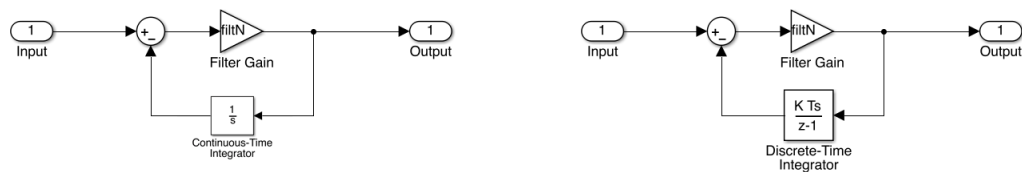
(a) Block diagram of discrete time derivative feedback loop representation in Simulink.

(b) Block diagram of continuous time derivative feedback loop representation in Simulink.

Figure 4.3. Continuous discrete and filtered Time derivative block diagrams

The modified eigenaxis control law defined in Equation (4.12) can now be discretized in the same fashion

$$\boldsymbol{M}_{cmd} = -\boldsymbol{J}\left[d\boldsymbol{\omega}_e + \left(p + i\frac{T_s}{z-1} + v\frac{N}{1 + N\frac{T_s}{z-1}}\right)\boldsymbol{q}_{e_v}\right]. \qquad (4.19)$$

At this point, it is useful to note that the control and estimator algorithms can have different sampling constants T_s. Additionally, sensor sampling rates can be set to arbitrary multiples of T_s. This allows the system performance to be evaluated in multiple scenarios that reflect the availability of resources in the ARAPAIMA on-board computer (OBC).

4.3.3 Transient Stability Analysis

The gain scheduling technique applied throughout this section gives rise to a concern regarding system stability during gain transients. While each control law presented ensures stability (given their respective conditions and assumptions are valid), their individual properties do not guarantee stable transient behavior. This behavior depends solely on how the gain scheduling is executed. In turn, this presents a set of restrictions on the controller tuning.

Stability analysis is carried out by linearizing the plant at predetermined time "snapshots", beginning at the moment of switch. A pole-zero map is then produced at each point to examine the system transient behavior.

The results presented in Chapter 5 correspond to maneuver specific gain values for a 10 s gain transient. The analysis presented here examines a similar case for a PID controller (Equation (4.4)) in a target tracking, disturbance-free, scenario. The initial and final gain values (identical to those in Section 5.2.2) are listed in Table 4.1.

Table 4.1. Gain parameters for transient behavior pole-zero mapping.

Parameter	Symbol	Value
PID proportional gain at switch	p_1	0.35
PID derivative gain at switch	d_1	0
PID integral gain at switch	i_1	0
PID proportional gain post-switch	p_2	0.75
PID derivative gain post-switch	d_2	0.50
PID integral gain post-switch	i_2	0.025

The first 100 s of the simulation are linearized at "snapshots" of (0, 2, 4, 6, 8, 10, 12.5, 15, 20, 25, 30, 40, 50, 75, and 100) s. The resulting pole-zero maps are shown in Figure 4.4. Although the system is stable for the initial and final gain values, adding a non-zero integral gain yields an unstable system for the first 8 s after switching gains. This coincides with the increase in pointing error at the moment of switch seen in Figures 5.5 and 5.7. From the controller performance results, it seems evident this brief instability period does not affect the overall target tracking performance. However, any disturbance irregularity occurring during this period could potentially cause severe system instability.
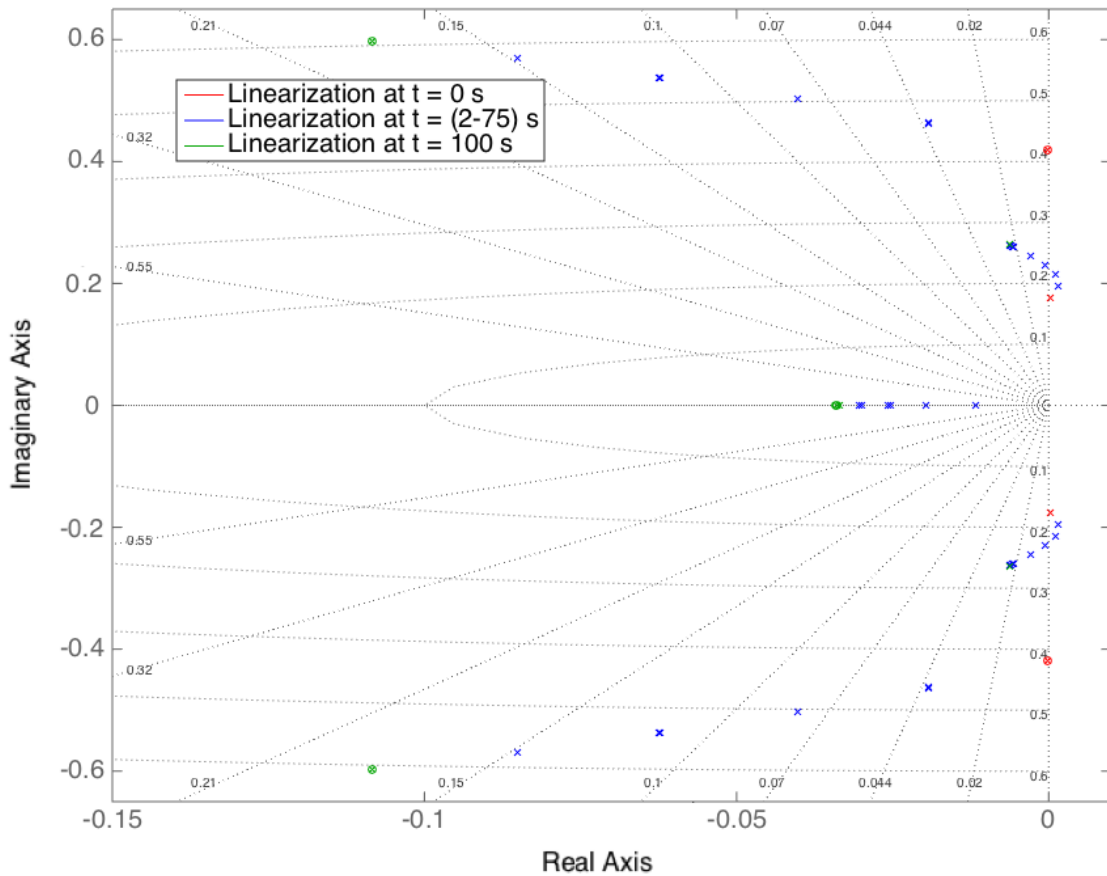
Figure 4.4. Pole-zero map for unstable gain transient.

The issue is readily solved by modifying the initial gain values such that $d_1 \neq 0$, and increasing the gain scheduling transient duration so the integral gain occurs more gradually that the rest. A set of gain values which yield a stable transient system is shown in Table 4.2. Note that the gain transient period is $10\,\mathrm{s}$ for the proportional and derivative gains, and $20\,\mathrm{s}$ for the integral gain. The resulting pole-zero maps for the same "snapshots" discussed above are shown in Figure 4.5.

Table 4.2. Modified gain parameters for stable transient behavior pole-zero mapping.

Parameter	Symbol	Value
PID proportional gain at switch	p_1	0.50
PID derivative gain at switch	d_1	0.25
PID integral gain at switch	i_1	0
PID proportional gain post-switch	p_2	1.0
PID derivative gain post-switch	d_2	0.75
PID integral gain post-switch	i_2	0.050
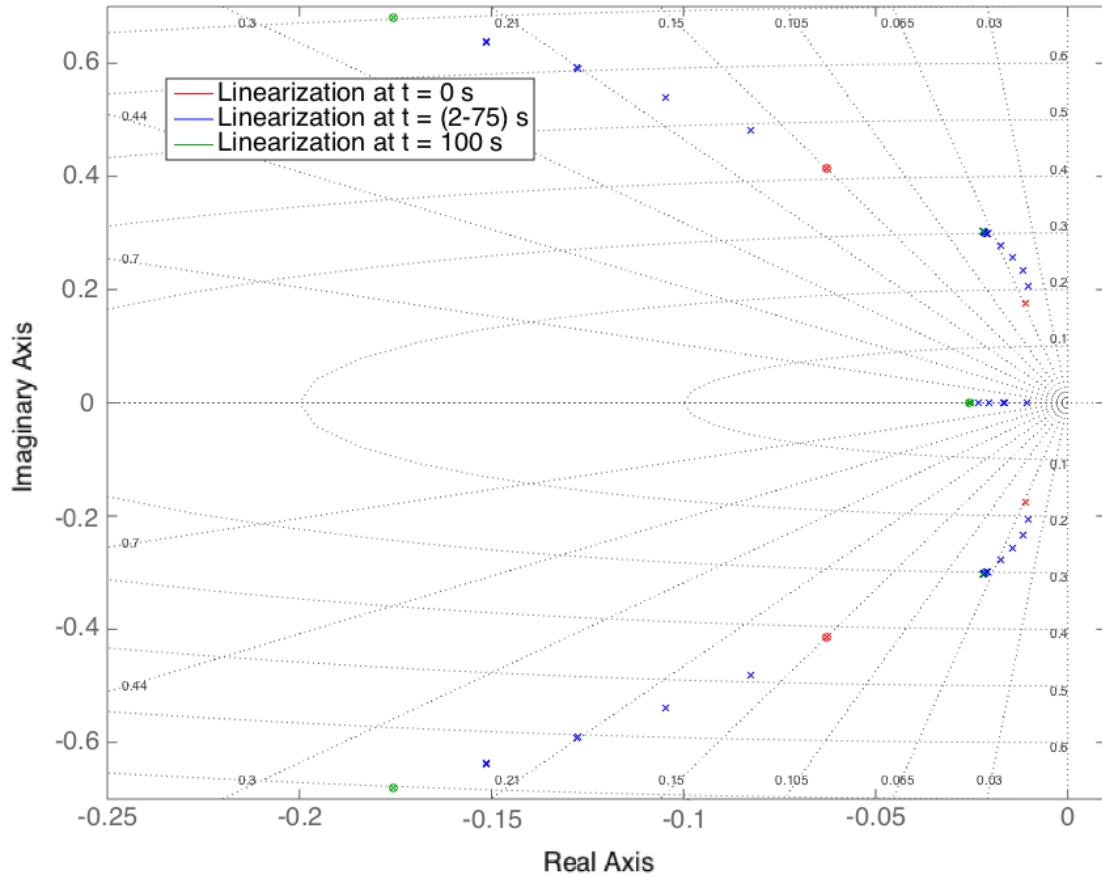
Figure 4.5. Pole-zero map for stable gain transient.

5. Numerical Simulations & Results

The numerical simulation outline follows the format of a simplified closed-loop control system. As such, its components are divided into three main subsystems: the plant, the controller, and the filter. The plant incorporates all internal and external disturbances described in Chapter 2. These are produced by environmental models within an orbital mechanics simulation in which the ARAPAIMA satellite has established a $250\,\mathrm{m}$ relative orbit about the target RSO. This orbit lies at an altitude of $500\,\mathrm{km}$ from the Earth's surface, at a $28.5°$ inclination.

The controller applies the different control configurations discussed in Chapter 4, and provides the necessary torque commands to track the RSO with an accuracy of $1\,\mathrm{arcmin}$ at $3\,\sigma$. The true pointing error of the satellite, its running mean, and deviation, are calculated parallel to control laws; these serve as the primary measure of the system performance. Lastly, the filter, placed downstream and in series with the sensor noise models, estimates the plant state by implementing the procedures outlined in Chapter 3. The different subsystems can be assigned their respective operating frequencies to give a better approximation of the system performance under different environmental or computational constraints.

5.1 Simulation Parameters

Most of the results presented in this chapter show the tracking performance of the satellite for a set of attitude quaternion and angular velocity profiles which correspond to a relative orbit about the target RSO. These reference signals (Figures 5.1 and 5.2) and their respective initial conditions were obtained from an ARAPAIMA mission STK simulation. Initial conditions and other global simulation parameters are given in Table 5.1.
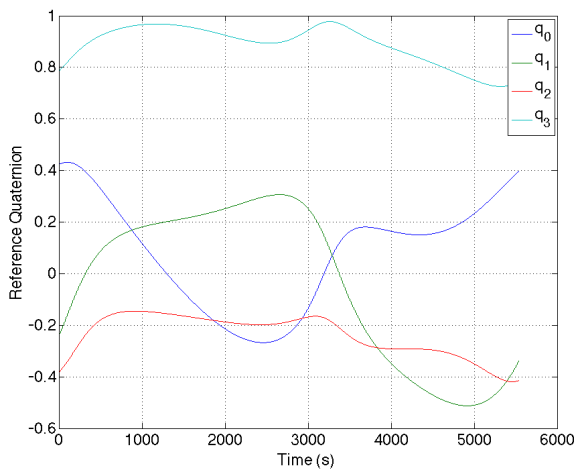
Figure 5.1. Attitude quaternion reference profiles for one relative orbit about the RSO.
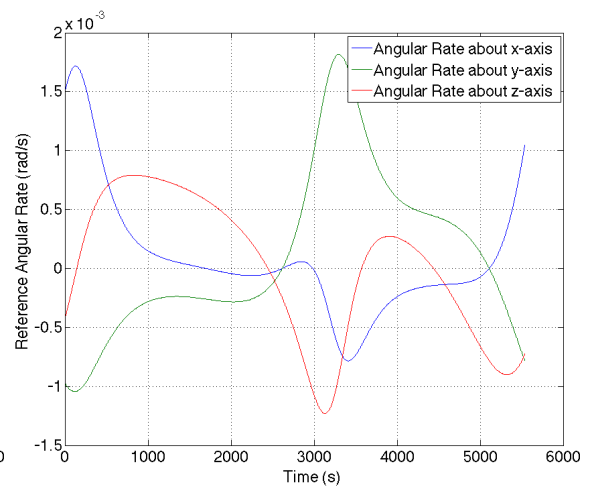
Figure 5.2. Angular rate reference profiles for one relative orbit about the RSO.

Note the maximum allowed simulation step size, $T_{s,sim} = 0.001$ s, is dictated by the actuator model because the simulation must be able to accommodate the minimum pulse width ($t_{min} = 0.002$ s) of the RCS thruster valves.

Table 5.1. Global simulation parameters.

Parameter	Symbol	Value	Units
Initial Attitude	$\bar{\boldsymbol{q}}_i$	$[0.4227, -0.2419, -0.3824, 0.7852]^T$	-
Initial Rate	$\boldsymbol{\omega}_i$	$[1.5, 1.0, 0.4]^T \times 10^{-3}$	$\mathrm{rad\,s^{-1}}$
Orbit altitude	h_{orb}	500	km
Orbit inclination	i_{orb}	28.5	$^\circ$
Distance from RSO	L_{rso}	250	km
RCS thruster frequency	f_{rcs}	10	Hz
Gain schedule transient	t_{gain}	10	s
Rate observer gain	λ	1	
Rate observer gain	γ	2	
Simulation time step	$T_{s,sim}$	1	ms
Simulation start date	-	January 1st, 2015	-

5.2   Target Tracking

This section details the tracking performance of the three main control laws discussed in Chapter 4, namely eigenaxis control, PID, and modified eigenaxis control with additional integral terms. Each is implemented with EKF, angular rate observer, and image feedback techniques. They are presented in the same chronological order as the ADCS design development. The parameters shown in Table 5.2 apply for all the simulated cases in this section unless otherwise specified.

Table 5.2. Simualtion parameters for target tracking with eigenaxis control.

Parameter	Symbol	Value	Units
Solver	-	ode4	-
Eigenaxis proportional gain	p	1	-
Eigenaxis derivative gain	d	0.25	-

5.2.1   Eigenaxis Control

The following set of simulations use only fixed gain eigenaxis control as described by Equation (4.3). Since there are no integral or time derivative $\boldsymbol{q}_{e_v}$ terms, this control configuration is ill suited for image feedback. Therefore, only the results for the EKF and rate observer are shown. Note that the two estimators address, different needs in the system. The EKF will propagate the STR quaternion solution such that state estimates are available at each simulation time step whereas the observer will extrapolate the STR output and give an estimate of the body angular rate at each simulation time step.

EKF Feedback

The eigenaxis control with EKF feedback simulation assumes that both sensors are sampling at their respective maximum rates to obtain the best estimates possible. However, as seen in Figure 5.3, the pointing performance still suffers because the EKF is not designed to account for the white noise in the gyro measurements. The pointing performance remains constant with a steady-state error of approximately 35 arcmin. While this configuration produces error outside the acceptable performance range for imaging operations, it is a stable system that can be implemented during mission modes where pointing requirements are not as stringent and STR measurements are unavailable.

Table 5.3. Simulation parameters for target tracking with eigenaxis control and EKF simulation

Parameter	Symbol	Value	Units
Solver	-	ode3	-
Gyro sampling frequency	f_{gyro}	50	Hz
STR sampling frequency	f_{str}	5	Hz
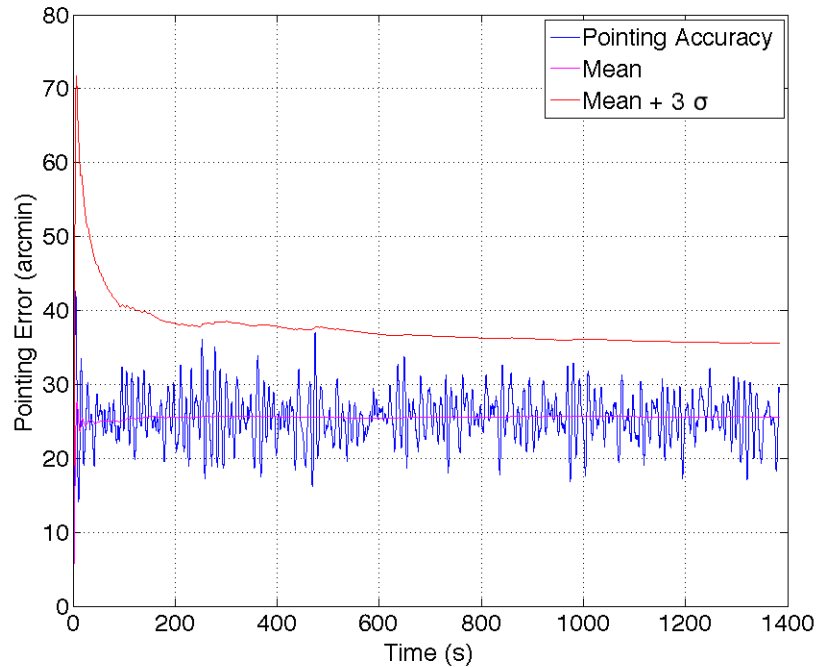
Figure 5.3. Target tracking performance of eigenaxis controller with EKF feedback.

Observer Feedback

The eigenaxis and angular rate observer simulation does not require a gyro measurement input, additionally the STR sampling rate is relaxed to $1\,\mathrm{Hz}$. This was determined to be the smallest sampling rate able to achieve the $3\,\sigma$ pointing requirement (Figure 5.4). Although this configuration yields good performance it is dependent on the STR being within its nominal operation range. In practice, regions in which

the sensor is saturated by sunlight would produce long delays or large errors in the STR solution which could lead to an unstable satellite. In these situations, the EKF feedback configuration would better preserve stability.

Table 5.4. Simulation parameters for target tracking using eigenaxis control with angular rate observer feedback.

Parameter	Symbol	Value	Units
Gyro sampling frequency	f_{gyro}	n/a	Hz
STR sampling frequency	f_{str}	1	Hz
Observer frequency	$1/T_{s,sim}$	1	MHz

Note that the observer frequency listed in Table 5.4 corresponds to the output frequency of the STR quaternion extrapolator.
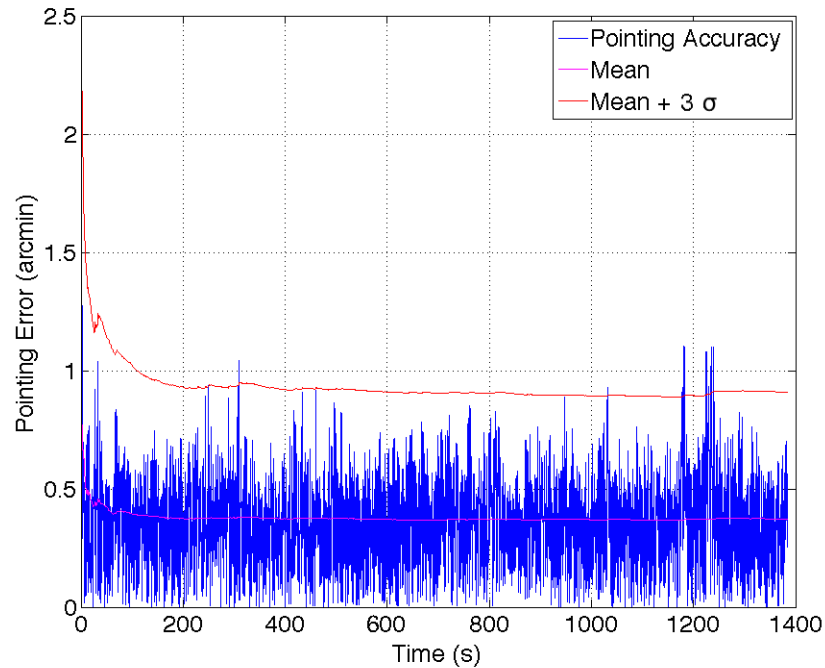
Figure 5.4. Target tracking performance of eigenaxis controller with angular rate observer feedback.

5.2.2 Eigenaxis & PID Control

The following set of simulations use a combination of fixed gain eigenaxis control and PID control with gain scheduling at the moment of switch. In each case, the eigenaxis control is used on the system for the first 250 s. Afterwards, the control switches to PID control with gains determined by Equation (4.5); the corresponding initial and final gain values are listed on Table 5.5.

The periodic 'jumps' in the running mean and deviation plots correspond to resets in the calculation. These are scheduled a preset amount of time after each control switch in order to give a better representation of the 3σ pointing performance.

Table 5.5. Simulation parameters for target tracking using PID and eigenaxis control.

Parameter	Symbol	Value	Units
PID proportional gain at switch	p_1	0.35	-
PID derivative gain at switch	d_1	0	-
PID integral gain at switch	i_1	0	-
PID proportional gain post-switch	p_2	0.75	-
PID derivative gain post-switch	d_2	0.50	-
PID integral gain post-switch	i_2	0.025	-

EKF Feedback

During the first 250 s the pointing performance is similar to the one observed in Figure 5.3. After the scheduled switch, the advantage of the PID control with EKF becomes apparent. Since the PID controller's only input is the error quaternion, there is a marked improvement in the pointing error (Figure 5.5). However, from Figure 5.6 we can see that it takes approximately 2000 s for the 3σ line to converge to a value

below 1 arcmin. Smaller error values are possible with extended simulation time but

the capabilities of this configuration are clear from these results. In practice, the

convergence issue can be avoided by allowing the EKF to converge during maneuvers

with more relaxed pointing requirements before commencing imaging operations.

Table 5.6. Simulation parameters for target tracking using PID and eigenaxis control with EKF feedback.

| Parameter	Symbol	Value	Units
Solver	-	ode3	-
Gyro sampling frequency	f_{gyro}	50	Hz
STR sampling frequency	f_{str}	5	Hz
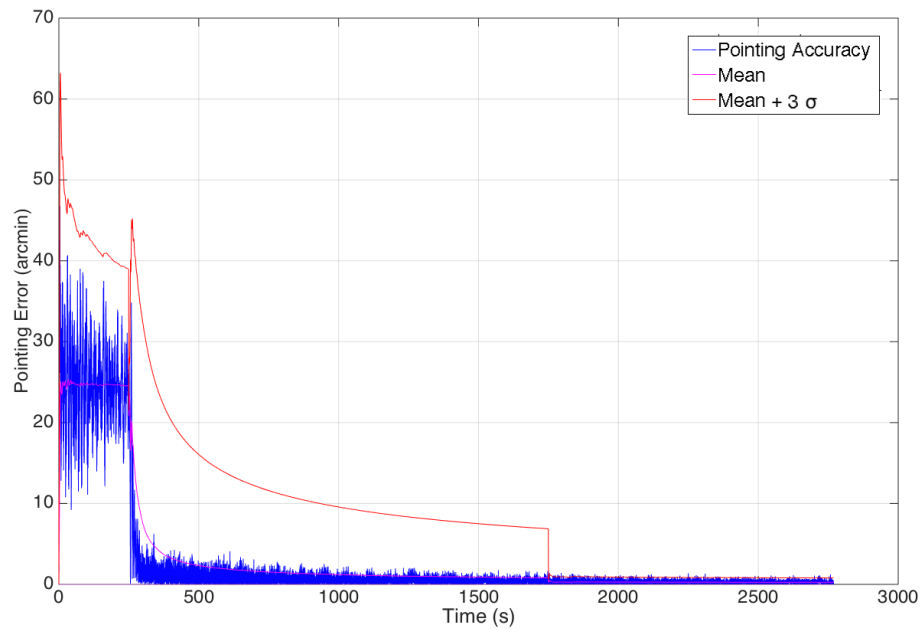
Figure 5.5. Target tracking performance of eigenaxis and PID controllers with EKF feedback. The switch to PID control occurs at 250 s.
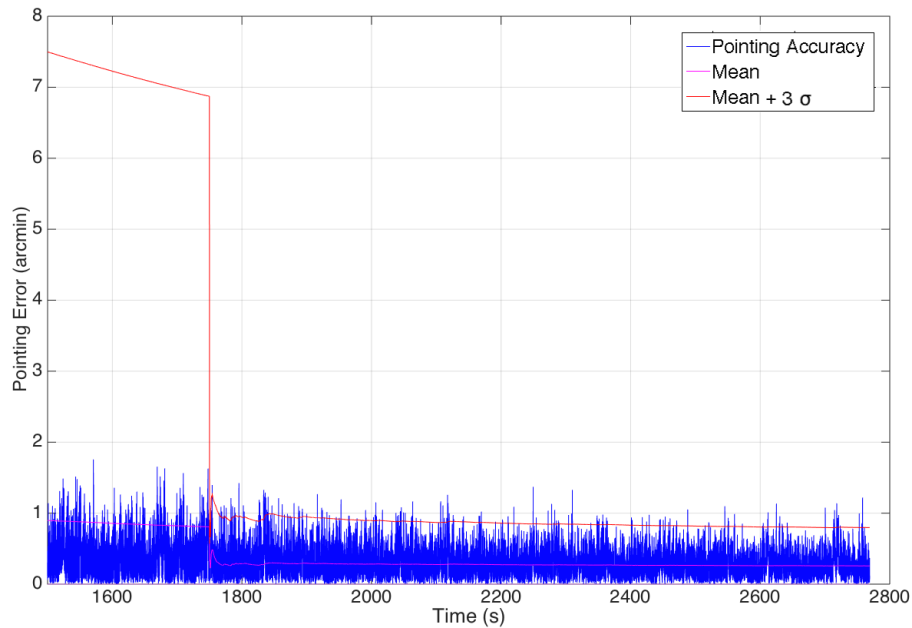
Figure 5.6. Tracking performance of PID controller with EKF feedback.

Observer Feedback

As with the previous case, the performance before the control switch is similar to that in the simulation with no PID control (Figure 5.7). However, there is no appreciable improvement in pointing error after the switch. As mentioned previously in Section 4.3 the similarity in pointing performance suggests the added complexity of a switching controller is unwarranted.

Table 5.7. Simulation parameters for target tracking using PID and eigenaxis control with angular rate observer feedback.

Parameter	Symbol	Value	Units
Gyro sampling frequency	f_{gyro}	n/a	Hz
STR sampling frequency	f_{str}	1	Hz
Observer frequency	$1/T_{s,sim}$	1	MHz
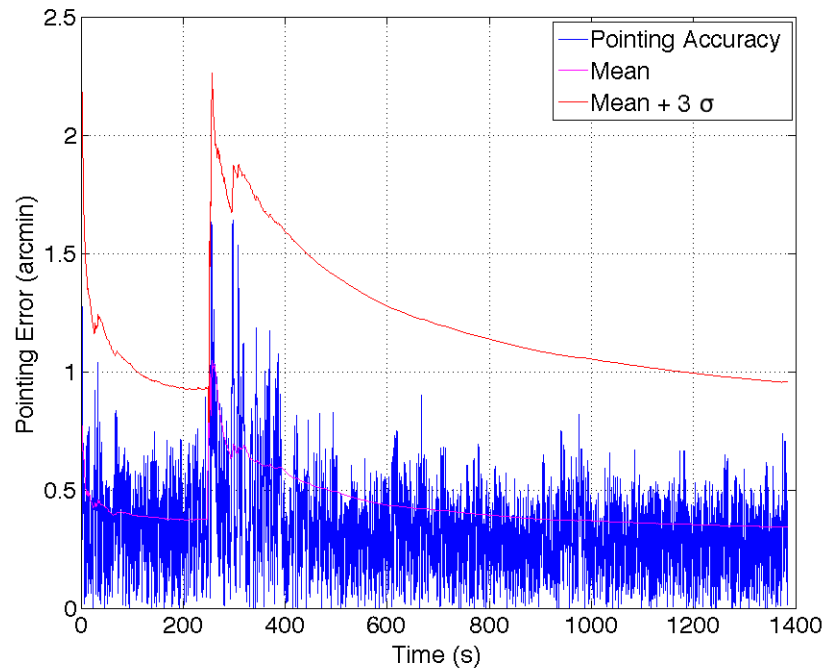
Figure 5.7. Target tracking performance of eigenaxis and PID controllers with angular rate observer feedback. The switch to PID occurs at 250 s.

Image Feedback

This simulation predicts the scenario in which the ARAPAIMA mission navigation algorithms provide a biased solution for the RSO location. The payload cameras are then used to provide unbiased image feedback by calculating the RSO's vertical and horizontal offsets from the center of the frame. For this simulation, Equation (4.8) is used to calculate the offsets from the reference signal.

During the first portion of the simulation a constant 1° bias is added to the feedback signal from the angular rate observer, which causes the fixed gain eigenaxis controller to reach a steady-state error of 60 arcmin. After 250 s, two simultaneous switches occur: the controller input changes to image feedback as described in Equation (4.7),

and the eignaxis control switches to PID control. In this case, the scheduled PID gains are listed in Table 5.8. After the switch, the pointing error is quickly reduced to a $3\,\sigma$ value of less than $0.3\,\text{arcmin}$ (Figure 5.10).

Table 5.8. Simulation parameters for RSO frame centering using PID and eigenaxis control with payload image feedback.

Parameter	Symbol	Value	Units
PID proportional gain at switch	p_1	2.0×10^{-3}	-
PID derivative gain at switch	d_1	1.25×10^{-3}	-
PID integral gain at switch	i_1	0	-
PID proportional gain post-switch	p_2	5.0×10^{-3}	-
PID derivative gain post-switch	d_2	2.0×10^{-3}	-
PID integral gain post-switch	i_2	5.0×10^{-4}	-
Gyro sampling frequency	f_{gyro}	50	Hz
STR sampling frequency	f_{str}	5	Hz
Observer frequency	$1/T_{s,sim}$	1	MHz
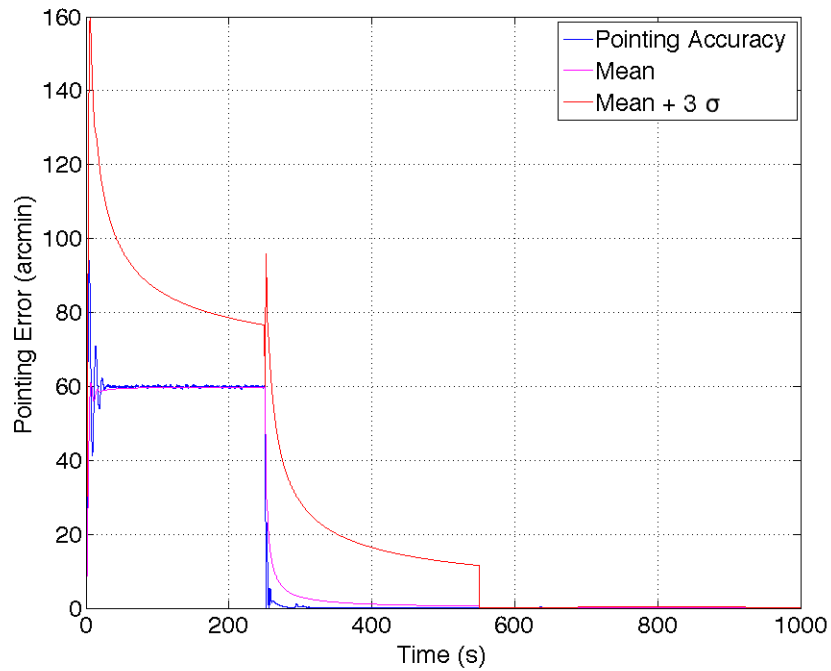
Figure 5.8. Target tracking performance during frame centering maneuver using eigenaxis control with biased rate observer feedback, and PID control with unbiased payload image feedback after 250 s.

Figure 5.9. Tracking performance of eigenaxis controller with biased angular rate observer feedback.
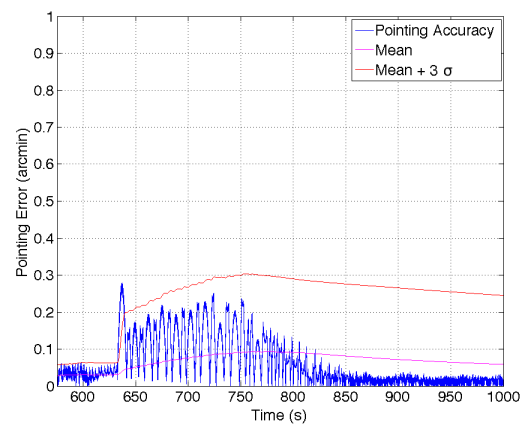
Figure 5.10. Frame centering performance of PID controller using payload camera image feedback.

5.2.3 Eigenaxis with Integral Control

Elaborating on the observation in Section 5.2.2, the next set of simulations follow the same sequence as the previous set but, instead of having two separate control laws, Equation (4.12) is used for all three cases. This allows different tracking scenarios to be associated with a specific set of gains instead of having multiple control laws, which reduces the complexity of the control system. The scheduled gains are as listed in Table 5.9 unless otherwise specified.

Table 5.9. Simulation parameters for eigenaxis control using gain scheduled integral terms.

Parameter	Symbol	Value	Units
Eigenaxis proportional gain	p	1	-
Eigenaxis derivative gain	d	0.25	-
Eigeanxis integral gain	i	0	-
Eigenaxis visual gain	v	0	-
Proportional gain at switch	p_1	0.5	-
Derivative gain at switch	d_1	0.125	-
Integral gain at switch	i_1	0	-
Visual gain at switch	v_1	0	-
Post-switch proportional gain	p_2	1	-
Post-switch derivative gain	d_2	0.5	-
Post-switch integral gain	i_2	0.05	-
Post-switch visual gain	v_2	0	-

EKF Feedback

The EKF feedback performance behaves as before during the first portion of the simulation. Figure 5.11 shows a significant improvement in performance after the gain switch but there is a mean steady state error of approximately 5 arcmin. This

occurs because the controller still requires an $\boldsymbol{\omega}_e$ input, which includes the modeled gyro white noise.

Table 5.10. Simulation parameters for eigenaxis control with gain scheduled integral terms and EKF feedback.

Parameter	Symbol	Value	Units
Solver	-	ode3	-
Gyro sampling frequency	f_{gyro}	50	Hz
STR sampling frequency	f_{str}	5	Hz
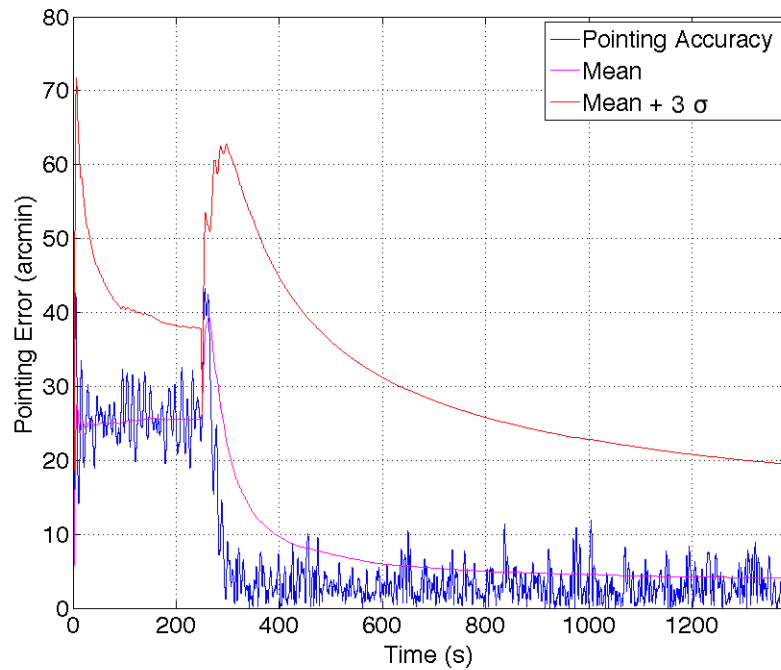
Figure 5.11. Target tracking performance of eigenaxis control with scheduled integral gains and EKF feedback. Integral control switches 'on' at $250\,\mathrm{s}$

Observer Feedback

Figure 5.12 shows no appreciable difference between the tracking performance of the fixed gain eigenaxis controller and the eigenaxis controller with scheduled integral gain. Moreover, its 0.35 arcmin mean accuracy is equivalent to that of the PID controller with observer feedback.

Table 5.11. Simulation parameters for eigenaxis control with gain scheduled integral terms and angular rate observer feedback.

| Parameter	Symbol	Value	Units
Gyro sampling frequency	f_{gyro}	n/a	Hz
STR sampling frequency	f_{str}	1	Hz
Observer frequency	$1/T_{s,sim}$	1	MHz
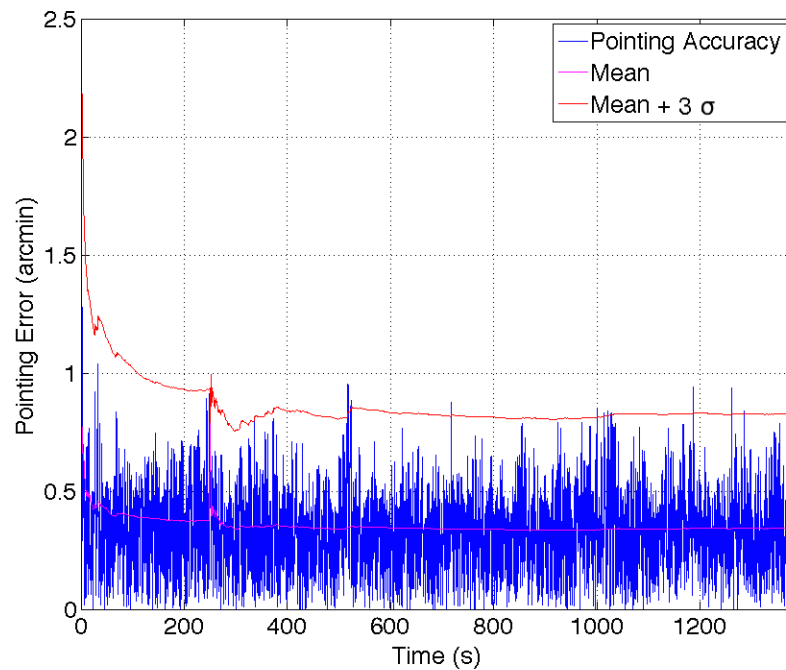
Figure 5.12. Target tracking performance of eigenaxis controller with scheduled integral gains and angular rate observer feedback. Integral control switches 'on' at 250 s.

Image Feedback

The tracking performance of the modified eigenaxis controller during the image feedback maneuver is nearly identical to that of the PID controller in the previous simulation set. Together with the observer feedback performance, the simulation results suggest the same level of accuracy is achievable without the additional complexity of controller switching.

Table 5.12. Simulation parameters for eigenaxis control with scheduled integral and visual gains using angular rate observer feedback.

Parameter	Symbol	Value	Units
Proportional gain at switch	p_1	2.0×10^{-3}	-
Derivative gain at switch	d_1	0	-
Integral gain at switch	i_1	0	-
Visual gain at switch	v_1	1.25×10^{-3}	-
Post-switch proportional gain	p_2	5.0×10^{-3}	-
Post-switch derivative gain	d_2	0	-
Post-switch integral gain	i_2	5.0×10^{-4}	-
Post-switch visual gain	v_2	2.0×10^{-3}	-
Gyro sampling frequency	f_{gyro}	n/a	Hz
STR sampling frequency	f_{str}	1	Hz
Observer frequency	$1/T_{s,sim}$	1	MHz

Figure 5.13. Target tracking performance of eigenaxis controller with scheduled i and v gains using biased angular rate observer feedback. Unbiased payload image feedback begins after $250\,\text{s}$.
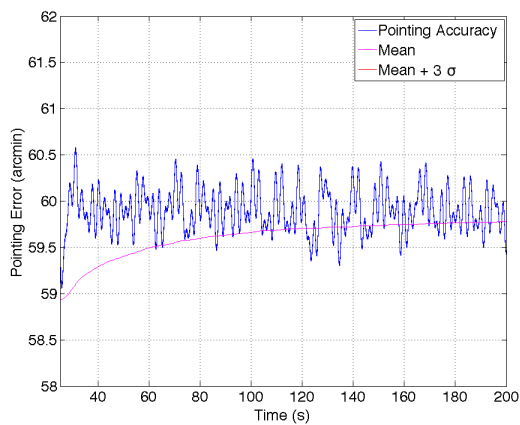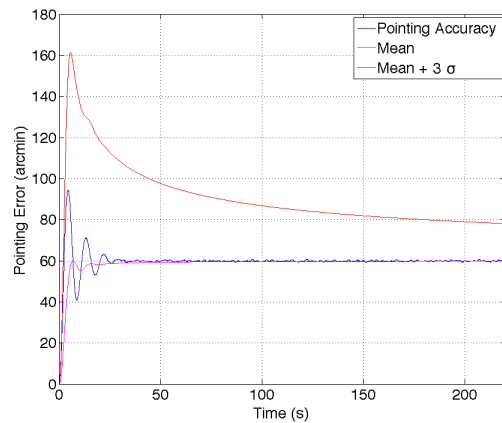

Figure 5.14. Target tracking performance using eigenaxis control with biased angular rate observer feedback.
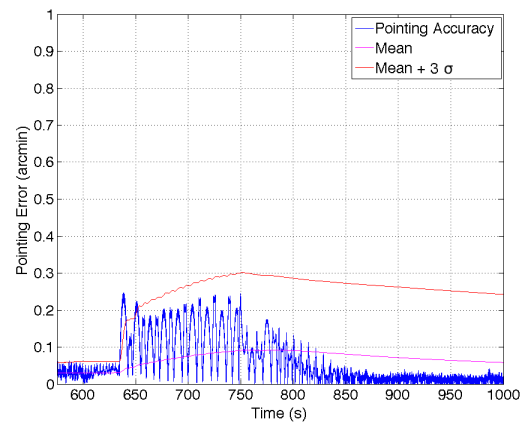
Figure 5.15. Frame centering performance of eigenaxis controller using i_2 and v_2 gains.

5.3   Detumbling

The angular rate observer requires the STR to provide nominal attitude solutions at all times in order to meet imaging accuracy requirements. This means the STR must be kept out of direct sunlight, and the body angular rates must not exceed the specified $1\,°\,\text{s}^{-1}$ limit. A simple PI controller is shown here to demonstrate the satellite is capable of executing detumbling maneuvers.

Worst case scenario deployment conditions expect initial rotation rates of $10\,°\,\text{s}^{-1}$ about each body axis. Figure 5.16 shows the angular rates are reduced to zero in a case with ideal sensor feedback. Figure 5.16 shows how the angular rates converge to approximately $0.01\,\text{rad}\,\text{s}^{-1}$ ($0.57\,°\,\text{s}^{-1}$) when receiving unfiltered gyro measurements. This offset, attributed to the sensor measurement bias, leaves a small error margin to satisfy the nominal STR performance conditions. However, the STR is able to provide attitude solutions with sufficient accuracy to exit detumbling mode when the angular rates are below $0.07\,\text{rad}\,\text{s}^{-1}$ ($4\,°\,\text{s}^{-1}$). After continuing to target tracking operations, the angular rates are limited by the progression of the reference attitude profile. Note that detumbling should only occur once during the mission lifetime.

Table 5.13. Simulation parameters for PID detumbling control using direct sensor feedback.

Parameter	Symbol	Value	Units
Initial angular rates	$\boldsymbol{\omega}_0$	$[0.175, 0.175, 0.175]^T$	$\text{rad}\,\text{s}^{-1}$
Detumble PID proportional gain	p	1	-
Detumble PID derivative gain	d	0	-
Detumble PID integral gain	i	0.05	-
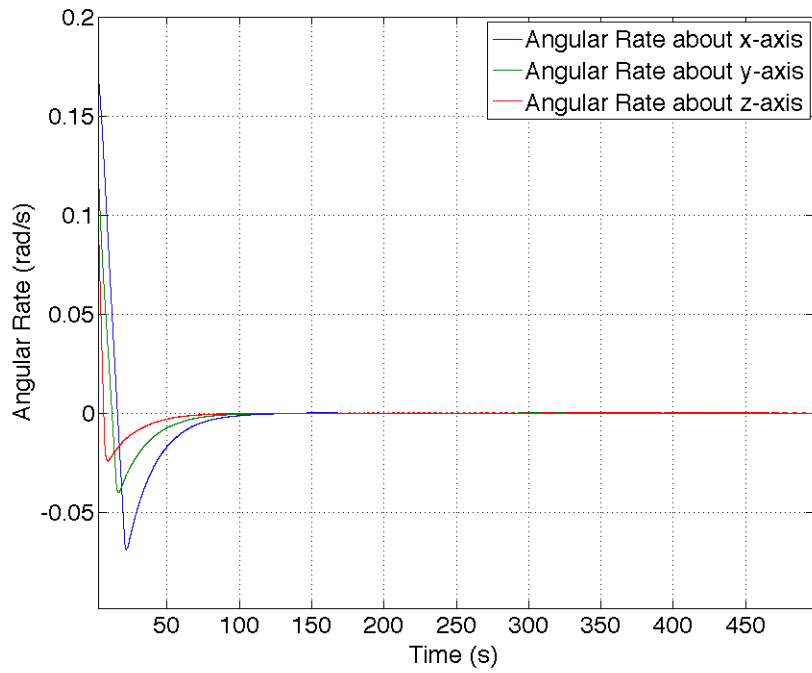
Figure 5.16. Detumbling performance of PID controller with ideal sensor feedback.
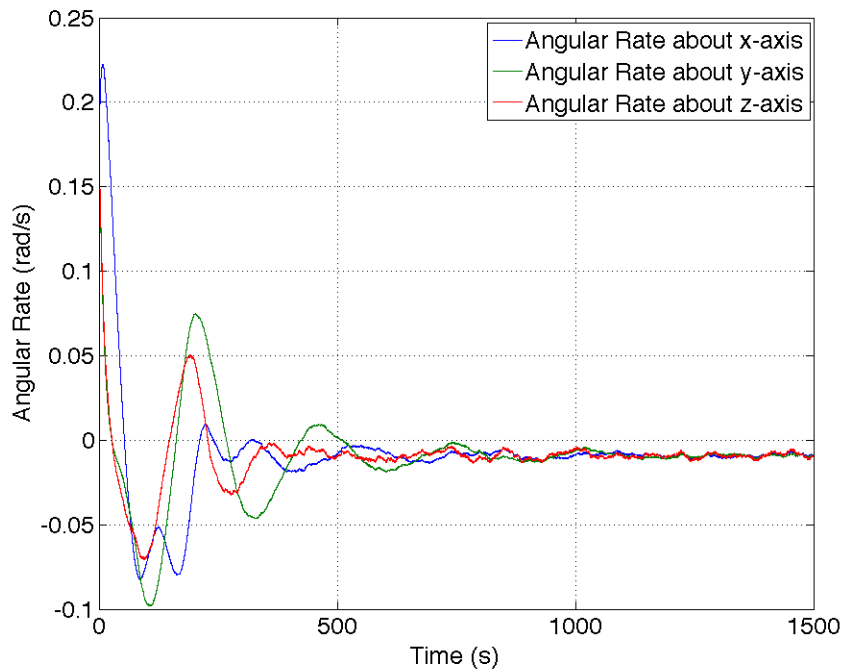
Figure 5.17. Detumbling performance of PID controller with modeled sensor noise feedback.

5.4   Multiple Maneuver Control

This simulation evaluates the performance of the ADCS throughout multiple maneuvers. The scenario begins with a detumbling maneuver during which the controller receives unfiltered gyro measurements at a rate of $50\,\mathrm{Hz}$. After $500\,\mathrm{s}$, the body angular rates are within the off-nominal operation range of the STR and the ADCS begins receiving STR solution updates at a rate of $1\,\mathrm{Hz}$. At this point the controller switches to the modified eignaxis control law with p, d, i, and v gains as listed in Table 5.14. The body then performs a fast slew maneuver (Figure 5.19) as it initiates target tracking operations. It is important to note the controller does not keep track of the pointing error during detumbling maneuvers. It is shown in Figure 5.18 only to demonstrate the ADCS's ability to manage large initial offsets.

From $500\,\mathrm{s}$ to $1000\,\mathrm{s}$ the controller tracks the RSO as it receives state estimates from the angular rate observer. However, the quaternion reference signal received thus far incorporates a $1°$ bias. Therefore, the controller achieves a steady state error of approximately $60\,\mathrm{arcmin}$. After $1000\,\mathrm{s}$, gain scheduling is used to begin image feedback operations. The pointing error quickly decreases to within target performance, and at $1300\,\mathrm{s}$ the updated running deviation confirms a $3\,\sigma$ pointing error of $0.6\,\mathrm{arcmin}$ (Figure 5.20). The performance continues to improve gradually until the end of the simulation.

Table 5.14. Simulation parameters for a multiple maneuver operation using scheduled eigenaxis control.

Parameter	Symbol	Value	Units
Initial angular rates	$\boldsymbol{\omega}_0$	$[0.175, 0.175, 0.175]^T$	$\mathrm{rad\,s^{-1}}$
Detumble PID proportional gain	p	1	-
Detumble PID derivative gain	d	0.05	-
Detumble PID integral gain	i	0.5	-
Eigenaxis proportional gain	p	1	-
Eigenaxis derivative gain	d	0.25	-
Eigenaxis integral gain	i	0	-
Eigenaxis visual gain	v	0	-
Proportional gain at switch	p_1	2.0×10^{-3}	-
Derivative gain at switch	d_1	0	-
Integral gain at switch	i_1	0	-
Visual gain at switch	v_1	1.25×10^{-3}	-
Post-switch proportional gain	p_2	5.0×10^{-3}	-
Post-switch derivative gain	d_2	0	-
Post-switch integral gain	i_2	5.0×10^{-4}	-
Post-switch visual gain	v_2	2.0×10^{-3}	-
Gyro sampling frequency	f_{gyro}	50	Hz
STR sampling frequency	f_{str}	1	Hz
Extrapolated frequency	$1/T_{s,sim}$	1	MHz
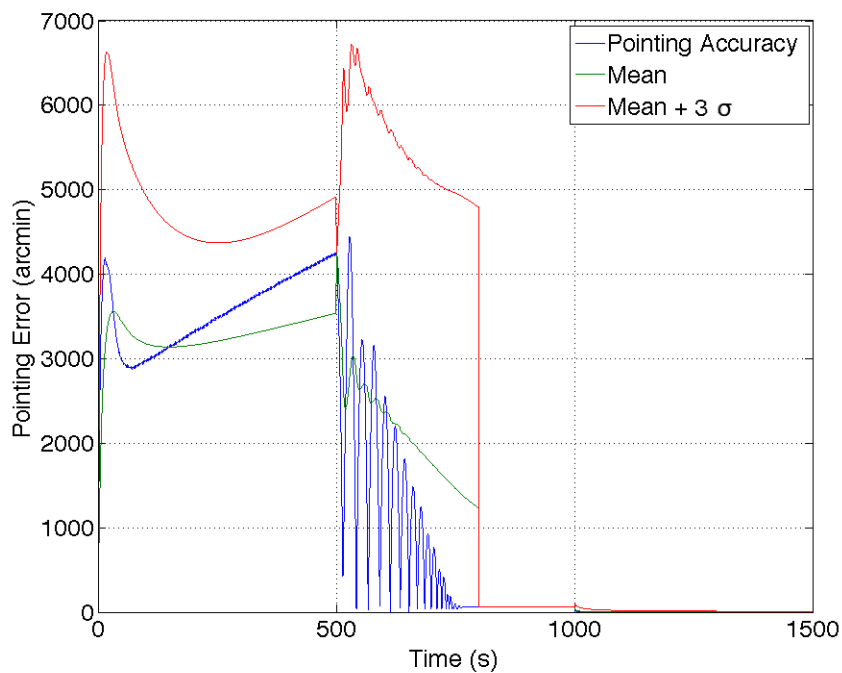
Figure 5.18. Tracking performance of a multiple maneuver simulation, which includes (in order) detumbling, slew, biased target tracking, and frame centering.
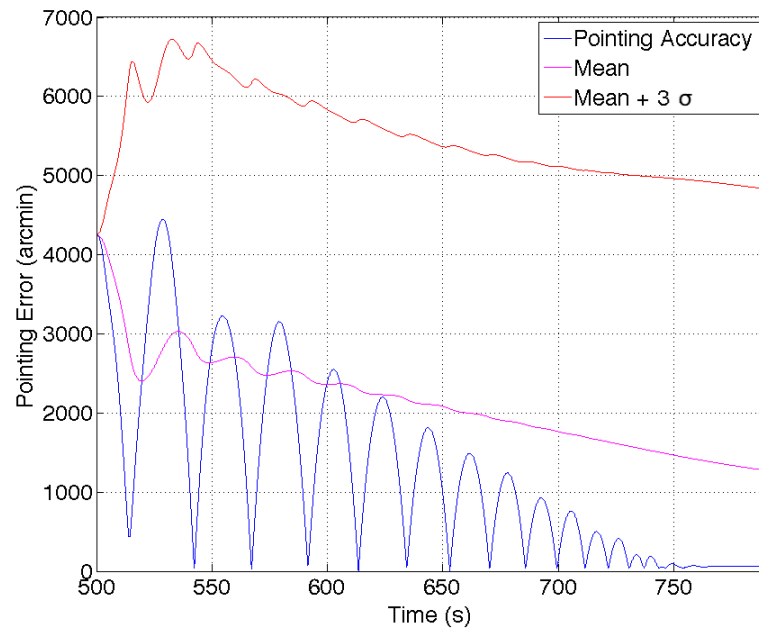
Figure 5.19. Performance of fast slew maneuver from a large arbitrary angle to target tracking using eigenaxis control with biased observer feedback.
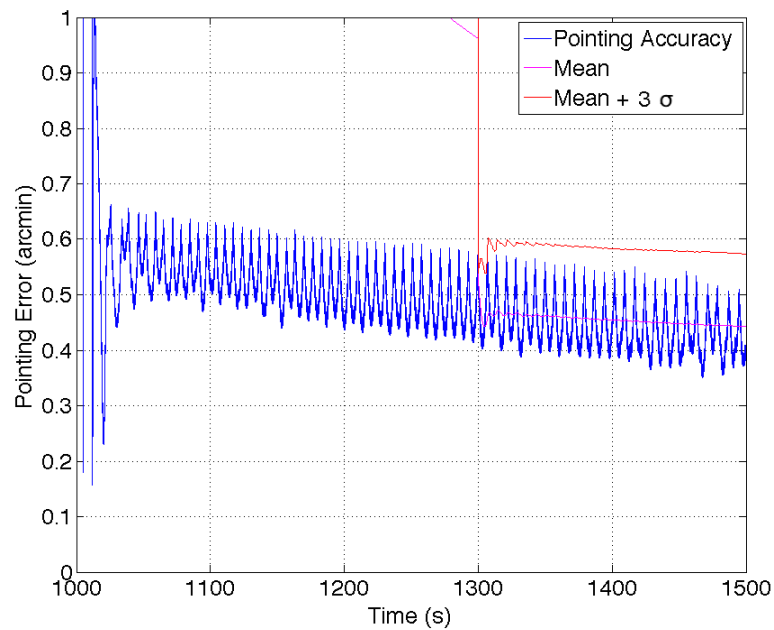
Figure 5.20. Frame centering performance of eigenaxis controller with unbiased image feedback.

5.5 Digital Control

The discrete ADCS is implemented directly into the previous simulation model by specifying the data rate transitions between the plant, controller, and estimator subsystems. The continuous plant states are sampled at the specified sensor rates and then propagated at an estimator frequency f_{obs} (f_{ekf} for the EKF). The state estimates are further down-sampled at the desired controller frequency. The controller output is subject to further computational delays, the worst case of which is a unit delay equal to the controller time step. This output is fed directly to the RCS thruster actuator model which adds an additional delay corresponding to the inverse of its operating frequency. The discrete controller block diagram is shown in Figure C.6.

The following set of simulations show the performance of the discrete modified eigenaxis controller (Equation (4.19)). The simulated scenarios are the same as for the continuous controller. Further discussion and performance comparisons to previous configurations are presented in the following section.

Table 5.15. Simulation parameters for discrete eigenaxis control with scheduled integral terms

Parameter	Symbol	Value	Units
Eigenaxis proportional gain	p	1	-
Eigenaxis derivative gain	d	0.25	-
Eigenaxis integral gain	i	0	-
Eigenaxis visual gain	v	0	-
Proportional gain at switch	p_1	0.5	-
Derivative gain at switch	d_1	0.125	-
Integral gain at switch	i_1	0	-
Visual gain at switch	v_1	0	-
Post-switch proportional gain	p_2	1	-
Post-switch derivative gain	d_2	0.5	-
Post-switch integral gain	i_2	0.05	-
Post-switch visual gain	v_2	0	-
Controller frequency	$10/T_{s,sim}$	100	Hz

EKF Feedback

Table 5.16. Simulation parameters for discrete eigenaxis control with gain scheduled integral terms and EKF feedback.

Parameter	Symbol	Value	Units
Solver	-	ode3	-
Gyro sampling frequency	f_{gyro}	50	Hz
STR sampling frequency	f_{str}	5	Hz
EKF frequency	$f_{s,ekf}$	1	MHz
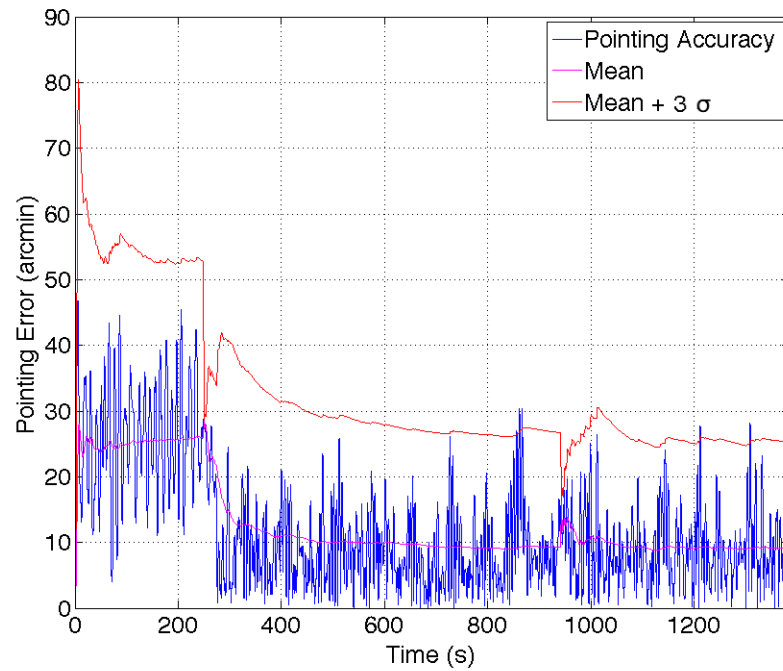
Figure 5.21. Target tracking performance of discrete eigenaxis controller with scheduled integral gains and EKF feedback.

Observer Feedback

Table 5.17. Simulation parameters for discrete eigenaxis control with gain scheduled integral gains and angular rate observer feedback.

| Parameter	Symbol	Value	Units
Gyro sampling frequency	f_{gyro}	n/a	Hz
STR sampling frequency	f_{str}	1	Hz
Observer frequency	$f_{s,obs}$	1	MHz
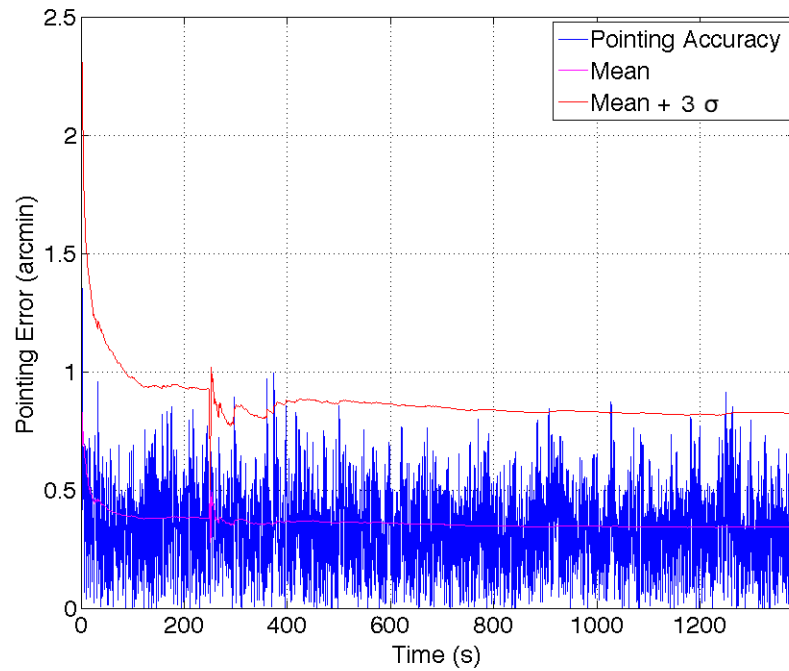
Figure 5.22. Target tracking performance of discrete eigenaxis controller with scheduled integral gains and angular rate observer feedback.

Image Feedback

Table 5.18. Simulation parameters for discrete eigenaxis control with scheduled integral and visual gains using angular rate observer feedback.

Parameter	Symbol	Value	Units
Proportional gain at switch	p_1	2.0×10^{-3}	-
Derivative gain at switch	d_1	0	-
Integral gain at switch	i_1	0	-
Visual gain at switch	v_1	1.25×10^{-3}	-
Post-switch proportional gain	p_2	5.0×10^{-3}	-
Post-switch derivative gain	d_2	0	-
Post-switch integral gain	i_2	5.0×10^{-4}	-
Post-switch visual gain	v_2	2.0×10^{-3}	-
Gyro sampling frequency	f_{gyro}	n/a	Hz
STR sampling frequency	f_{str}	1	Hz
Observer frequency	$f_{s,obs}$	1	MHz

Figure 5.23. Target tracking performance of discrete eigenaxis controller with scheduled i and v gains using biased angular rate observer feedback. Frame centering with unbiased payload image feedback begins after $250\,\text{s}$.
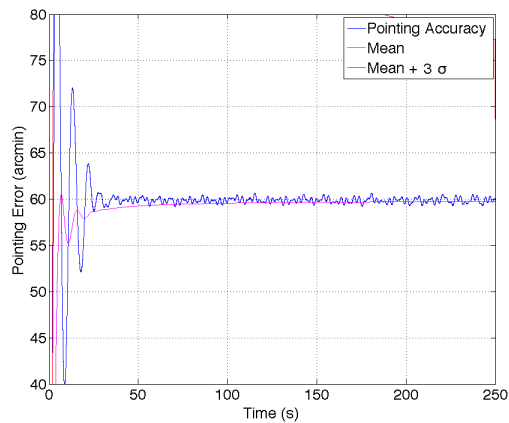
Figure 5.24. Target tracking performance using discrete eigenaxis control with biased angular rate observer feedback.
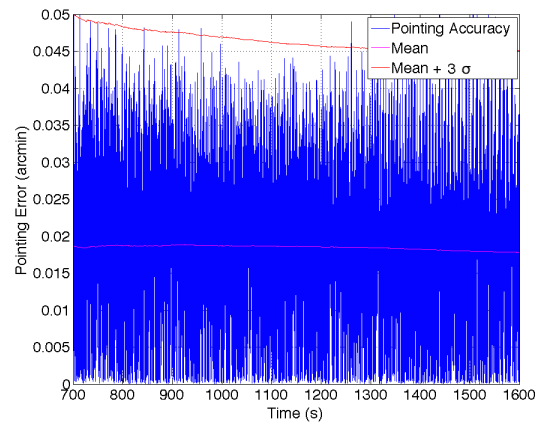
Figure 5.25. Frame centering performance of eigenaxis controller using i_2 and v_2 gains.

5.6 Summary

The performance of the four different control system configurations analyzed in this chapter is summarized in Table 5.19.

The fixed gain eigenaxis controller is the simplest configuration that produces a stable system but it only meets the imaging requirements with the rate observer output. Furthermore, it is incompatible with image feedback.

The PID controller performs best when used with the EKF; however the EKF is slower to converge than the rate observer. For all other cases, there is no other significant improvement in performance over the fixed gain eigenaxis controller to justify having two separate control algorithms

The modified, scheduled gain eigenaxis controller with integral terms is unable to meet imaging requirements when used with the EKF. Otherwise, the only improvement over its previous configuration is compatibility with image feedback. In this regard, it was able to match the PID performance.

The discrete modified eigenaxis controller performance suffers more than its continuous counterpart when used with the EKF due to the reduced controller sampling rate. However, the image feedback performance benefits from this delay because it creates a 'deadband' effect. Thus allowing the error more time to converge in between controller outputs.

Table 5.19. Target tracking mean pointing accuracy

Controller	EKF (arcmin)	Rate Observer (arcmin)	Image Feedback (arcmin)
Fixed gain eigenaxis	25	0.35	n/a
Scheduled gain PID	0.25	0.35	0.05
Scheduled gain eigenaxis	5	0.35	0.05
Discrete eigenaxis with scheduled gains	10	0.35	0.02

Controller Selection

A total of twelve configurations corresponding to four controllers, and three different feedback sources (see Tables 5.1 and 5.13) are discussed throughout this thesis. Though extensive, their combined results quantify the ADCS performance in terms of pointing accuracy.

Selecting a control law for the ARAPAIMA mission, however, is not a straight forward matter. In conversational terms, ARAPAIMA needs a "controller for all occasions". In other words, the ideal choice would be a controller which gives the best imaging performance but is also able to fulfill the requirements of all other operational modes. Regrettably, no single controller configuration can accommodate all these conditions. Therefore, the best alternative is determined by considering the different possible mission constraints.

Firstly, the controller must be able to satisfy the $1\,\mathrm{arcmin}$ ($3\,\sigma$) during imaging and tracking requirements. Only eight of the twelve configurations fulfill this condition. Of those eight, only the scheduled gain PID controller can do so with EKF feedback.

Second, the controller must be compatible with image feedback techniques to correct possible bias in the reference signal. This eliminates the fixed eigenaxis gain controller since it does not accept projection parameter inputs.

Third, the controller must be as simple as possible without affecting the pointing performance. The PID controller, requires simultaneous gain scheduling and control law switching. This presents an unnecessary risk to the mission, therefore, the PID is not a viable option.

At this point we are left with two choices: the continuous and discrete modified eigenaxis controllers, each with rate observer and image feedback. However, the controller must run on the ARAPAIMA OBC and account for the different (and possibly varying) sensor rates. The only possible choice then is the discrete modified eigenaxis control with rate observer and image feedback. Therefore the current control law of the ARAPAIMA ADCS is

$$\boldsymbol{M}_{cmd} = -\boldsymbol{J}\left[d\boldsymbol{\omega}_e + \left(p + i\frac{T_s}{z-1}F(z) + v\frac{N}{1 + N\frac{T_s}{z-1}F(z)}\right)\boldsymbol{q}_{e_v}\right].$$

6. Conclusions

The design approach of the ADCS presented in this thesis gives more focus to the level of detail and sophistication of the simulation models than to the theoretical backbone of each topic. However, the aim of such an approach is not to develop new theories, but to instead utilize those that are already well known and available to create new practices. Much of the work presented here, although not groundbreaking in its separate fields, is new in its application to small satellites.

Rather than include an abundance of assumptions that oversimplify the design process, every detail is considered in an effort to make the most comprehensive plant model possible. To an extent, the bulk this work is modular and can be applied to any arbitrary satellite mission in LEO. However, the portions specific to the ARAPAIMA mission introduce a depth of analysis not present in traditional academic design exercises. To this end, a considerable amount of this work's value lies not only in its implementation, but also in its development. The completed model's capabilities exceed those of a control loop simulation and can provide system level information such as dynamic behavior, expended electrical power, propellant consumption, and orbit trajectory perturbations.

The result of this design approach constitutes a proof-of-concept for an academic CubeSat platform proximity operation mission through extensive examination and interpretation of simulated data.

7. Recommendations

A number of models within the simulation can be improved further; most of these improvements involve simplifying the code structure and replacing embedded code with Simulink S-functions in order to decrease run time. Currently, the average performance is 30 virtual seconds per second for the continuous time models, and 50 virtual seconds per second for the discrete controllers.

7.1 Future Work

Aside from changes to the simulation there are mission scenarios and ADCS improvements te be considered:

The stability analysis presented in Section 4.3.3 needs to be developed further. Particularly, a non-linear stability proof is needed to consider input switching scenarios.

The ADCS model is advanced enough to begin hardware in-the-loop (HIL) testing and real-time simulations. A dSpace DS006 processor has been obtained for this purpose. This will allow trials with engineering test units and other mission hardware. In time this will lead to integration and testing with other ARAPAIMA subsystems.

As mentioned in Section 5.6, a deadband type effect was observed during the discrete controller simulations. A deadband region is currently being developed which has shown small improvements during fixed gain tracking operations. Further improvement on its implementation is expected to improve the performance of all maneuvers.

The payload image feedback process needs to be modified to accept real images and determine the projection parameters directly from them without having access to the attitude quaternion.

Lastly, the controller and observer algorithms need to be tested for the scenario in which optical measurements are unavailable from both the STR and the payload optical array.

REFERENCES

Bird, G. A. (1994). *Molecular gas dynamics and the direct simulation of gas flows.* Oxford University Press, USA.

Curtis, H. (2013). *Orbital mechanics for engineering students* (3rd ed.). Butterworth-Heinemann.

Dodge, F. T. (2010). *The new dynamic behavior of liquids in moving containers.* Southwest Research Institute.

Flenniken, W. S. (2005). *Modeling inertial measurement units and analyzing the effect of their errors in navigation applications* (Unpublished master's thesis). Auburn University.

Franklin, G. F., Powell, J. D., & Workman, M. L. (1990). *Digital control of dynamic systems* (2nd ed.). Addison-Wesley Publishing Company.

G. Blesser, D. S. (n.d.). *Using the kalman filter extended kalman filter.* (Lecture notes from Deutsche Forschungszentrum für Künstliche Intelligenz GmbH)

Harris, K., McGarvey, M., Chang, H. Y., Ryle, M., II, T. R., & Udrea, B. (2013, August). Application for rso automated proximity analysis and imaging (arapaima): Development of a nanosat-based space situational awareness mission. In *Smallsat 2013.* AIAA.

Hedin, A. E. (n.d.). *Msis-e-90 atmoshpere model.* Retrieved July 10th, 2014, from `http://ccmc.gsfc.nasa.gov/modelweb/atmos/msise.html`

Huang, A. (2014, February). *Solenid valve linear operation region.* Personal Communication.

Imagery, N., & Agency, M. (2000). *Department of defense world geodetic system 1984 tr8350.2* (Tech. Rep.). NIMA.

Inamori, T., Sako, N., & Nakasuka, S. (2011). Compensation of time-variable magnetic moments for a precise attitude control in nano-and micro-satellite missions. *Advances in Space Research*, *48*(3), 432-440.

Kuipers, J. B. (1999). *Quaternions and rotation sequences a primer with applications to orbits, aerospace, and virtual reality.* Princeton University Press.

Liu, L. (2007). *Jitter and Basic Requirements of the Reaction Wheel Assembly in the Attitude Control System.* Cambridge.

Lyle, R., & Stabekis, P. (1971). *Spacecraft aerodynamic torques (nasa monographs in space vehicle design criteria- guidance and control)* (No. SP-8058). NASA.

MathWorks. (2013, March). Aerospace blockset user's guide 2013a (3.11 ed.) [Computer software manual]. Natick, Massachusetts.

Maus, S., Macmillan, S., McLean, S., Hamilton, B., Thomson, A., Nair, M., & Rollins, C. (2010). *The us/uk world magnetic model for 2010-2015* (Tech. Rep.). NOAA NESDIS/NGDC.

Picone, M., Hedin, A., & Drob, D. (n.d.). *Nrlmsise-00.* Retrieved July 10th, 2014, from `http://ccmc.gsfc.nasa.gov/modelweb/atmos/nrlmsise00.html`

Pong, C. M., Lim, S., Smith, M. W., Miller, D. W., Villaseñor, J. S., & Seager, S. (2010). Achieving high-precision pointing on exoplanetsat: Initial feasibility analysis. *MIT Open Access Articles*.

RikiMunakata. (2009). *Cubesat design specification rev. 12* (Tech. Rep.). California Polytechnic State University.

Schutz, B., Tapley, B., & Born, G. H. (2004). *Statistical orbit determination.* Elsiever Academic Press.

Shuster, M. D. (1993, October-December). A survey of attitude representations. *The Journal of the Astronautical Sciences*, *41*(4), 439-517.

Swartwout, M. (n.d.). *Cubesat database.* Retrieved March 8th, 2015, from `https://sites.google.com/a/slu.edu/swartwout/home/cubesat-database`

Thakur, D., Mazenc, F., & Akella, M. R. (2014, August). Partial Lyapunov Strictification: Smooth Angular Velocity Observers for Attitude Tracking Control. In *Aiaa/aas astrodynamics specialist conference* (pp. 1–18). San Diego, CA: American Institute of Aeronautics and Astronautics. Retrieved from `http://arc.aiaa.org/doi/abs/10.2514/6.2014-4420` doi: 10.2514/6.2014-4420

Vallado, D. A. (2013). *Fundamentals of astrodynamics and applications* (4th ed.). Microcosm Press.

Vazquez, N. (2014, April). *Fuel slosh effects on arapaima attitude control.*

Wertz, J. R., Everett, D. F., & Puschell, J. J. (2011). *Space mission engineering: The new smad* (4th ed.). Microcosm Press.

Wie, B. (1985). Quaternion feedback for spacecraft large angle maneuvers. *Journal of Guidance, Control, and Dynamics*, *8*(3), 360-365.

Wie, B., Bailey, D., & Heiberg, C. (2002). Rapid multitarget acquisition and pointing control of agile spacecraft. *Journal of Guidance, Control, and Dynamics*, *25*(1), 96-104.

Wie, B., & Lu, J. (1995). Feedback control logic for spacecraft eigenaxis rotations under slew rate and control constraints. *Journal of Guidance, Control, and Dynamics*, *18*(6), 1372-1379.

Wie, B., Weiss, H., & Arapostathis, A. (1989, May-June). Quaternion feedback regulator for spacecraft eigenaxis rotations. *Journal of Guidance, Control, and Dynamics*, *12*(3), 375-380.

A. ARAPAIMA Mission Time and Reference Frame Conventions

This document defines the conventions for time systems and reference frames used for the Arapaima mission. The reference frames are divided into three groups, one group comprises the spacecraft-based frames, the second group comprises the orbit-based reference frame, and the third group comprises Earth-based frames.

Reference frames and conventions defined elsewhere in the the main document are omitted.

Time Systems

The time is specified in the Julian Date system (JD), and it has at least eight decimal places. According to (Vallado, 2013), eight decimal digits provide a reasonable accuracy of 4×10^{-4} s. (Note that $1\,\mathrm{s} = 1.1574 \times 10^{-5}$ days.)

Spacecraft-based Reference Frames

The spacecraft-based reference frames are defined below and most of them are presented in Figures A.2 and A.3. All the reference frames are right handed (RH) systems.

Geometric Fixed Reference Frame (GFF)

The GFF is the reference frame with respect to which all the origins and orientations of the other spacecraft-based reference frames are defined and measured. The origin of the GFF is placed at the reference (fiduciary) marker, typically a retro-reflector cube.

Origin : At the spacecraft reference (fiduciary) marker.

O_x : Parallel to some edge of the satellite bus structure. The positive direction on chaser satellite is the opposite of the satellite face with the apertures of the payload instruments.

O_y : Normal to the O_x axis. Positive direction: TBD.

O_z : Completes the RH reference frame.

Laser Rangefinder Reference Frame (L)

The laser range finder reference frame is attached to the receiver telescope of the rangefinder.

Origin : At the spacecraft reference (fiduciary) marker.

O_x : Along the optical axis of the laser rangefinder receiver telescope. The positive direction is towards the aperture of the telescope tube.

O_y : As defined by the instrument maker.

O_z : Completes the RH reference frame.

Infrared Camera Reference Frame (IRC)

The infrared camera reference frame is attached to a camera lens.

Origin : At the spacecraft reference (fiduciary) marker.

O_x : Along the optical axis of the camera. The positive direction is towards the aperture.

O_y : As defined by the instrument maker.

O_z : Completes the RH reference frame.

Monochrome Camera Reference Frame (MC)

The monochrome camera frame is attached to the camera lens.

Origin : As defined by the instrument maker.

O_x : Along the optical axis of the camera. The positive direction is towards the aperture.

O_y : As defined by the instrument maker.

O_z : Completes the RH reference frame.

Star Tracker Reference Frame (STR)

The star tracker reference frame is attached to star tracker optics assembly.

Origin : As defined by the instrument maker.

O_x : Along the optical axis of the star tracker optics assembly. The positive direction is towards the aperture of the optics assembly.

O_y : As defined by the unit manufacturer.
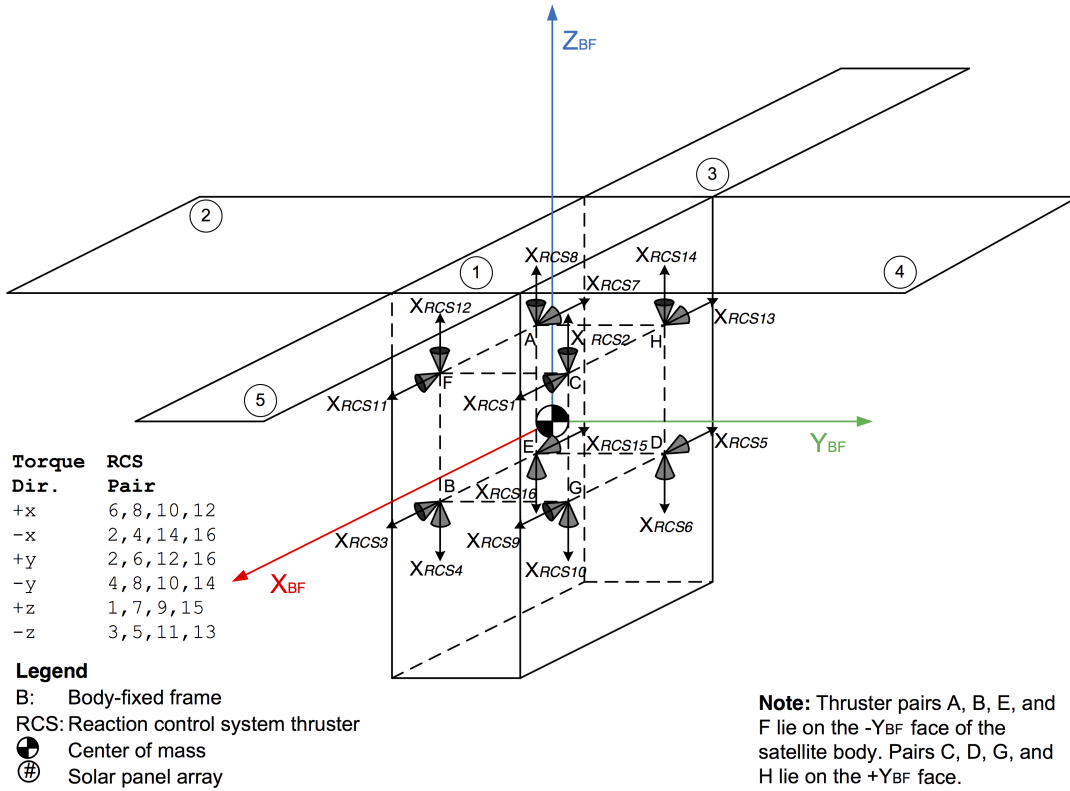
O_z : Completes the RH reference frame.

Figure A.1. RCS thruster placement on satellite body-frame.

Reaction Control System Thruster Reference Frames (RCS)

It is assumed that the reaction control system is made of sixteen thrusters grouped by two in reaction control clusters. They provide attitude control torques about all

body axes in both directions. Cluster C is made of thrusters **one** and **two** and it is installed at the $(-x_{GF}, +z_{GF})$ corner of the satellite bus. Cluster B is made of thrusters **three** and **four** and it is installed at the $(+x_{GF}, -z_{GF})$ corner of the bus. Cluster D is made of thrusters **five** and **six** and it is installed at the $(-x_{GF}, -z_{GF})$ corner of the bus. Cluster A is made of thrusters **seven** and **eight** and is installed at the $(-x_{GF}, +z_{GF})$ corner of the bus. The remaining eight thrusters have been added as redundancy to the system and they complete a mirror image of clusters A, B, C, and D. The origin and axes directions for each RCS thruster reference frame follow the convention described below.

Origin : At the point of application of the reaction force of the respective thruster.

O_x : Along the optical axis of the star tracker optics assembly. The positive direction is towards the aperture of the optics assembly.

O_y : Along the axis of the respective thruster. The positive direction is towards the exhaust plane of the thruster.

O_z : Completes the RH reference frame.
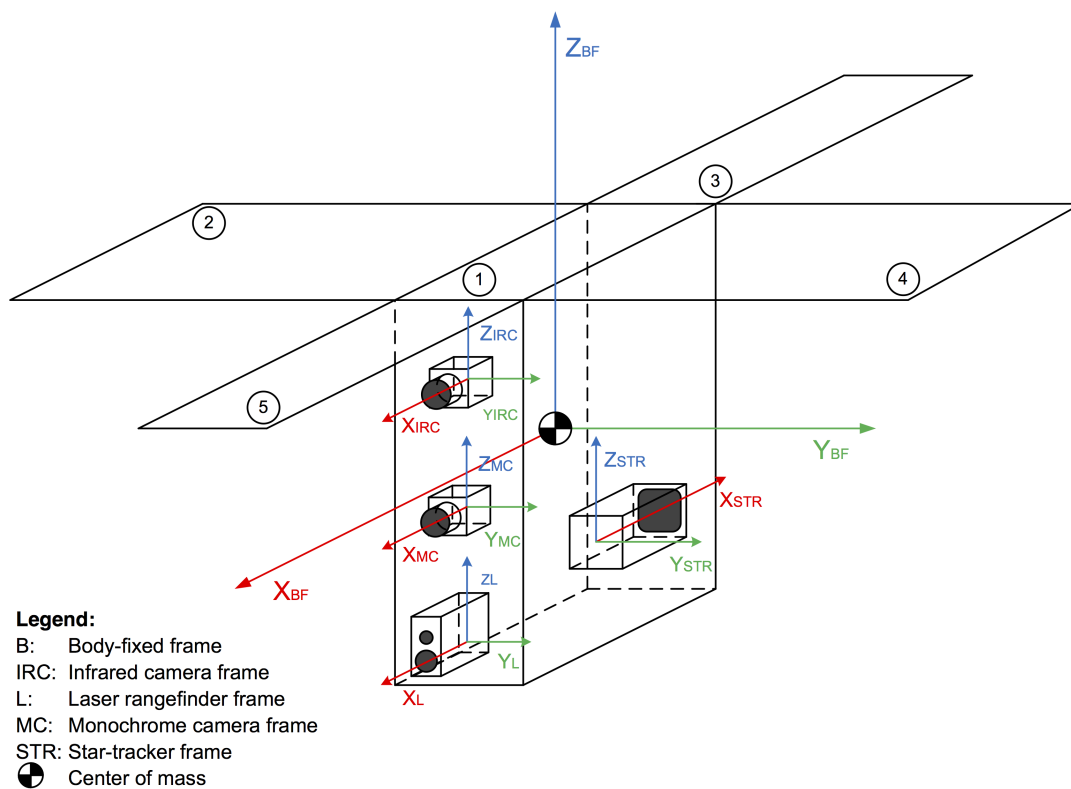
Figure A.2. Imaging array placement on the satellite body. The x-axis on the satellite's body-fixed frame is defined as being parallel to the imaging direction.

Orbit-Based Reference Frames

All orbit-based frames have their origin at the center of mass of the respective satellite.

Local Vertical Local Horizontal Reference Frame (RSW)

The local vertical, local horizontal reference frame is also known as the Gaussian reference frame or the radial, transverse, normal (RTN) frame.

Origin : At the center of mass of the respective satellite.

O_x : Along the line of position vector of the center of mass of the respective The positive direction is towards the aperture of the optics assembly.

O_y : Perpendicular to O_x, positive direction in the direction of the velocity vector of the satellite. Note that the O_y axis of the RSW aligns with the

O_z : Completes the RH reference frame.
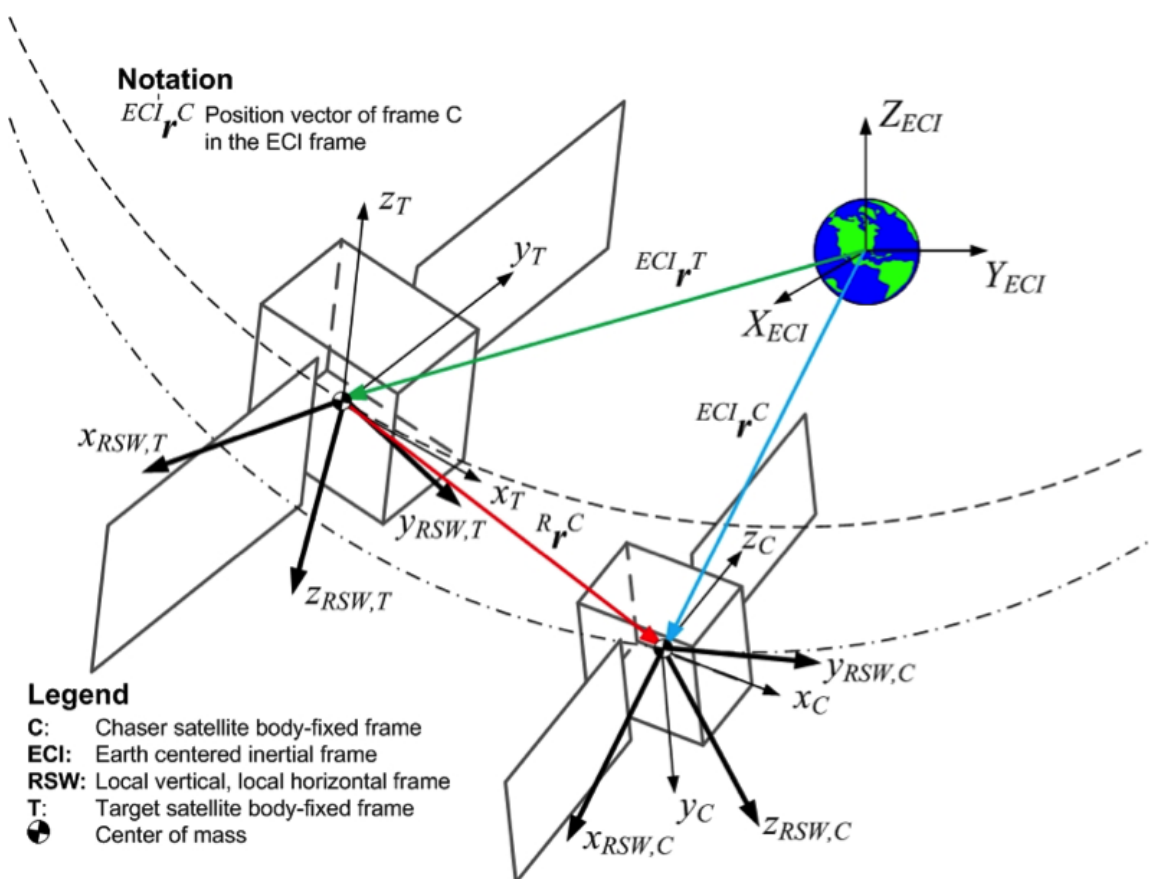
Figure A.3. Illustration of the orbit-based and ECI reference frames.

Earth-based Reference Frames

World Geodetic System 1984 (WGS84)

The components of the position and velocity vectors obtained from the GPS module are expressed with respect to the WGS-84 system (Imagery & Agency, 2000).

Origin : At the center of mass of the Earth.

O_x : Intersection of the International Earth Rotation Service (IERS), Reference Meridian (IRM), and the plane passing through the origin and normal to the Z-axis. The IRM is coincident with the Bureau International de lHeure (BIH) Zero Meridian (epoch 1984.0) with an uncertainty of 0.005".

O_y : Completes the RH Earth-Centered, Earth-Fixed system.

O_z : The direction of the IERS Reference Pole (IRP). This direction corresponds to the direction of the BIH Conventional Terrestrial Pole (CTP) (epoch 1984.0) with an uncertainty of 0.005".

B. Extended Kalman Filter Gains

This document describes the process used to calculate the G, W, H, and V matrices used in the EKF process outlined in Section 3.1.

The filter state is a ten element column vector derived from the quaternion kinematics and rate gyro model. The kinematics are given in matrix notation as

$$
\dot{\bar{q}} = \frac{1}{2}
\begin{bmatrix}
0 & -\omega_x & -\omega_y & -\omega_z \\
\omega_x & 0 & \omega_z & -\omega_y \\
\omega_y & -\omega_z & 0 & \omega_x \\
\omega_z & \omega_y & -\omega_x & 0
\end{bmatrix}
\begin{bmatrix}
q_0 \\
q_1 \\
q_2 \\
q_3
\end{bmatrix},
$$

where ω_n represents the true angular rate about the subscript body axis.

The rate gyro model assumes an individual sensor for each body axis. Thus, the scalar equation

$$
\frac{1}{1 + S_{g,n}}(\omega_{g,n} - b_{g,n} - \omega_{arw,n}) = \omega_n,
$$

is applied to each axis independently. Where $S_{g,n}$ is a scaling factor, $b_{g,n}$ is a bias term and $\omega_{arw,n}$ is the angle random walk,

Substituting the gyro model equation into the quaternion kinematics yields the non-linear state model

$$
\begin{bmatrix} \dot{q}_0 \\ \dot{q}_1 \\ \dot{q}_2 \\ \dot{q}_3 \end{bmatrix} = \frac{1}{2} \begin{bmatrix} 0 & \frac{-1}{1+S_{g,x}}(\omega_{g,x} - b_{g,x} - \omega_{arw,x}) & \frac{-1}{1+S_{g,y}}(\omega_{g,y} - b_{g,y} - \omega_{arw,y}) & \frac{-1}{1+S_{g,z}}(\omega_{g,z} - b_{g,z} - \omega_{arw,z}) \\ \frac{1}{1+S_{g,x}}(\omega_{g,x} - b_{g,x} - \omega_{arw,x}) & 0 & \frac{1}{1+S_{g,z}}(\omega_{g,z} - b_{g,z} - \omega_{arw,z}) & \frac{-1}{1+S_{g,y}}(\omega_{g,y} - b_{g,y} - \omega_{arw,y}) \\ \frac{1}{1+S_{g,y}}(\omega_{g,y} - b_{g,y} - \omega_{arw,y}) & \frac{-1}{1+S_{g,z}}(\omega_{g,z} - b_{g,z} - \omega_{arw,z}) & 0 & \frac{1}{1+S_{g,x}}(\omega_{g,x} - b_{g,x} - \omega_{arw,x}) \\ \frac{1}{1+S_{g,z}}(\omega_{g,z} - b_{g,z} - \omega_{arw,z}) & \frac{1}{1+S_{g,y}}(\omega_{g,y} - b_{g,y} - \omega_{arw,y}) & \frac{-1}{1+S_{g,x}}(\omega_{g,x} - b_{g,x} - \omega_{arw,x}) & 0 \end{bmatrix} \begin{bmatrix} q_0 \\ q_1 \\ q_2 \\ q_3 \end{bmatrix}.
$$

(B.1)

S_n and b_n are also defined as part of the state:

$$
\dot{\boldsymbol{b_g}} = \begin{bmatrix} \omega_{rrw,x} & 0 & 0 \\ 0 & \omega_{rrw,y} & 0 \\ 0 & 0 & \omega_{rrw,z} \end{bmatrix},
$$

(B.2)

$$
\dot{\boldsymbol{S_g}} = \begin{bmatrix} \omega_{srw,x} & 0 & 0 \\ 0 & \omega_{srw,y} & 0 \\ 0 & 0 & \omega_{srw,z} \end{bmatrix}.
$$

(B.3)

The complete estimated state is then

$$\boldsymbol{X}(t, \boldsymbol{u}, \boldsymbol{w}) = [q_0, q_1, q_2, q_3, b_{g,x}, b_{g,y}, b_{g,z}, S_{g,x}, S_{g,y}, S_{g,z}]^T, \qquad \text{(B.4)}$$

where $\boldsymbol{u}$ is the state input $\omega_{g,n}$. It is assumed the system has non-additive noise so the discrete linearization has the following form

$$g(\boldsymbol{u}_{(k)}, \boldsymbol{X}_{(k-1)}, \boldsymbol{w}_{(k)}) \approx$$

$$g(\boldsymbol{u}_{(k)}, \boldsymbol{\mu}_{(k-1)}, 0) + \frac{\delta g(\boldsymbol{u}_{(k)}, \boldsymbol{\mu}_{(k-1)}, 0)}{\delta \boldsymbol{X}_{(k-1)}} \Delta \boldsymbol{\mu}_{(k-1)} + \frac{\delta g(\boldsymbol{u}_{(k)}, \boldsymbol{\mu}_{(k-1)}, \boldsymbol{w}_{(k)})}{\delta \boldsymbol{w}_{(k)}} \Delta \boldsymbol{w}_{(k)}, \quad \text{(B.5)}$$

$$g(\boldsymbol{u}_{(k)}, \boldsymbol{X}_{(k-1)}, \boldsymbol{w}_{(k)}) \approx g(\boldsymbol{u}_{(k)}, \boldsymbol{\mu}_{(k-1)}) + \boldsymbol{G}_{(k-1)} \Delta \boldsymbol{\mu}_{(k-1)} + \boldsymbol{W}_{(k)} \Delta \boldsymbol{w}_{(k)}. \qquad \text{(B.6)}$$

Where $\boldsymbol{G}$ and $\boldsymbol{W}$ are Jacobian matrices ((G. Blesser, n.d.)). The linearizion process that follows in lengthy and unwieldy. Therefore, the process is shown in detail only for the first state, q_0, then the proceeding results are presented.

Consider the $\dot{q}_0$ term of the non-linear state equation

$$\dot{q}_0 = \frac{1}{2} \left[-\frac{1}{1 + S_{g,x}} (\omega_{g,x} - b_{g,x} - \omega_{arw,x}) q_1 - \frac{1}{1 + S_{g,y}} (\omega_{g,y} - b_{g,y} - \omega_{arw,y}) q_2 \right.$$

$$\left. -\frac{1}{1 + S_{g,z}} (\omega_{g,z} - b_{g,z} - \omega_{arw,z}) q_3 \right]. \quad \text{(B.7)}$$

Its first-order partial derivative with zero noise corresponding to the first row of $\boldsymbol{G}$

is

$$
\frac{\delta q_0}{\delta q_i}(\boldsymbol{u}, \Delta\boldsymbol{\mu}, 0) =
$$

$$
\frac{1}{2}\left[\frac{-1}{1+S_{gx,*}}(\omega_{g,x}-b_{gx,*})\Delta q_1 - \frac{1}{1+S_{gy,*}}(\omega_{g,y}-b_{gy,*})\Delta q_2\right.
$$

$$
-\frac{1}{1+S_{gz,*}}(\omega_{g,z}-b_{gz,*})\Delta q_3 + \Delta b_{g,x}(\frac{-1}{1+S_{gx,*}})q_{1,*} + \Delta b_{g,y}(\frac{-1}{1+S_{gy,*}})q_{2,*}
$$

$$
+ \Delta b_{g,z}(-\frac{-1}{1+S_{gz,*}})q_{3,*} + \frac{1}{(1+S_{gx,*})^2}(\omega_{g,x}-b_{gx,*})q_{1,*}\Delta S_{g,x}
$$

$$
+ \frac{1}{(1+S_{gy,*})^2}(\omega_{g,y}-b_{gy,*})q_{2,*}\Delta S_{g,y} + \left.\frac{1}{(1+S_{gz,*})^2}(\omega_{g,z}-b_{gz,*})q_{3,*}\Delta S_{g,z}\right]. \quad \text{(B.8)}
$$

And the partial derivative with respect to the noise w corresponding to the first row

of $\boldsymbol{W}$ is

$$
\frac{\delta q_{0,*}}{\delta \omega_n}(\boldsymbol{u}, \Delta\boldsymbol{\mu}, \boldsymbol{w}) = \frac{1}{2}\left[\Delta\omega_{arw,x}(\frac{1}{1+S_{gx,*}})q_{1,*}\right.
$$

$$
\left. + \Delta\omega_{arw,y}(\frac{1}{1+S_{gy,*}})q_{2,*} + \Delta\omega_{arw,z}(\frac{1}{1+S_{gz,*}})q_{3,*}\right]. \quad \text{(B.9)}
$$

Equations (B.8) and (B.9) are brought into the discrete time domain using the

forward Euler method

$$
y_{(k+1)} = y_{(k)} + T_s g(t_{(k)}, y_{(k)}), \quad \text{(B.10)}
$$

where T_s is the desired time step length. Which yields

$$\Delta q_{0,(k)} = \Delta q_{0,(k-1)} + \frac{T_s}{2}\Bigg[(-\frac{1}{1+S_{gx,(k-1)}}(\omega_{gx,(k)}-b_{gx,(k-1)}))\Delta q_{1,(k-1)} - \frac{1}{1+S_{gy,(k-1)}}(\omega_{gy,(k)}-b_{gy,(k-1)})\Delta q_{2,(k-1)}$$

$$- \frac{1}{1+S_{gz,(k-1)}}(\omega_{gz,(k)}-b_{gz,(k-1)})\Delta q_{3,(k-1)} - \Delta b_{gx,(k-1)}(\frac{-1}{1+S_{gx,(k-1)}}q_{1,(k-1)}) - \Delta b_{gy,(k-1)}(\frac{-1}{1+S_{gy,(k-1)}}q_{2,(k-1)})$$

$$- \Delta b_{gz,(k-1)}(\frac{-1}{1+S_{gz,(k-1)}}q_{3,(k-1)}) - \frac{1}{(1+S_{gx,(k-1)})^2}(\omega_{gx,(k)}-b_{gx,(k-1)})q_{1,(k-1)}\Delta S_{gx,(k-1)}$$

$$- \frac{1}{(1+S_{gy,(k-1)})^2}(\omega_{gy,(k)}-b_{gy,(k-1)})q_{2,(k-1)}\Delta S_{gy,(k-1)} - \frac{1}{(1+S_{gz,(k-1)})^2}(\omega_{gz,(k)}-b_{gz,(k-1)})q_{3,(k-1)}\Delta S_{gz,(k-1)}\Bigg], \quad \text{(B.11)}$$

$$\Delta q_{0,(k)} = \Delta q_{0,(k-1)} + \frac{T_s}{2}\Bigg[\Delta\omega_{arw,x,(k)}(\frac{1}{1+S_{gx,(k-1)}})q_{1,(k-1)} + \Delta\omega_{arw,y,(k)}(\frac{1}{1+S_{gy,(k-1)}})q_{2,(k-1)}$$

$$+ \Delta\omega_{arw,z,(k)}(\frac{1}{1+S_{gz,(k-1)}})q_{3,(k-1)}\Bigg], \quad \text{(B.12)}$$

respectively. Note that the equilibrium terms $(*)$ simply become the conditions for the previous time step.

Applying this method to the remaining nine states produces the complete $\boldsymbol{G}$ and $\boldsymbol{W}$ state estimation matrices

$$
\boldsymbol{G}_{(k-1)} = T_s \begin{bmatrix}
\frac{1}{T_s} & -\text{dqx} & -\text{dqy} & -\text{dqz} & -\text{dbx } q_1 & -\text{dby } q_2 & -\text{dbz } q_3 & -\text{dSx } q_1 & -\text{dSy } q_2 & -\text{dSz } q_3 \\
\text{dqx} & \frac{1}{T_s} & \text{dqy} & -\text{dqz} & \text{dbx } q_1 & -\text{dby } q_2 & \text{dbz } q_3 & \text{dSx } q_1 & -\text{dSy } q_2 & \text{dSz } q_3 \\
\text{dqx} & -\text{dqy} & \frac{1}{T_s} & \text{dqz} & \text{dbx } q_1 & \text{dby } q_2 & -\text{dbz } q_3 & \text{dSx } q_1 & \text{dSy } q_2 & -\text{dSz } q_3 \\
\text{dqx} & \text{dqy} & -\text{dqz} & \frac{1}{T_s} & -\text{dbx } q_1 & \text{dby } q_2 & \text{dbz } q_3 & -\text{dSx } q_1 & \text{dSy } q_2 & \text{dSz } q_3 \\
0 & 0 & 0 & 0 & \frac{1}{T_s} & 0 & 0 & 0 & 0 & 0 \\
0 & 0 & 0 & 0 & 0 & \frac{1}{T_s} & 0 & 0 & 0 & 0 \\
0 & 0 & 0 & 0 & 0 & 0 & \frac{1}{T_s} & 0 & 0 & 0 \\
0 & 0 & 0 & 0 & 0 & 0 & 0 & \frac{1}{T_s} & 0 & 0 \\
0 & 0 & 0 & 0 & 0 & 0 & 0 & 0 & \frac{1}{T_s} & 0 \\
0 & 0 & 0 & 0 & 0 & 0 & 0 & 0 & 0 & \frac{1}{T_s}
\end{bmatrix}_{(k-1)} , \qquad \text{(B.13)}
$$

$$W_{(k-1)} = \begin{bmatrix} 0 & -\mathrm{d}\omega\mathrm{x}\ q_1 & -\mathrm{d}\omega\mathrm{y}\ q_2 & -\mathrm{d}\omega\mathrm{z}\ q_3 & 0 & 0 & 0 & 0 & 0 & 0 \\ 0 & \mathrm{d}\omega\mathrm{x}\ q_1 & -\mathrm{d}\omega\mathrm{y}\ q_2 & \mathrm{d}\omega\mathrm{z}\ q_3 & 0 & 0 & 0 & 0 & 0 & 0 \\ 0 & \mathrm{d}\omega\mathrm{x}\ q_1 & \mathrm{d}\omega\mathrm{y}\ q_2 & -\mathrm{d}\omega\mathrm{z}\ q_3 & 0 & 0 & 0 & 0 & 0 & 0 \\ 0 & -\mathrm{d}\omega\mathrm{x}\ q_1 & \mathrm{d}\omega\mathrm{y}\ q_2 & \mathrm{d}\omega\mathrm{z}\ q_3 & 0 & 0 & 0 & 0 & 0 & 0 \\ 0 & 0 & 0 & 0 & 1 & 0 & 0 & 0 & 0 & 0 \\ 0 & 0 & 0 & 0 & 0 & 1 & 0 & 0 & 0 & 0 \\ 0 & 0 & 0 & 0 & 0 & 0 & 1 & 0 & 0 & 0 \\ 0 & 0 & 0 & 0 & 0 & 0 & 0 & 1 & 0 & 0 \\ 0 & 0 & 0 & 0 & 0 & 0 & 0 & 0 & 1 & 0 \\ 0 & 0 & 0 & 0 & 0 & 0 & 0 & 0 & 0 & 1 \end{bmatrix}_{(k-1)} . \tag{B.14}$$

Where

$$\mathrm{dqn} = \frac{1}{1 + S_{gn,(k-1)}}(\omega_{gn,(k)} - b_{gn,(k-1)}), \tag{B.15}$$

$$\mathrm{d}\omega\mathrm{n} = \frac{-1}{1 + S_{gn,(k-1)}}, \tag{B.16}$$

$$\mathrm{dbn} = \frac{-1}{1 + S_{gn,(k-1)}}, \tag{B.17}$$

$$\text{dSn} = \frac{-1}{(1 + S_{gn,(k-1)})^2}\left(\omega_{gn,(k)} - b_{gn,(k-1)}\right). \tag{B.18}$$

For simplicity, the measurement and correction matrices are assumed to be identity

$$\boldsymbol{H} = \boldsymbol{I}_{10 \times 10}, \tag{B.19}$$

$$\boldsymbol{V} = \boldsymbol{I}_{10 \times 10}. \tag{B.20}$$

C. Simulation Block Diagrams

This document contains Simulink block diagram models of the control configurations discussed in Chapter 5. They are intended to showcase the high-level system configuration and provide more detail on the implementation of the different controllers on the continuous and discrete domains.
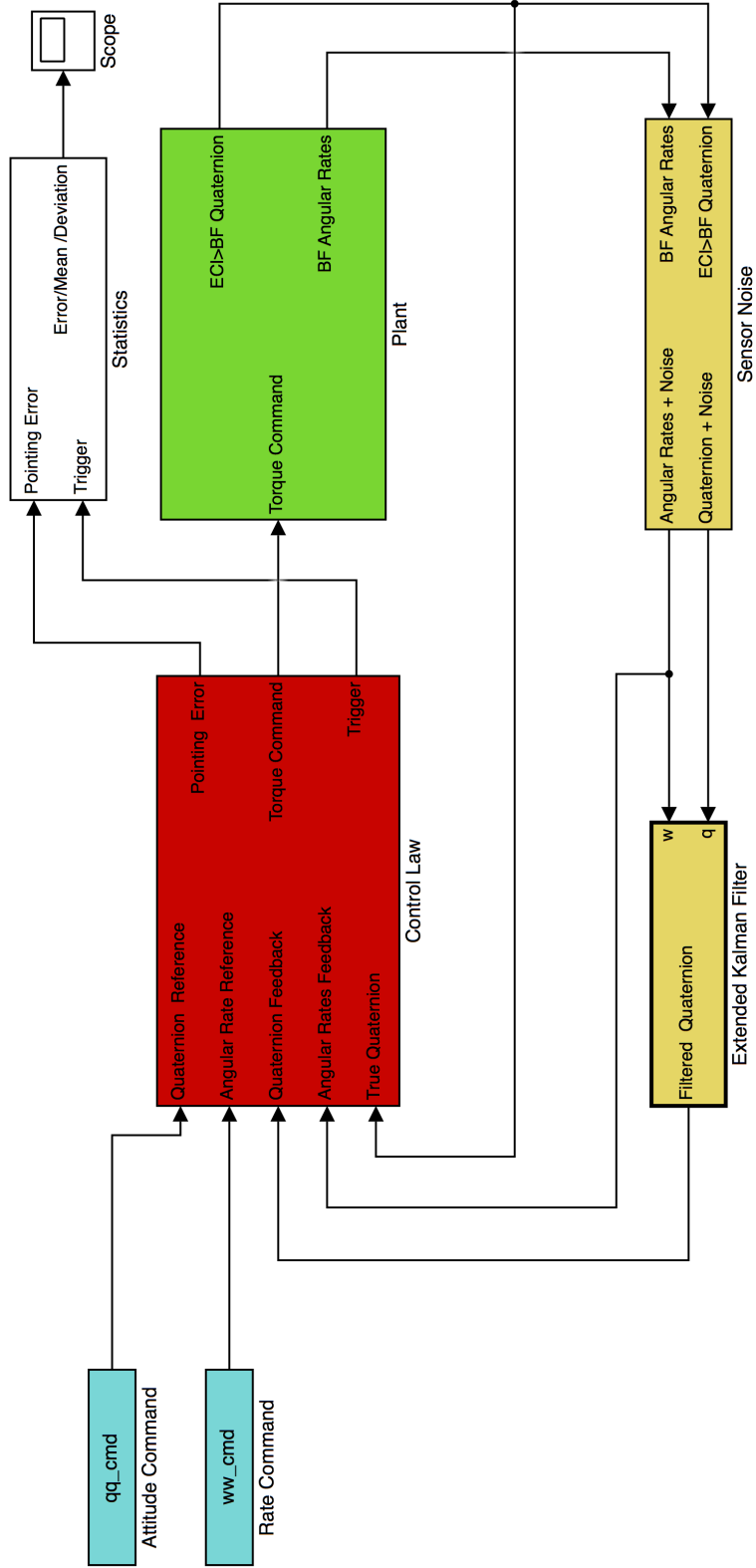
Figure C.1. Simulink block diagram model of continuous domain ADCS simulation with EKF feedback. Both the controller and estimator subsystems run at the same frequency as the plant.
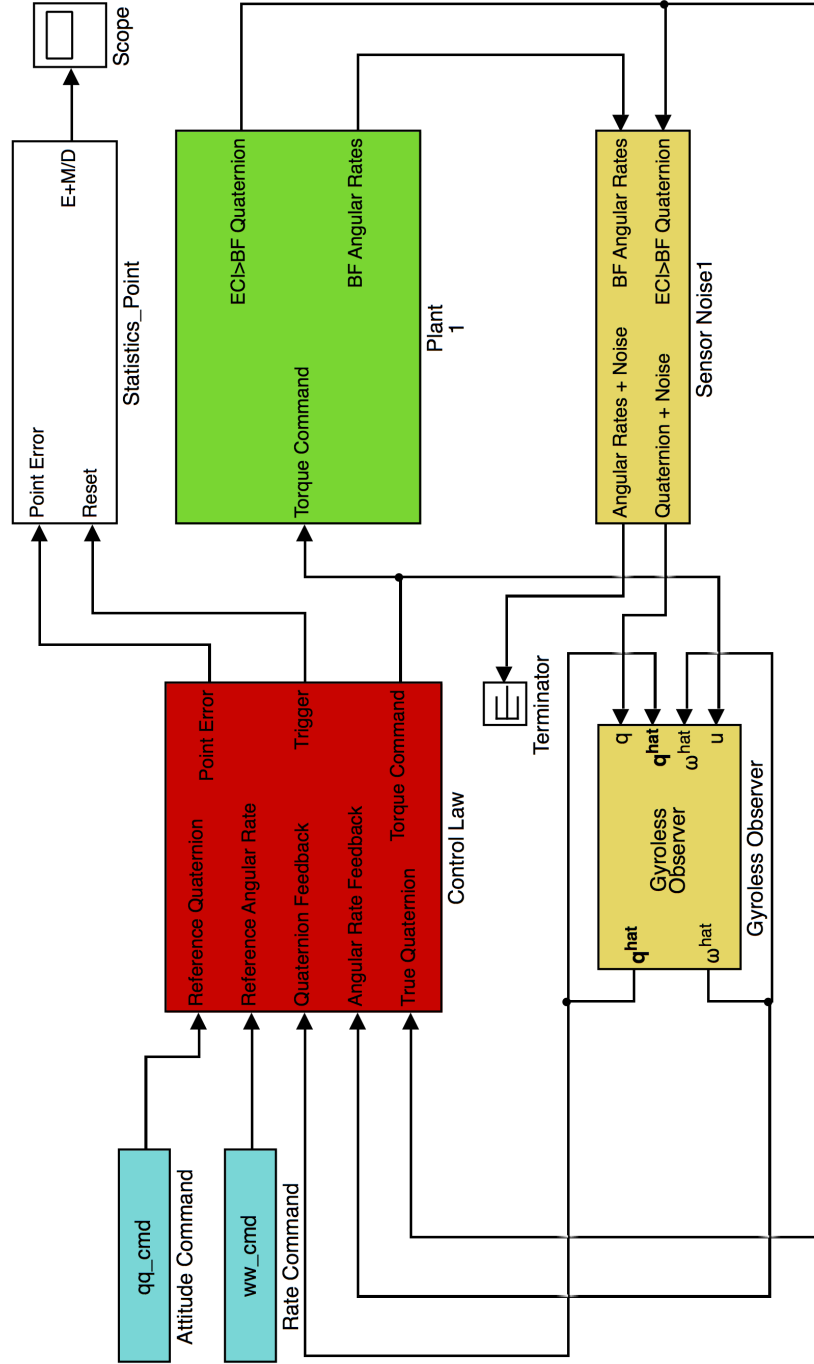
Figure C.2. Simulink block diagram model of continuous domain ADCS simulation with angular rate observer feedback. Both the controller and estimator subsystems run at the same frequency as the plant.
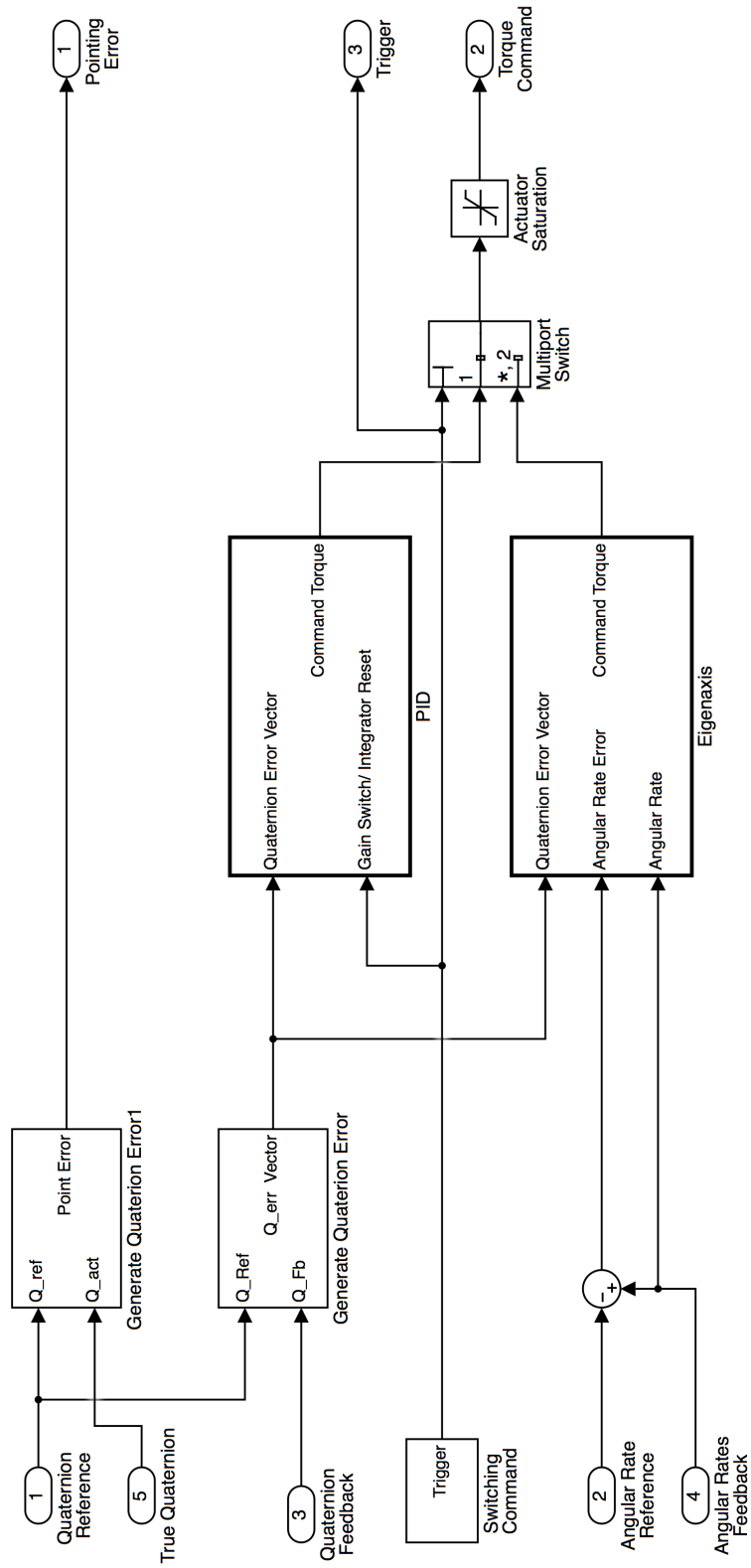
Figure C.3. Simulink block diagram model of continuous domain switching controller. The 'eigenaxis' block contains the fixed gain eigenaxis control law; the 'PID' block contains the PID control law and gain scheduling algorithm.
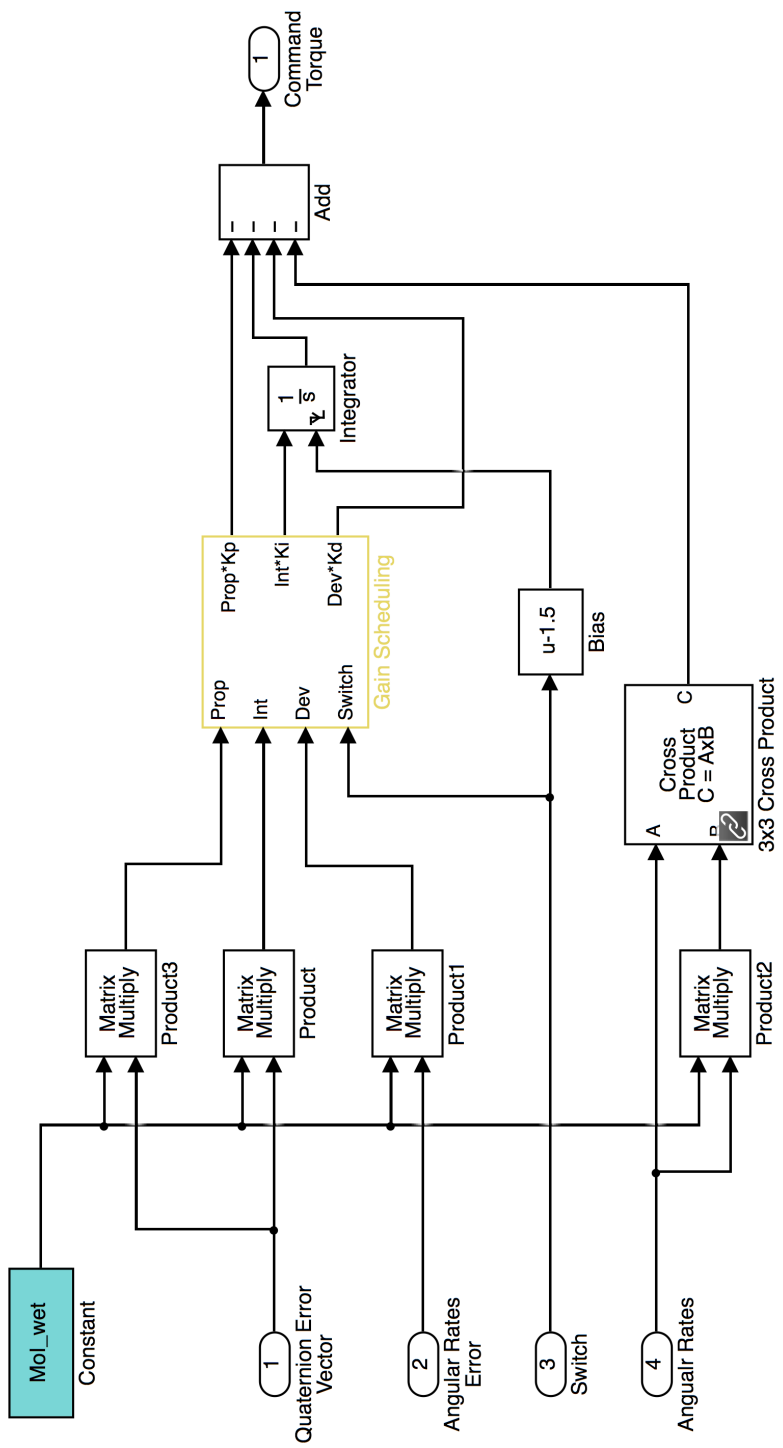
Figure C.4. Simulink block diagram model of continuous domain eigenaxis controller with gain scheduling and integral q_{e_v} control.
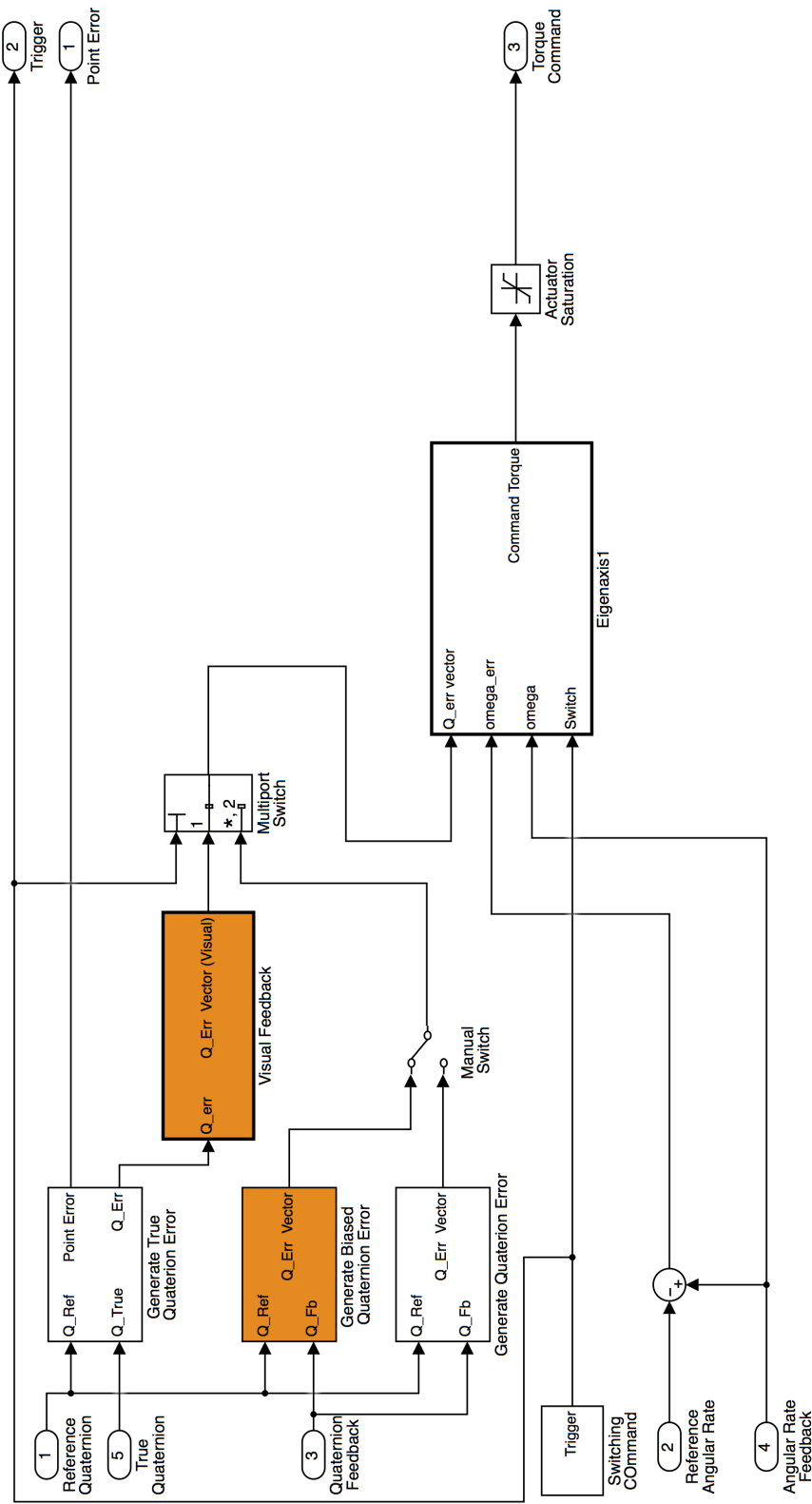
Figure C.5. Simulink block diagram model of continuous domain modified eigenaxis controller with gain scheduling and payload image feedback.
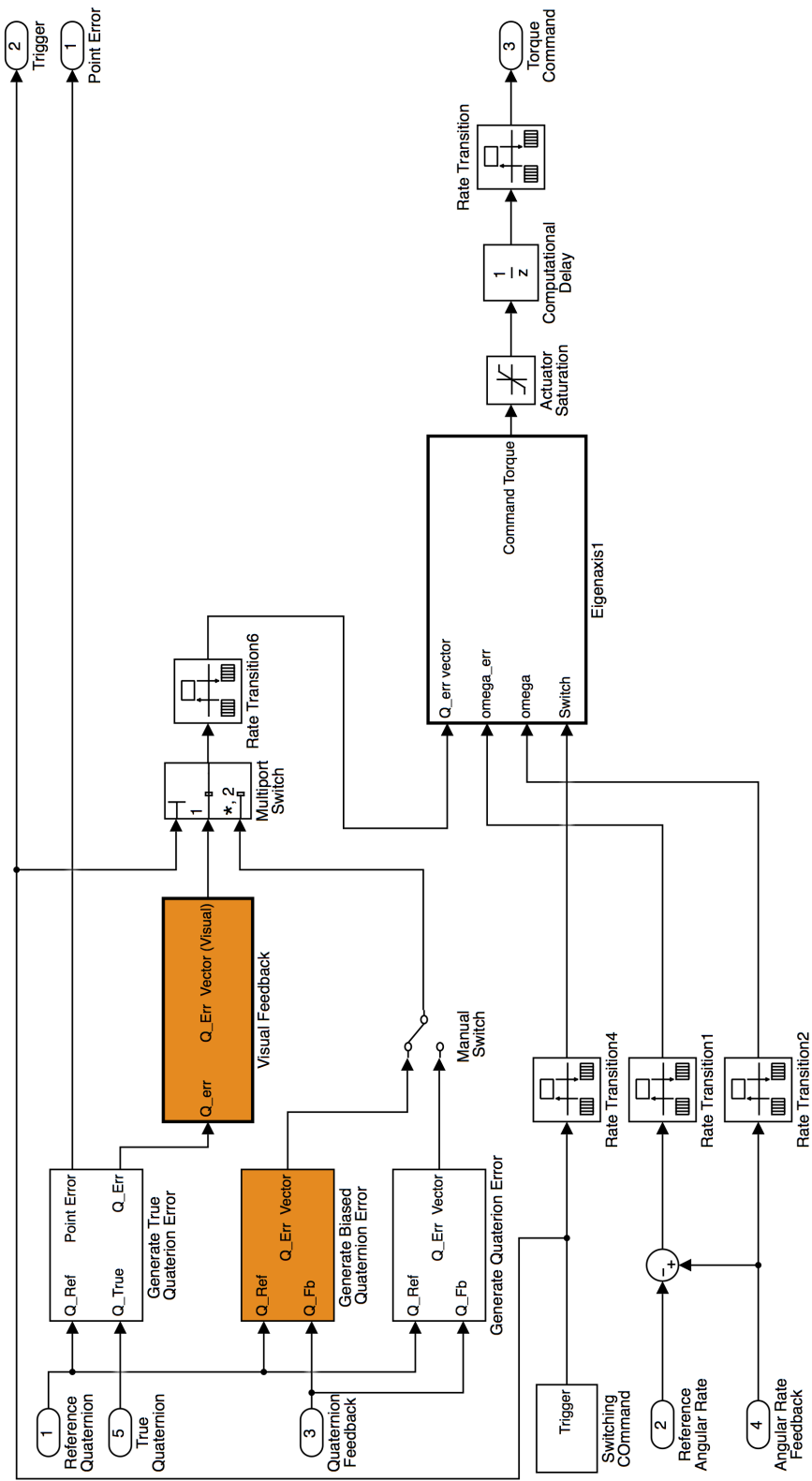
Figure C.6. Simulink block diagram mdoel of discrete time modified eigenaxis controller with gain scheduling and payload image feedback. The rate transition blocks on the controller inputs down-sample the estimator outputs. The rate transition blocks on the output of the controller, introduce computational delays.